Glacier Surface Velocity Estimation & Facies Classification using InSAR and Multi-Temporal SAR Techniques in Indian Himalaya
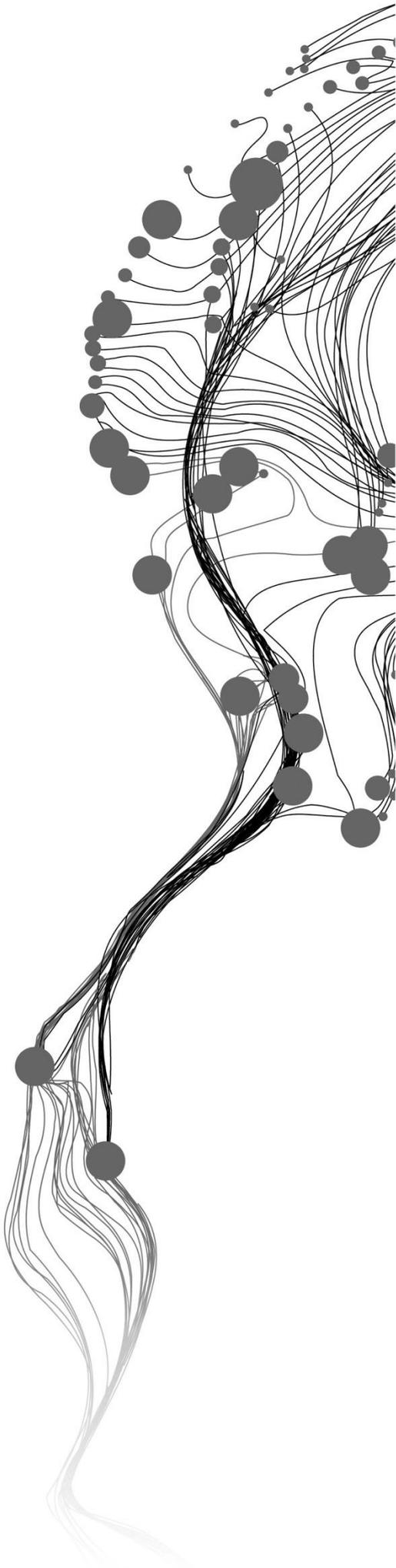
ANIRUDHA VIJAY MAHAGAONKAR
March, 2019

SUPERVISORS:
Dr. Praveen K Thakur
Dr. Ling Chang

Glacier Surface Velocity Estimation & Facies Classification using InSAR and Multi-Temporal SAR Techniques in Indian Himalaya

ANIRUDHA VIJAY MAHAGAONKAR
Enschede, The Netherlands; March, 2019

ABSTRACT

ESA's Sentinel-1 is one of the most conventional SAR missions currently in operation. Encouraged by the availability of 6-day interferometric pairs from Sentinel-1 program we have taken up assessment of glacier velocities and classification of glacier facies for Siachen, Bara Shigri and Gangotri Glaciers representing the Indian Himalayan Region (IHR). This rugged mountain region hosts a huge chunk of glaciers, and is lately severely affected by climate change, substantiating the need for regular studies in the region. Velocity assessments were performed using Differential SAR Interferometry (DInSAR) approach for 2016, while classification of glacier facies was done for 2015, 2016, 2017 and 2018 using the Multi-temporal SAR technique. Further, ELA for each of these years were delineated and assessed to understand the trend of change.

Siachen glacier was the fastest moving glacier with velocity ranging between 0-135.27±5.1m/y, while Bara Shigri and Gangotri glaciers had velocities ranging between 0-32.5±2.15m/y and 0-41.85±7.32m/y respectively. Our surface velocity estimates were strongly consistent with pervious findings. It is noted that velocities have changed substantially over the past 20 years whereas they are more or less similar between 2014 and 2016, suggesting that standing glacier mass may exert stress driving the glacier movement. As interferometric pairs only from one pass were available, our results are most sensitive and reliable along the glacier trunks which nearly coincides with the LOS direction of the sensor in consideration. Sensitivity metrics for assessing the sensitivity in a particular flow direction, using Sentinel-1 sensor are presented. The average sensitivity over main trunk of Siachen glacier was 0.66, while for Bara Shigri and Gangotri glaciers it was 0.61 and 0.55 respectively. These values along with acquisition and processing errors are used for reporting associated uncertainties.

Radar facies classification and ELA delineation was done using satellite images from three seasons – Winter, Early Summer and Late Summer. Upper Percolation Zone was seen only over Siachen Glacier, while it was absent over Bara Shigri and Gangotri Glaciers. Other zones that were identified include Middle Percolation Zone, Lower Percolation Zone, Bare Ice Facies and Debris Covered Ice Facies. Dry Snow Facies and Super-Imposed Ice Facies do not exist in the IHR. The results of classification were highly accurate, with an overall accuracy >85%. ELAs were the lowest in 2015 for all the 3 glaciers, and gradually moved higher in altitude over 2016, 2017 and 2018. It was found that Gangotri glacier was relatively more sensitive due to its exposure to warm temperatures throughout the year. By analysing ELA changes using temperature and precipitation information, extracted from ERA Interim products, it was found that temperature has higher influence on ELA fluctuations than precipitation.

In this study we have also assessed the utility of Sentinel-1 products for studying glacial dynamics in the IHR. While it is observed that Sentinel-1 products are highly applicable, their careful pre-assessment may be required for best results before usage.

Keywords: Sentinel-1, Indian Himalayan Region, DInSAR, Glacier velocity, Facies classification, ELA, Sensitivity.

ACKNOWLEDGEMENTS

TABLE OF CONTENTS

LIST OF FIGURES

LIST OF TABLES

ABBREVATIONS

1/2/3/4 - D	One/Two/Three/Four Dimensional
ALOS	Advanced Land Observation Satellite
BIF	Bare Ice Facies
CSA	Canadian Space Agency
DCIF	Debris Covered Ice Facies
DEM	Digital Elevation Model
DGPS	Differential Global Positioning System
DInSAR	Differential SAR Interferometry
DLR	German Aerospace Center
EC	European Commission
ECMWF	European Center for Medium-range Weather Forecasting
ELA	Equilibrium Line Altitude
Envisat	Environmental Satellite
ERA	ECMWF ReAnalysis
ERS	European Remote-Sensing Satellite
ESA	European Space Agency
ESD	Enhanced Spectral Diversity
EU	European Union
EW	Extra Wide Swath Mode
GIS	Geographic Information System
GLOF	Glacial Lake Outburst Flood
GPS	Global Positioning System
GRD	Ground Range Detected
HPC	High Processing Cluster
IHR	Indian Himalayan Region
InSAR	Interferometry
ISRO	Indian Space Research Organization
IW	Interferometric Wide Swath Mode
JAXA	Japan Aerospace Exploration Agency
LOS	Line of Sight
LPF	Lower Percolation Facies
MAI	Multiple Aperture Interferometry
MPF	Middle Percolation Facies
NASA	National Aeronautical Space Administration
NISAR	NASA - ISRO SAR Mission
OA	Overall Accuracy
PA	Producer Accuracy
PALSAR	Phased Array type L-Band Synthetic Aperture Radar
PolSAR	Polarimetric SAR
PSI	Persistent Scatterer Interferometry
Radar	Radio Detection and Ranging
Radarsat	Canadian Radar Earth Observation Satellite
RISAT	ISRO's Radar Imaging Satellite
S1	Sentinel-1
S1a	Sentinel-1a
S1b	Sentinel-1b
SAR	Synthetic Aperture Radar
SLA	Snow Line Altitude
SLC	Single Look Complex
SM	Strip Map Mode
SNAPHU	Statistical-cost, Network-flow Algorithm for Phase Unwrapping
SNR	Signal-to-Noise Ratio

SRTM	Shuttle Radar Topography Mission
SVM	Support Vector Machine
UA	User Accuracy
UPF	Upper Percolation Facies
USA	United States of America
VHR	Very High Resolution
WGS84	World Geodetic System 1984
WV	Wave Mode

Units

mm	millimetre
cm	centimetre
m	metre
dB	decibel
y	year
°C	Degree Celsius
°	Angular Degree
d	day

1. INTRODUCTION

1.1. Motivation

The melting of glaciers and ice caps around the world is unprecedented (Immerzeel, van Beek, & Bierkens, 2010; Michael Zemp et al., 2015), and this has been asserted with substantial evidences and high confidence. Changing climate patterns, rising sea levels, depleting freshwater resources and impending risks from glacial hazards put the major chunk of life-forms on Earth in danger. These factors of vulnerability establish the critical need to assess the evolution of these cryospheric systems (Bolch et al., 2012). Understanding them can help in mitigating impending risk levels. Additionally, glaciers are sensitive systems (Kääb, Chiarle, Raup, & Schneider, 2007; Kulkarni, Rathore, Singh, & Bahuguna, 2011) and can act as indicators to change in climate. Thus, realizing their responses can help in many ways than just one.

Satellite Synthetic Aperture Radar (SAR) has revolutionized cryospheric research. Modern developments in this technology have made it robust for mapping and monitoring snow and ice systems across the world. Among the many applications of SAR, topographic modelling and surface deformation assessment have been well established. Pool of studies performed using these approaches have elevated the general understanding about glacial behaviour and response substantially. Easy availability of SAR products from different missions, such as ERS-1/2, ALOS-1/2, RADARSAT-1/2, ENVISAT and RISAT, lasting several years was instrumental in this development.

European Space Agency's (ESA) Sentinel-1a &-1b SAR missions were recently launched in 2014 and 2016 respectively. Promising a 6-day revisit interval and millimetre-level observations for ground targets, these satellites have opened huge scope of opportunities for precise glacier assessment and timely monitoring of glacial-disasters. These modern SAR products may provide a base for studying Himalayan Glaciers, which couldn't be completely accomplished using other existing products, with an exception of ERS-1/2 (tandem operation mode) and TerraSAR-X and TanDEM-X. However, there are several challenges that will have to be addressed. In this study, the potential of Sentinel-1a & -1b SAR products for glacier classification and velocity estimation over Himalayan systems will be assessed.

1.2. Background

From sea ice to ice sheets and the snow caps, Cryosphere comprises of all forms of snow and ice spread across the planet. These elements together play a significant role in functioning of the Earth. Glaciers, a major component of the cryosphere, are masses of snow and ice that move due to its weight that has accumulated over several years, and also under the influence of gravity. The accumulation of snow is balanced by melting of ice during summer months, and this altogether defines the glacier cycle (system). The glacier system has far reaching impacts on sustenance of natural ecological systems, forming a crucial part of our environment (Benn & Evans, 2010).

Glaciers and ice sheets have been undergoing unprecedented change in the recent past (Bolch et al., 2012; Immerzeel et al., 2010). Due to their sensitive nature, these ice forms are losing mass at rates higher than accumulation, causing them to be in negative balance. They have been following a regular pattern of

accumulation and retreat for several millennia, which has been disturbed by recent human-induced climate change (Rosenzweig et al., 2008). As a result, this has led to changes in glacier extent (Benn & Evans, 2010; Paul & Haeberli, 2008; M. Zemp, Hoelzle, & Haeberli, 2009), rise in global sea level (Gardner et al., 2013; Meier et al., 2007), alteration to the hydrological balance (Bliss, Hock, & Radić, 2014; Kaser, Grosshauser, & Marzeion, 2010) and enhanced risk from glacial lake outburst floods (GLOFs) (Bajracharya & Mool, 2009; Kääb et al., 2003; Mahagaonkar, Wangchuk, Ramanathan, Tshering, & Mahanta, 2017). These researches have used elementary glacial dynamics to understand balance-imbalance of glacial systems, whose regular monitoring can help in minimizing any kind of major risk posed by glacial hazards.

Remote sensing technology plays a critical role in enabling timely monitoring of dynamics on temperate glaciers, which otherwise are inaccessible due to rough terrain and inhospitable atmospheric conditions. Since the launch of LANDSAT by NASA in 1970s, optical satellite products are available from various missions at different scales and resolutions. From delineation and mapping of glacial extents, to classification of glaciated regions and estimating surface velocity, optical datasets have been used in plethora of glacial applications, making it easier to study these dynamic structures on wider spatial extents. Monitoring changes in equilibrium line altitudes (ELA), snout fluctuations and development of supra-glacial and pro-glacial lakes has become convenient with availability of multi-temporal products. However, a major limitation to the use of optical imageries is the cloud cover, generally present over mountain regions. This obstructs the utility of such datasets making them invalid. Moreover, due to similar reflectance properties of snow, ice and firn, there generally exists and ambiguity in their differentiation (Gupta, Haritashya, & Singh, 2005). Considerable part in optical datasets is blackened by mountain shadows, causing difficulty in differentiating glaciated and non-glaciated regions.

On the other hand, the role of radar remote sensing in glacial applications has been remarkable since its advent in ~1970s. Synthetic Aperture Radar (SAR), an active microwave sensor, generally uses radiations in X (2.5-4cms), C (4-8cms), S (8-15cms) & L (15-30cms) bands (Moreira et al., 2013) of the microwave spectrum. The ability of these radiations to penetrate through clouds and function irrespective of daylight conditions has made SAR a vital technology to study glaciers. Moreover, in this part of the electromagnetic spectrum, snow, ice and liquid water have variable spectral responses that helps in better distinction from space. The side looking geometry of sensors, and penetration of microwave radiation allows collection of crucial geophysical information of ground objects. This information may be communicated in the type of scattering (surface, volume scattering) or the form of polarization, which is the vectoral orientation of the radiation with respect to direction of propagation (Paul, 1998). Usage of polarized information (HH, HV, VV and VH), referred to as Polarimetry (PolSAR), for identification of surface objects based on characteristic scattering mechanisms (Akbari, Doulgeris, & Eltoft, 2014; Partington, 1998) has been widely employed for classification of glacier surfaces using SAR (Akbari et al., 2014; Callegari, Marin, & Notarnicola, 2017; L. Huang et al., 2011; Thakur et al., 2017). Scattering of incident radiation depends on surface roughness, dielectric constant and angle of incidence of the object.

Along with polarized information, SAR sensors also record phase information, which is a measure of the distance of the object from the sensor. Phase information from two passes can be employed in Interferometric SAR (InSAR) for topographic modelling e.g. Bürgmann, Rosen, & Fielding, 2000; Massonnet & Feigl, 1998. The precision of the generated topographic model (Digital Elevation Model, DEM) is highly dependent on the degree of coherence between repeat acquisitions (Joughin, Winebrenner, & Fahnestock, 1995). Ground movements or deformation can be quantified using phase information from (two or three) repeat acquisitions having an allowable spatiotemporal baseline and insignificant atmospheric phase delay. This approach, similar to InSAR, is referred to as Differential SAR Interferometry (DInSAR) (Gabriel, Goldstein, & Zebker, 1989). DInSAR has been widely used for measuring deformation from space

(Bürgmann et al., 2000; Kumar, Venkataraman, & Høgda, 2011; Mattar et al., 1998). Glacier movement and velocity, which is inherent to understanding glacier health, can be estimated from mm to cm level precision using DInSAR (Kumar, Venkataraman, & Høgda, 2011). Alternatively, glacier surface movements can also be quantified using feature tracking approaches, like in optical datasets, using SAR intensity or coherence bands. This approach essentially estimates the offset between the same features or pixels with high coherence to give two dimensional velocity vectors. However, the sensitivity & precision of DInSAR is significantly higher than offset tracking, making it a more valuable option for quantifying glacier movements.

1.3. Problem Statement

Unlike remotely sensed optical products, data from SAR products is difficult to interpret. While visual interpretation of raw SAR data may be relatively complicated, several steps of processing are required to retrieve information that can help in better interpretation. Although usage of SAR products requires enhanced technical understanding of the instrument, which is complicated, it has been put to extensive use in studying various glacial components over time.

However, there are certain limitations to utility of SAR, especially in mountain terrains. Due to the side looking imaging geometry, SAR products are characterized by layover, foreshortening and shadow (Paul, 1998), a manifestation that causes substantial geometric distortion in SAR processing. The precision of SAR interferometric processing is controlled by magnitude of coherence, which is a measure of similarity between the two products used for interferometric processing (referred to as an interferometric pair). Signal to noise ratio (SNR), a measure of the receiver noise, is one component of decorrelation. Others being the spatial decorrelation caused due to the perpendicular baseline between sensor positions during acquisition of the interferometric pair. While larger baselines are desirable for topographic modelling, having them beyond the critical baseline may cause complete decorrelation in the pair, leading to significant random noise. Temporal changes, such as growth of crops and precipitation events, can bring change in the surface microstructure leading to temporal decorrelation. Additionally, phase is sensitive to deformation/displacement equivalent to half of the wavelength ($\lambda/2$), limited by the phase cycle (-π, +π]. Therefore, when displacement is significant, phase unwrapping is required and that can potentially introduce error. Moreover, recording of quad-pol data (HH, HV, VV, VH), which is important for PolSAR, is a challenge limited by the trade-off between energy utilization and polarization modes of the radar sensors. Due to this, not all modern SAR sensors provide quad-polarized information.

Glaciated regions are generally characterized by snow and water precipitation. Snowfall contributes to accumulation of mass, which is balanced by ablation over the summer period causing considerable amount of fresh snow and ice to melt. Strong winds, which are also a common phenomenon, can deposit mass of snow and dust over the glacier surfaces. All these processes, that commonly occur over glaciated regions, can significantly alter the surface, thereby, potentially contributing to temporal decorrelation. Rapid glacier displacement may also add to decorrelation on glacier surfaces (Kumar, Venkataraman, & Høgda, 2011; Sood, 2014). Therefore, a small temporal baseline (~1-2 days) will possibly be optimal for ideal interferometric pairs. Unfortunately, only ERS-1/2 mission of ESA that was operational in tandem mode for 1995-1996, could provide 1-day separated pairs for interferometric analyses. Other satellite missions have significantly longer temporal baselines ranging from 11 days (TerraSAR-X and TanDEM-X) to 14 days (ALOS-1/2), 24 days (RADARSAT-2) and 35 days (ENVISAT). At such high baselines, decorrelation will be very high, limiting their applications to glacial studies. On the other hand, the utility of PolSAR approach

for glacier facies classification (Callegari et al., 2016; L. Huang et al., 2011) is limited by non-availability of fully polarized information from modern radar satellites.

Sentinel-1a and -1b satellites have same configuration, operating with C-Band (λ = 5.6cms) having a revisit of 12 days each, and providing single polarized or dual polarized data. However, their orbits are aligned in such a way that, combined use of -1a and -1b products could provide datasets at 3-6 day temporal frequencies. The primary focus of our research is to explore and assess the applicability of Senitnel-1 products for glacial studies, specifically glacier facies classification and surface velocity estimation, in the Indian Himalayan Region (IHR). While 6-day temporal separation may possibly provide optimal correlation for DInSAR based velocity retrieval, the single and dual polarized data can be used for facies classification using Multi-temporal SAR approach (Partington, 1998; Sood, 2014; Thakur et al., 2017). This information can further be used to analyse the health of the glacier; however, this is beyond the scope of this research. The study area is focused around the Indian Himalayan Region, specifically Western Himalayas.

1.4.   Research Identification

The unprecedented changes in glacial systems and the ongoing climate change necessitates the need for updated information on elementary glacial dynamics. Our study will focus on estimation of glacier velocity and classification of glacier facies for representative glaciers in the Western Himalayan Region of India using Sentinel-1 products.

1.4.1.   Research Objectives

1.   Estimation of glacier surface velocity by Differential SAR Interferometry
2.   Classification of glacier facies using multi-temporal SAR images and ELA delineation

1.4.2.   Sub-Objectives

3.   Evaluating the quality of estimated surface velocity
4.   Evolution of line of equilibrium (ELA) using classified time-series data

1.4.3.   Research Questions

Specific to Objective 1
1.   What is the estimated surface velocity of the chosen glaciers?

Specific to Objective 2
2.   What are the different glacier facies identified using Multi-temporal SAR Approach in IHR?
3.   How accurate are the results of classification?

Specific to Objective 3
4.   What is the quality of the velocity estimated using Sentinel-1?

Specific to Objective 4
5.   How has ELA evolved/changed over the study period and what impacts the change?

1.5.   Innovation

As Sentinel-1a & -1b satellites were recently launched their products haven't been explored completely for glacial applications. The 6-day temporal baseline offered by Sentinel-1 constellation is the lowest baseline being offered by any mission currently in operation. It will be interesting to assess the applicability of Sentinel-1 products for interferometric processing in the Indian Himalayan Region, which hasn't been used so far for retrieving glacier velocities.

Also, the quality of estimated velocity will be assessed in this study, with respect to the orientation of the glacier flow direction. Such assessment hasn't been done so far, and may be required to understand as to what extent the estimates using SAR products are reliable.

1.6.   Research Methodology

Estimation of surface velocity will be performed, primarily, using Differential Interferometric SAR approach (Goldstein, Engelhardt, Kamb, & Frolich, 1993). This will require careful investigation of available datasets for the Himalayan region and assessment of coherence between different set of pairs. Imageries captured by C-Band SAR sensor on board ESA's Sentinel -1a and -1b instruments will be used in combination for this research. Alpine Himalayan glaciers are dynamic and generally fast moving with considerable amount of debris covering their surfaces. Glaciers from the Western Himalayan region are chosen for this study. In case of poor coherence for DInSAR processing, intensity offset tracking (Gray, Short, Mattar, & Jezek, 2001; Lucchitta, Rosanova, & Mullins, 1995) approach will be experimented. Validation of velocity estimates is expected to be done using field data, but in case of difficulty to access the field due to adverse weather conditions, proxy information from published sources will be used.

As Sentinel-1 data is not fully polarimetric, PolSAR classification of glacier facies using decomposed polarization information is not possible. Hence, multi-temporal SAR approach (Partington, 1998) will be used for classifying glacier surface into radar identifiable facies. This approach will require 3 images from Early Summer (April-May), Late Summer (August-September) and Early Winter (December-January). The three images will be stacked together to prepare a composite to be passed through Red, Blue and Green channels to create a RGB colour composite. Using the backscatter information, training samples will be identified on the composite to perform supervised classification. The process repeated on multiple composites from previous years can help in understanding the trend of changes in glacier surface facies.

1.7.   Data availability

From the Sentinel-1 mission of ESA, a large pool of high configuration SAR data is available since 2014. This mission offers a temporal baseline of 12-days and 6-days over the Indian Himalayan Region. The region is covered during both ascending and descending passes of satellites. Although, the data from ascending nodes is available, it is sparse and irregular in the region. These datasets are available for use and can be freely downloaded from ESA's Copernicus Open Access Hub web portal (https://scihub.copernicus.eu/dhus/#/home).

1.8.   Thesis Outline/Structure

The complete thesis has been organized into 7 chapters. **Chapter 1** introduces the basic processes of glaciers and ice sheets along with a mention about the motivation for taking up this research, objectives and the innovation in this work. **Chapter 2** provide an overview on the scientific background of SAR, Differential SAR Interferometry for velocity estimation and Multi-Temporal SAR for classification.   **Chapter 3** includes details of the study area and datasets that are being used in the undertaken research. **Chapter 4** outlines the methods and steps adopted to achieve the research objectives. **Chapter 5** presents the results from the work and a report on analysis of the outputs. **Chapter 6** is a discussion on the results and analyses presented in the previous chapter. **Chapter 7** is a summary of inference from the research with answers to research questions put forth in the beginning, and further recommendations.

2.   SCIENTIFIC REVIEW

This chapter presents an overview on the use of satellite radar data for monitoring glacier dynamics, specifically glacier velocity and facies classification using Differential SAR Interferometry and Multi-temporal SAR approach. Starting with a brief background of how glacial studies gained importance, the chapter further discusses about the evolution of use of satellite radar in glaciology. A general introduction of Microwave remote sensing is followed by a review on its application for glacier surface velocity estimation and glacier facies classification.

2.1.   Evolution of Glacial Studies – Brief Introduction

Enhanced scientific understanding of climate dynamics and evolution has put light on factors that can indicate change. Glaciers, and other components of the Cryosphere, are considered to be vital indicators (Haeberli, Hoelzle, Paul, & Zemp, 2007; Houghton et al., 2001; Thompson, Mosley-Thompson, Davis, & Brecher, 2011) based on their sensitivity (Kääb et al., 2007; Kulkarni et al., 2011) and response to differential conditions of climate forcing (Vaughan et al., 2013), solar flux (Michael Zemp et al., 2015) and precipitation. While they are vital indicators, their responses are controlled by several factors (Benn & Evans, 2010; Pritchard, Arthern, Vaughan, & Edwards, 2009) making it difficult to understand and predict their behaviour. This challenge has led to initiation of several studies in glacial mass balance, surface velocity, areal extent, fluctuation of equilibrium line altitude (ELA), snout monitoring, sources and rates of accumulation and ablation among others.

Traditionally, field surveys were employed to ascertain changes in glacial behaviour. A series of stakes and pits on the glacier surface were crucial tools for quantification of mass loss and mass gain, in terms of snow water equivalent (SWE), from ablation and accumulation zones of the glacier (Hubbard & Glasser, 2005). Periodic theodolite measurements of the stake locations and their relative distance from nearby features such as lateral moraines were used to estimate glacier surface velocity (Cuffey & Paterson, 2010; Kodama & Mae, 1976). Monitoring of glacier snout using total station and D-GPS was helpful in understanding immediate glacier response to surrounding atmospheric conditions. Geomorphological mapping of lateral and terminal moraines were useful in understanding past glacial extents. These components help in understanding the glacial behaviour (Benn & Evans, 2010). Although field based estimates are highly reliable, it is not always possible to access glacier swaths due to rough terrain, inhospitable weather conditions and financial implications from labour and logistics (Bolch et al., 2012; L. Huang & Li, 2011). Due to this, field based glacier studies have been selective and limited, not evenly covering glaciers spread across the world.

Advent of remote sensing technologies has made it possible to study glacier dynamics with acceptable certainty, yet it can only partially substitute the significance of in-situ measurements (Bolch et al., 2012). Several optical sensors provide datasets at regular and high-revisit intervals. Analysis and interpretation of these datasets on regular intervals has made systematic monitoring of glacial changes possible. But, the passive optical sensors are sensitive to atmospheric conditions and cloud cover, making it difficult to sense ground features under adverse conditions and also during night time. Moreover, the requirement of an external source of illumination for such a system becomes an additional constraint. These limitations have

been overcome with modern Synthetic Aperture Radar (SAR) sensors. With ability to penetrate through the clouds, these active sensors can also operate throughout the day providing high resolution, surficial and structural information in addition to phase information of the ground objects. Initially developed during the Second World War, this technology has since been used in series of applications, including glacial studies.

2.2. Microwave Remote Sensing and Synthetic Aperture Radar (SAR)

Microwave remote sensing, commonly referred to as Radio Detection and Ranging (Radar), utilizes the radiation in microwave spectrum to retrieve information about the ground objects. This active remote sensing system works on the principle of scattering caused by interacting objects. The scattered radiation is partially returned to the sensor as 'Echo' or 'Backscatter', and is recorded for its amplitude and phase; where amplitude is a measure of energy reflected back to the sensor, and is a function of the object's geometry, surface roughness and dielectric properties (Ulaby, Moore, & Fung, 1981). Phase is a measure of the 2-way distance between the sensor and the object. This information can be put to use only when the sensors are side looking, helping to characterize and distinguish different objects on ground. Therefore, all the SAR sensors possess a side-looking imaging geometry (Moreira et al., 2013), as shown in **Figure 2.1**. The *look angle* is the off-nadir angle in which radar sensor looks at the surface; *incident angle* is measured between incident beam and the normal drawn to the interacting surface and *azimuth angle* is measured between the satellite track and look direction on the horizontal plane. Polarization of the backscattered wave is also recorded by the sensors, providing additional information for characterization of interacting objects. All this together has greatly enhanced the utility of microwave remote sensing in multitude of applications ranging
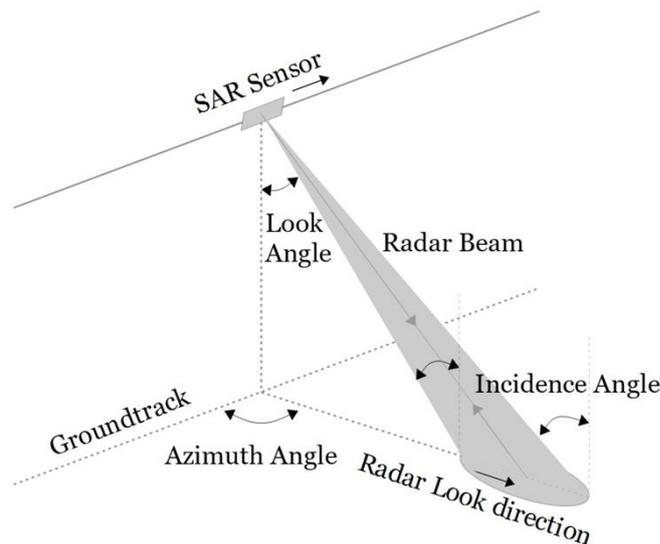
Figure 2.1: Side-looking Geometry of SAR Imaging Sensors. The direction of satellite movement is referred to as the azimuth direction and sensor look direction is referred to as the range direction. Due to side looking geometry, the cell sizes are different at near range and far range of the SAR image.

from detection, characterization, classification and mapping, to assessment of deformation and subsidence. Seasat, in 1978, was among the first civilian SAR systems to be launched. Since then, more than a dozen of SAR sensors have been deployed, revolutionizing the use of SAR in day to day applications (Moreira et al., 2013). Brief overview of satellite missions with SAR sensors is listed in **Table 2.1**. Apart from those mentioned, there are several more being developed to provide datasets of higher spatiotemporal configurations. Some of the commonly used SAR products include datasets from ERS1/2, RADARSAT1/2, ALOS-PALSAR1/2, ENVISAT, TerraSAR-X & TanDEM-X, RISAT-1 and the recently

launched Sentinel-1a and -1b. These sensors use either of the C band, L band or X band of the microwave spectrum for imaging. SAR analysis techniques like Interferometry (InSAR) for modelling of surface topography, Differential SAR Interferometry (DInSAR) for surface deformation and displacements and Polarimetry (PolSAR) for improved parameter retrieval were developed during the 80's and 90's (Gabriel et al., 1989; Joughin et al., 1995; Massonnet et al., 1993; Shi & Dozier, 1995). These techniques have greatly enhanced the significance of SAR systems and have catapulted research in related domains. Here, only applications relevant to glaciology are discussed.

Table 2.1: Overview of some SAR Satellite missions and their key characteristics

Satellite	Space Agency, Country	Years of operation	Band	Wavelength (cm)	Repeat Pass (days)	Polarization
Seasat	NASA, USA	1978	L-Band	23.5	3	HH
ERS-1	ESA, Europe	1991 - 2000	C-Band	5.6	3 to 35	HH
ERS-2	ESA, Europe	1995 - 2011	C-Band	5.6	35	HH
ERS -1/2 Tandem Mode	ESA, Europe	1995 - 1996	C-Band	5.6	1	HH
JERS - 1	JAXA, Japan	1992 - 1998	L-Band	23.5	44	HH
SIR - C / XSAR	NASA, USA	1994	L-Band	23.5	-	HH, HV, VV, VH
			C-Band	5.6	-	
	DLR, Germany	1994	X-Band	3	1	VV
Radarsat - 1	CSA, Canada	1995 - Today	C-Band	5.6	24	HH
SRTM	NASA, USA	2000	C-Band	5.6	-	HH, VV
	DLR, Germany		X-Band	3	-	VV
ENVISAT	ESA, Europe	2002 - 2012	C-Band	5.6	35	HH, HV, VV, VH
ALOS PALSAR - 1	JAXA, Japan	2006 - 2011	L-Band	23.5	45	Dual (HH, VV) / Quad
Radarsat - 2	CSA, Canada	2007 - Today	C-Band	5.5	24	HH, HV, VV, VH
TerraSAR - X	DLR, Germany	2007 - Today	X-Band	3.1	11	HH, HV, VV, VH
TanDEM - X	DLR, Germany	2010 - Today			11	
RISAT - 2	ISRO, India	2009 - Today	X-Band	3.1	14	Variable
RISAT - 1	ISRO, India	2012 - 2017	C-Band	5.6	25	Hybrid
ALOS PALSAR - 2	JAXA, Japan	2014 - today	L-Band	23.5	14	Variable
Sentinel-1a	ESA, Europe	2014 - today	C-Band	5.6	12	Variable
Sentinel-1b	ESA, Europe	2016 - today	C-Band	5.6	12	Variable
Sentinel-1 a/b	ESA, Europe	2016 - today	C-Band	5.6	3-6	VV, VH
NISAR	NASA, USA & ISRO, India	2021 (proposed)	L-Band	24	12	Variable
			S-Band	9.3		

2.3.   Snow, Ice and their interaction with Radar

Snow, ice and firn together make up the entire Cryosphere. Snow is a mass of several loosely packed crystals of ice having a density of 50-200kg m^{-3} which increases to 400-500kg m^{-3} upon metamorphosis (Armstrong & Brun, 2008). This denser form of snow is called firn, generally defined as a snowpack that has survived one melting season (Cuffey & Paterson, 2010). This further transforms into ice, which is closely packed with negligible pockets of air and water, having a density of 800-900kg m^{-3} (Armstrong & Brun, 2008; Cuffey & Paterson, 2010). They also differ in the size and shapes of the crystals, water content, dielectric properties and internal temperature (Müller, 2011). Each of these have a variable response to incident radiations (European Space Agency, 2014).
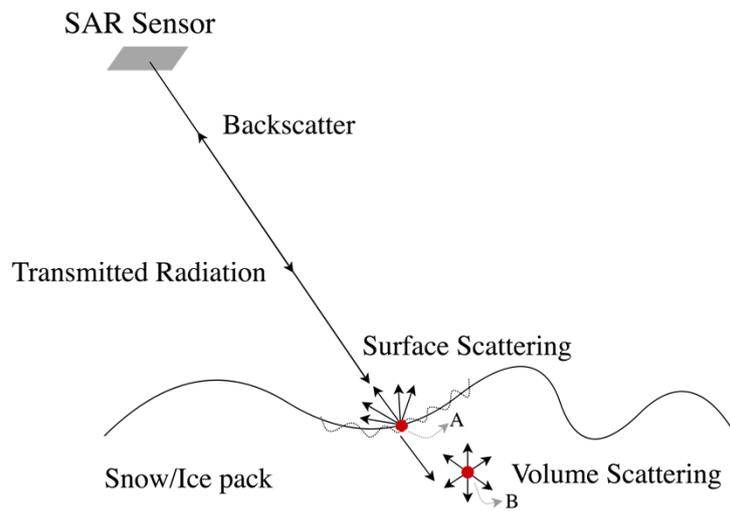
Figure 2.2: Scattering mechanisms in a snow/ice pack. The dotted-curvy line at the surface is the representation of surface roughness. The points A and B represent the phase center from surface and volume scattering respectively.

Transmission of microwave through heterogeneous medium experiences attenuations due to scattering and absorption, thereby controlling the extent of penetration in the medium. While absorption occurs due to electrical conductivity and di-electric properties, scattering is caused by homogeneity and heterogeneity (Ulaby et al., 1981) of the medium. Higher the degree of heterogeneity, greater is the loss of backscatter energy. Scattering (**Figure 2.2**) may occur either as surface scattering, as in case of wet or smooth layered objects, or volume scattering, where the radiation penetrates as a result of lower attenuations at the surface (Ulaby et al., 1981). Degree of penetration is also a function of radar wavelengths, with longer wavelength radiations (e.g. L Band) penetrating deeper than those with shorter wavelengths (e.g. C Band)(Rignot, Echelmeyer, & Krabill, 2001). While this ability offers more information about the sub-surface, its sensitivity to surface variations slightly decreases. This nature of longwave radiation sensors can be exploited for InSAR applications over larger temporal baselines, where higher coherence is retained between the two acquisitions (Rignot et al., 2001). But, the phase center, the point from which the return wave appears to have originated (Green, 2008), may be different (as seen in **Figure 2.2**) based on penetration ability, which has to be taken care.

Microwaves are transvers in nature, and vibrate in directions perpendicular to the direction of propagation (Paul, 1998). This property of polarization is independent of its wavelength (European Space Agency, 2014). Modern sensors are developed to record and store the polarization information of backscatter, which can further be decomposed to retrieve crucial scattering properties of the ground object (Cloude, 2009; Moreira et al., 2013). The backscattered wave may be co-polarized (HH, VV), cross-polarized (HV, VH) or a

combination of both, quad-polarized (HH, HV, VH, VV). Different forms of snow and ice have a variable response towards polarizing the backscattered wave (Forster, Isacks, & Das, 1996). Water content in the snow/ice pack, grain size and roughness are factors that can affect the polarization of the backscattered wave. This phenomenon has been exploited for classification of glacier facies (Callegari et al., 2016; L. Huang et al., 2011; Jiancheng Shi, Dozier, & Rott, 1994; Parrella, Fischer, Hajnsek, & Papathanassiou, 2018; Sood, 2014).

A typical glacier is generally composed of dry snow, wet snow and ice with increasing temperature as we move from the accumulation (higher elevation) to the ablation zone (lower elevation). For a given radar wavelength, penetration is higher in dry snow and lower in wet snow. Due to high water content of ice, penetration is relatively poor. Volume scattering is generally dominant in snow covered areas of the glacier and surface scattering occurs in the ice covered regions. Penetration during the night time increases due to the refreezing of water pockets in the snow/ice pack. Rott, Sturm, & Miller (1993) derived penetration depths for dry snow in C-Band (λ=~5.6cms) and X-Band (λ=~12.6cms) and reported to be 21.7m and 10.4m respectively. In another study, they also reported that penetration in dry snow is in the order of 10m at 10GHz and decreases to 1m at 40GHz (Rott, Domik, & Matzler, 1985). Ice clearly has lower penetration in the same frequencies due to higher liquid water content. Penetration depths of 20-27m in dry snow were reported by Weber Hoen & Zebker (2000) for C-band. Degree of backscatter signal in glacier ice is dominated by surface scattering, as a function of roughness and wavelength. In dry snow regions, the backscatter signals are partially from air-snow boundary layer and from in-homogeneities under the snow surface. Also, the roughness of surface ice is significantly higher than snow, causing the backscatter to be high. However, it is difficult to accurately and completely understand snow and ice responses to radar signals (Rott et al., 1985).

2.4. Glacier Surface Velocity Estimation Using SAR Techniques

Surface motion of glaciers and ice sheets from space can be derived with high precision using Synthetic Aperture Radar (SAR) (Gabriel et al., 1989; Joughin, Kwok, & Fahnestock, 1998; Kumar, Venkataraman, Larsen, & Hogda, 2011; Li et al., 2018; Mouginot, Rignot, Scheuchl, & Millan, 2017; Mouginot, Scheuch, & Rignot, 2012; Satyabala, 2016; Varugu, Singh, & Rao, 2015). It has emerged to be a preferred tool for investigation of flow velocities (Joughin, Smith, & Abdalati, 2010; Mouginot et al., 2017) due to their spatiotemporal resolution and its ability to function irrespective of daylight and cloud cover. Availability of datasets of different wavelengths (L-Band, X-Band, C-Band) has fuelled extensive studies investigating surface velocities in Antarctica (Giles, Massom, & Warner, 2009; Goldstein et al., 1993; Moll & Braun, 2006; Mouginot et al., 2012), Greenland (Joughin et al., 2010, 1995; Mouginot et al., 2017; Nagler, Rott, Hetzenecker, Wuite, & Potin, 2015) and The Himalayas (Kumar, Venkataraman, & Høgda, 2011; Kumar, Venkataraman, Høgda, & Larsen, 2013; Satyabala, 2016; Sood, 2014; Thakur, Dixit, Chouksey, Aggarwal, & Kumar, 2016; Varugu et al., 2015).

Two common approaches for deriving across-glacier surface velocity maps are 1) Differential SAR Interferometry (DInSAR) and Offset tracking (Cuffey & Paterson, 2010; Massonnet & Feigl, 1998). While both approaches are useful tools for generating surface displacement vectors, DInSAR has the ability to map displacements up to mm scales (Gabriel et al., 1989). However, in both cases, decorrelation between two images may lead to unreliable estimates.

2.4.1.   Differential Interferometry (DInSAR)

Interferometric Synthetic Aperture Radar (InSAR) exploits the phase for mapping topographic information of the ground surface (Hanssen, 2001). Two scenes from slightly different viewing geometries (**Figure 2.3**), taken using 2 antennae or from repeat passes are required for this process. When a temporal baseline (ΔT) is introduced to this approach, deformation of surface objects can be mapped. But in presence of an effective spatiotemporal baseline (B_S, ΔT), which generally is the case, the deformation signals are mixed with topographic signals. This requires an additional step of interferometric processing called the Differential SAR Interferometry (DInSAR). In this technique, the topographic phase is eliminated from the interferogram using an external topographic model (e.g. DEM) (Massonnet et al., 1993) or a third pass (Zebker, Rosen, Goldstein, Gabriel, & Werner, 1994), leaving behind only the differential phase or the
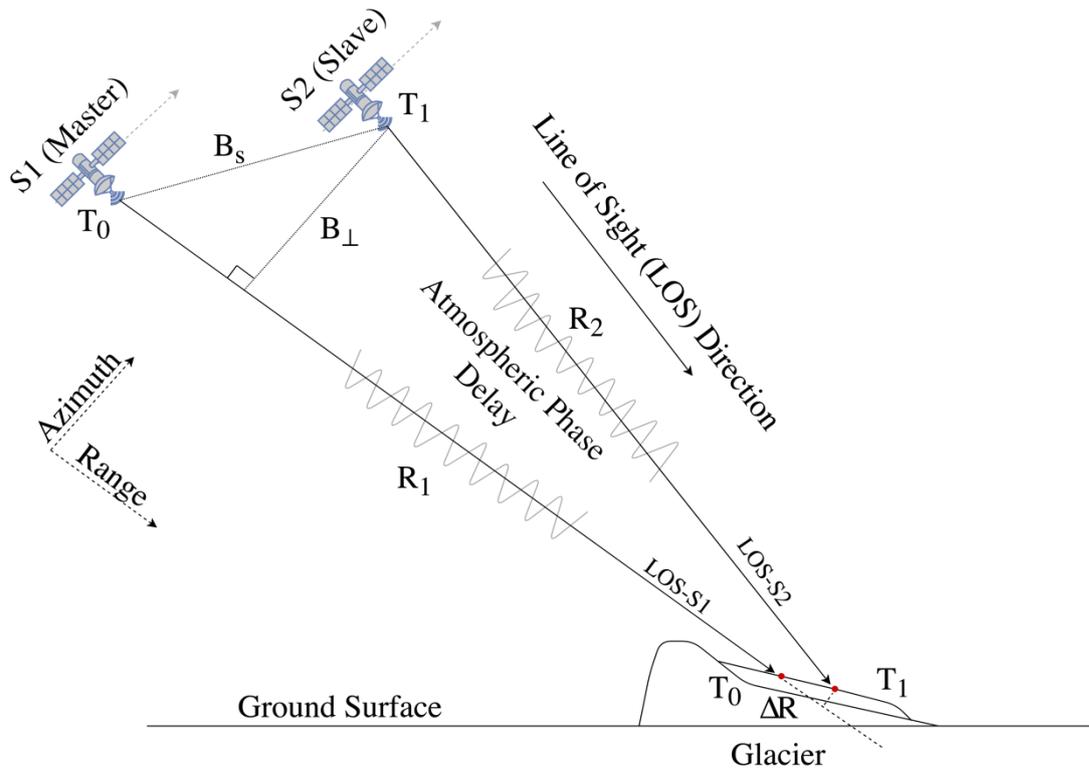
Figure 2.3: Satellite imaging geometry for DInSAR. B_S=Spatial Baseline; $B_\perp$=Perpendicular baseline; T_0-T_1=Temporal Baseline (ΔT); ΔR=Range Difference in slant range direction of the master (LOS-S1); R_1, R_2 = Range of S1; S2; S1, S2 = Satellite positions and LOS-S1, LOS-S2 = Line of sight directions of S1 & S2.

differential interferogram (Gabriel et al., 1989). But, the phase change ($\Delta\varphi$) (eq. 2.1) seen in the interferogram is also contributed by phase delay from earth's curvature ($\Delta\varphi_{flat\ earth}$), atmosphere ($\Delta\varphi_{atmosphere}$) and noise ($\Delta\varphi_{noise}$) apart from topography ($\Delta\varphi_{topography}$) and displacement ($\Delta\varphi_{displacement}$). To precisely extract only the phase due to deformation, other phase contributions should be eliminated.

$$\Delta\varphi = W\ (\Delta\varphi_{flat\ earth} + \Delta\varphi_{topography} + \Delta\varphi_{displacement} + \Delta\varphi_{atmosphere} + \Delta\varphi_{noise}) \qquad (2.1)$$

Where 'W' is the wrapping function. For elimination of flat earth, the orbital information from the metadata may be used. Topography phase can be removed using the two processes discussed above. Removing the

atmospheric phase requires additional meteorological data for modelling atmospheric conditions. Alternatively, atmospheric phase and noise can be eliminated by time series InSAR techniques, e.g. Persistent Scatterer Interferometry (PSI) (Ferretti, Prati, & Rocca, 2000, 2001).

Unwrapping (Chen & Zebker, 2002) of the differential interferogram can provide a measure of relative deformation specified to one dimensional Line of Sight (LOS) direction (indicated in **Figure 2.3**). For deriving multi-dimensional information, additional interferometric pairs, having different viewing geometries, are required. Such pairs can be acquired from ascending and descending passes for two dimensional information, assuming that the ice flow is parallel to the surface (no deformation in the third dimension) (Joughin et al., 1998; Mohr, Reeh, & Madsen, 1998). This information can be processed further to decompose the LOS vectors to actual surface velocity information.

The applicability of DInSAR greatly depends on the degree of coherence between the image pair (Euillades et al., 2016). Choosing pairs with smaller spatiotemporal baseline may assure higher coherence, considering similar reflectivity characteristics of ground objects. Decorrelation is introduced when 1) volume scattering dominates the image area, 2) ground objects change their scattering behaviour between the acquisitions, and 3) significant difference in look angle (Ferretti, Monti-Guarnieri, Prati, & Rocca, 2007). Depending on the radiation wavelength, degree of decorrelation may vary. Generally, L-Band acquisitions are more suitable for studies requiring repeat-pass measurements, due to their lower sensitivity towards temporal changes in the scattering mechanism (Hanssen, 2001). It is suggested to use closest spatiotemporal baseline for best interferometry results.

DInSAR technique has been widely used for mapping glacier and ice sheet velocities in the Antarctic (Goldstein et al., 1993; Joughin et al., 2010; Moll & Braun, 2006; Mouginot et al., 2017; Rignot, 1998; Rignot, Jacobs, Mouginot, & Scheuchl, 2013), Greenland (Joughin et al., 1998, 2010, 1995; Kwok & Fahnestock, 1996; Rignot, Jezek, & Sohn, 1995) and other regions (Eldhuset, Andersen, Hauge, Isaksson, & Weydahl, 2003; Kumar, Venkataraman, & Høgda, 2011; Kumar et al., 2013; Kumar, Venkataraman, Larsen, et al., 2011; Mattar et al., 1998; Prats, Scheiber, Reigher, Andres, & Horn, 2009; Sánchez-Gámez & Navarro, 2017; Schneevoigt, Sund, Bogren, Kääb, & Weydahl, 2012; Sood, 2014; Thakur et al., 2016; Varugu et al., 2015; Wangensteen et al., 2005), viz. Svalbard, the Himalayas, Alps and the Andes.

In the first, Gabriel et al. (1989) used DInSAR for mapping swelling of ground surfaces due to water absorbing clays in Imperial Valley, California. They were able to map minute swellings of ~1cm to 10m in 3-6 days, caused due to watering of agricultural fields, using Seasat datasets from 1978. A similar study was performed by Massonnet et al. (1993) to map displacement caused due to 1992 earthquake at Landers, California. Study performed by Goldstein et al., (1993) on the Rutford Ice Stream in West Antarctic Ice Sheet was among the first applications of DInSAR on estimation of horizontal ice-flow velocities. They observed the detection limits to be 1.5mm and 4mm in vertical and horizontal directions respectively, with respect to radar LOS direction. Upon comparison with ground measurements, a decrease of 2% in ice-flow velocity was reported between 1978-80 and 1992.

Launch of ERS-1 in 1991 by European Space Agency provided first set of synoptic imageries for studying ice-motion of glaciers and ice-sheets in Greenland. Rignot et al. (1995) used these datasets to estimate ice flow measurements on the western flank of Greenland Ice Sheet. Their results were reported to be within 6% of field velocity estimates collected over a 40km survey stretch. A similar study was carried out by Joughin et al. (1995) and LOS displacements from a 3-day interferogram were decomposed to horizontal and vertical components. Wangensteen et al. (2005) were able to project the LOS displacement onto actual surface displacement using the relationship,

$$V_{glac} = \frac{V_{los}}{(cos\alpha \; cos\xi \; sin\theta + \; cos\theta \; sin\alpha \;)} \tag{2.2}$$

where V_{glac} is the actual surface velocity in flow direction, V_{los} is the velocity in LOS direction and α, ξ, θ are the slope, aspect angle with respect to radar beam direction and look angle respectively (**Figure 2.4**).
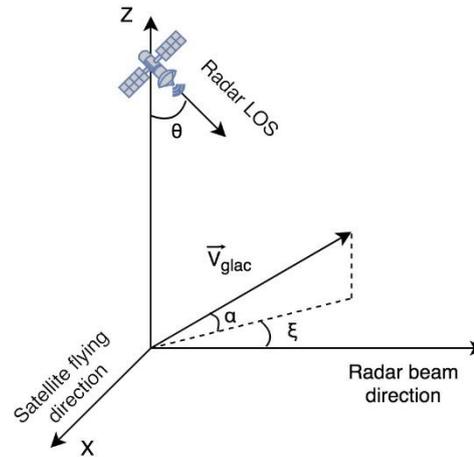
Figure 2.4: Illustration of Surface velocity from InSAR geometry where α is slope, ξ is angle between glacier movement direction and radar beam direction and θ look angle. V_{glac} vector represents the direction of glacier movement.

The velocity estimated by DInSAR method is a vector in the LOS direction, derived using single interferometric pair (Goldstein et al., 1993). Joughin et al. (1998) and Mohr et al. (1998) presented a combined approach for inferring 3 dimensional velocity from Differential Interferometry. Using pairs from ascending and descending passes and assuming surface parallel flow, full 3 dimensional flow pattern can be modelled. LOS vectors of every pixel from ascending and descending pairs are resampled to geographic coordinates. Joughin et al. (1998) have detailed the entire process and presented results from Ryder Glacier in Greenland. They have observed that velocities are highest at the termini, several kilometres per year, while they are much slower, few meters per year, around the summit of the glacier. Although, the study was performed using ERS-1/2 datasets with 1 day and 3 day temporal baseline, shorter temporal baselines may be required for fast moving glaciers. Mohr et al. (1998) were able to validate their results of 3D displacement from Storstrommen Glacier from northeastern Greenland. It was reported that the 3D-DInSAR results, construted using datasets from ERS 1/2 tandem mode, correlated well with the GPS measurements. Flow velocities from 2m yr^{-1} to 250m yr^{-1} were observed. The direction of flow from InSAR agreed with all ground stakes that had velocities > ~20m yr^{-1}. In both the studies it was observed that, in certain glaciers (ex. Surging glaciers) it may not be correct to assume surface parellel flow, but the assumption and 3D displacement information have the potential to significantly enhance our understanding of dynamic glacier movement.

Glacier or ice cap surfaces that are affected by wind may experience temporal decorrelation (Moll & Braun, 2006). Similar challenge was encountered by Moll & Braun, (2006) during interferometric processing of 19 pairs of ERS-1/2 datasets with 1 day temporal baseline in the Glaciers of King George Island in Antarctica. Out of 19 pairs, only 2 pairs exhibited high degree of coherence. 6 other pairs had partially good coherence and were considered usable for DInSAR processing. Due to decorrelation from rapid melt and wind drifting, the results were hampered with inaccuracies. Where external elevation information with GCP was available, the results were improved to better accuracy. Eldhuset et al. (2003) have presented a combined use of one-day interferometric pairs along with photogrammetric tools and ground measurements to obtain reliable

velocity estimates for a fast moving glacier in Svalbard – Kronebreen Glacier (2m day^{-1}). Using C-band ERS-1/2 images, they were able to draw interferograms with coherence values close to 1. They found highest coherence during low melt season (August). A velocity of 0.5m day^{-1} was observed at upper part of the glacier. The central part of the glacier (5-10km from the snout) had a velocity of 2m day^{-1} which reduced to ~1m day^{-1} towards the snout. Wangensteen et al. (2005) estimated LOS velocity for 3 glaciers in Svalbard - Isachsenfonna, Akademikerbreen and Nordbreen. The estimated velocities (v_r) were further decomposed in the flow direction of the glacier (v) using slope(α), aspect angle with respect to radar direction(ξ), look angle(θ) and the velocity in LOS direction. The relationship is given in eq 2.1 (Kwok & Fahnestock, 1996).

The maximum and average velocities for Isachsenfonna glacier are 0.42m d^{-1} and 0.23m d^{-1} measured during January 1996. In April 1996, the velocities were 0.42m d^{-1} and 0.18m d^{-1} respectively. It was observed that the velocities on Nordbreen were reportedly slower, around 0.35m d^{-1} and 0.14m d^{-1} maximum and average velocities respectively. Akademikerbreen Glacier reported a maximum velocity of 0.41m d^{-1} and an average velocity of 0.07m d^{-1} during the similar period.

Hu, Li, Zhu, Ren, & Ding (2010) presented a new method for deriving 3D velocities of glacier surfaces using a combination of DInSAR and Offset tracking methods. Using pairs from ascending and descending passes, the LOS velocities are measured. Subsequently, displacement in azimuth direction is estimated using offset tracking. All the 4 independent vector components are combined using the method of least squares and Helmert variance component estimation. A similar approach was used by Sánchez-Gámez & Navarro (2017) for estimating 3 dimensional velocity of Southern Ellesmere Ice caps in Canadian Arctic.

Using InSAR, few studies were performed for the glaciers of Himalayan Region (Strozzi, Luckman, Murray, Wegmuller, & Werner, 2002). This may be due to lack of datasets with required revisit intervals and decorrelation from rapid movement of glaciers. Among the first studies in the Himalayas was by Venkataraman, Rao, & Rao, (2006). They used ENVISAT and ERS-1/2 datasets for DInSAR analyses and observed ERS-1/2 datasets with 1 day temporal baseline were favourable. Interferograms constructed using ASAR datasets had poor coherence (due to long temporal baseline), hence weren't applicable for interferometric processing in the Himalayan region. DEM generated using ERS-1/2 and the velocity estimated for 2 major glaciers – Gangotri and Siachen Glacier seemed reliable. In another instance (Kumar, Venkataraman, & Høgda, 2011) use of ERS-1/2 datasets produced accurate velocity vectors for Siachen Glacier in the Western Himalayas. But the limited availability of datasets with 1-day baseline, only limited to a few pairs of scenes in 1995-1996, makes it impossible to study velocity changes for later time periods. Several other studies were performed (Sood, 2014; Thakur et al., 2016) using the ERS-1/2 data of 1-day interval from 1995-1996.

Upon launch of X-Band TerraSAR-X sensor in 2007, Kumar, Venkataraman, Larsen, et al. (2011) experimented with its applicability of DInSAR processing in the Himalayan Region. The 11-day temporal separation and the lower wavelength (3.1cm) caused extensive loss of coherence, making it inapplicable for the rapidly melting Himalayan glaciers. Instruments with longer wavelengths (e.g. L Band) and with higher revisit frequencies (~2-4 days) can provide optimal base for interferometric processing in the Himalayan region.

After launch of Sentinel-1b satellite, 6 day separated interferometric pairs have been available. Jauvin, Yan, Trouve, & Fruneau (2018) processed 6 day interferograms from October 2016-April 2017 for glaciers along the Mont Blanc Massif, French Alps. They found acceptable coherence even at lower altitudes during the cold season. The results obtained were similar to those from DInSAR processing from 1996 using ERS

datasets. Sánchez-Gámez & Navarro (2017) presented the potential of Sentinel-1 datasets for mapping movements of slow moving glaciers in the Canadian Arctic with desirable accuracy.

Datasets from these instruments provide opportunity for obtaining better results through interferometric processing for alpine glaciers (Jauvin et al. 2018), as in the Himalayas. Moreover, these datasets are freely available and can be downloaded from https://scihub.copernicus.eu/dhus/#/home. Although, L-band sensors were launched (ALOS-PalSAR-1, ALOS-PalSAR-2), they are either readily unavailable or they have lower revisit frequencies. Role and applicability of Sentinel-1a/b datasets for interferometric processing to derive glacier surface velocities should be accessed for the Himalayan glaciers.

2.5.   Glacier Facies Classification using SAR Datasets

The sensitivity of radar backscatter to minute variations in geophysical properties of ground objects makes it a preferred tool for identification and classification of glacier facies. Variations in glacier facies potentially represent the response to surrounding climate (Forster et al., 1996), and regular monitoring of these variations can convey ample information about glacier behaviour and stability. Snow line and the equilibrium line altitude (ELA) can be easily identified from multi-temporal assessment of glacier facies (L. Huang et al., 2011). While optical images are preferred for classifications, they are limited by the cloud cover present in the images. SAR products using Polarimetry SAR (PolSAR) approach and multi-temporal SAR approach have been used for glacier facies classification. The characteristic backscatter from different snow forms and stages of ice crystallization permits identification of different glacier facies, viz. the dry snow facies, percolation facies, wet snow facies, superimposed ice facies and ablation facies (Cuffey & Paterson, 2010), represented in **Figure 2.5**. The properties of each of these zones are briefly discussed below:
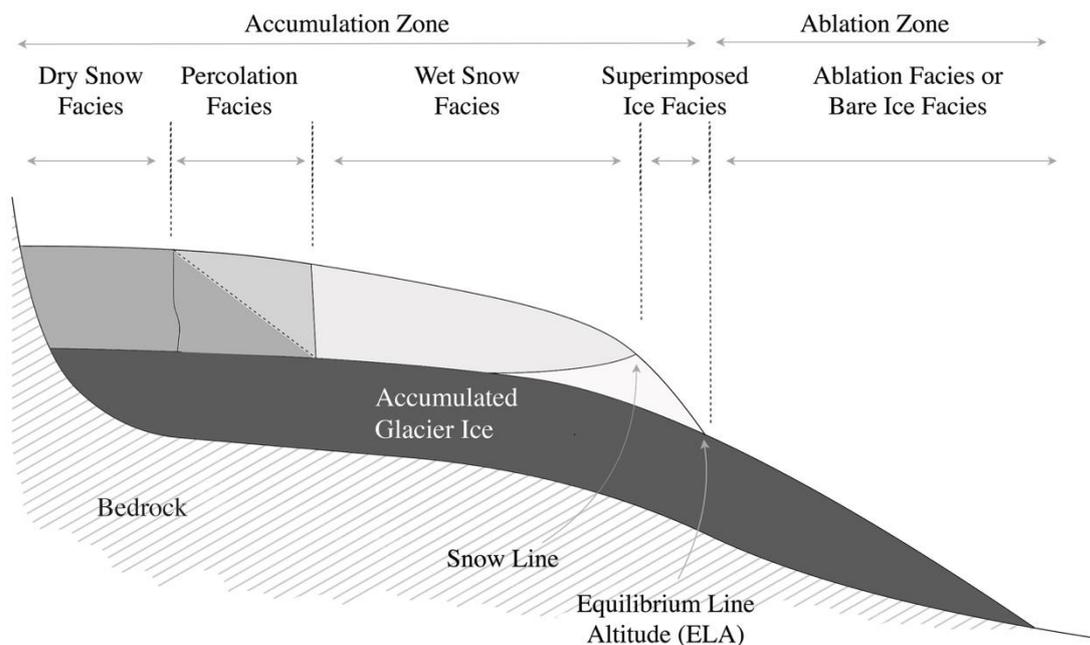
Figure 2.5: Cross-sectional illustration of a typical glacier representing different radar glacier facies on a glacier surface. The dry snow, percolation, wet snow and superimposed ice facies together form the accumulation zone, while the bare ice facies forms the ablation zone, separated by Equilibrium Line Altitude (ELA).

Dry Snow Facies: Characterized by dry snow flakes, no melting occurs in this part of the glacier throughout the year. Generally found in extreme cold regions like ice sheets of Greenland and Antarctica, this zone can rarely be seen in high altitude glaciers. With time, the dry snow gets compacted under its own weight and due to deposition of additional mass of snow from winds and storms. Volume scattering is dominant in this region, and radiations penetrate up to 20m deep into a dry snow pack (König, Winther, & Isaksson, 2001). Therefore, this region appears dark in SAR images (Partington, 1998). This facies is normally absent in Himalayan Glaciers as temperatures may hover around ~0°C during summer periods.

Percolation Facies: Dry snow that accumulates over monsoon and winter periods is subjected to surface melting leading to percolation and refreezing of meltwater, causing formation of horizontal ice lenses and vertical ice glands (Cuffey & Paterson, 2010). Melting is further forced by the latent heat released by refreezing of meltwater. The presence of ice lenses, amid the dry snow packs, formed due to occasional melting causes backscatter to be high during winter, which significantly reduces in summer due to presence of meltwater on the surface (König et al., 2001).

Wet Snow Facies: This zone is characterized by melting of entire annual accumulation and refreezing. Grain sizes in this facies are larger due to crystallization and recrystallization of ice. Where melting is excessive, an area of slush is developed (Cuffey & Paterson, 2010). Although water content is minimal, it significantly alters the penetration ability of the radiation and therefore the predominant scattering mechanism shifts from volume scattering to surface scattering. In SAR images, this zone appears dark during winter and bright during spring and summer.

Superimposed Ice Facies: Ice lenses are extensively formed in this zone due to refreezing of the excessive meltwater, available from melting of wet snow packs. They are high in density and start immediately below the wet snow zone (Cuffey & Paterson, 2010). The line differentiating the two facies is called the 'Snow line', identified during the end of ablation season. Apparently, during heavy ablation years or regions where ablation is excessive (Himalayan Regions), refreezing may be minimal which would also eventually melt leaving no layer of superimposed ice (Partington, 1998). The backscatter of Superimposed Ice Facies is similar to bare ice facies due to similar composition, and can be differentiated using the degree of smoothness which is higher in superimposed ice.

Ablation Zone or Bare Ice Facies: This zone is the lowest part of the glacier or an ice sheet, and consists of exposed rough ice facies. This character helps in distinction of bare ice from superimposed ice. More than the accumulated mass is lost to melting in this part of the glacier. Dry snow, that is present in winter, causes backscatter to be low, which further lowers with time due to melting of snow pack. During summer, after the seasonal snow has completely melted, higher backscatter is observed. The line of separation between superimposed ice facies and bare ice facies is referred to as the equilibrium line altitude (ELA), which in absence of superimposed ice facies (as in some of the Himalayan Glaciers) is located between bare ice and wet snow facies.

The applicability of non-polarized SAR products for classification of glacier facies was demonstrated for the first time by Partington (1998). Using 3 SAR images, from winter, early summer and late summer, ice sheet from Greenland could be successfully classified into 5 facies as described above. Although simple, the technique requires use of multiple SAR datasets. The image from winter represents the maximum dry conditions, while that from late summer represents the areas of melt, making them the key elements for the approach. Usage of these three images for creation of a RGB composite helps in visualization of multi-temporal signatures, which forms the basis for classification of glacier facies. Further, this approach also helps in detection of the snow line and equilibrium line altitude, which may be critical components to

understand glacier health. Even though the approach is effective and produces reliable results, it has been used in very few studies. Sood (2014) used multi-temporal SAR approach for classification of Samudra-Tapu glacier in the Western Himalayas using this method and found that this approach performed better in classification than other PolSAR decomposition and classification methods. RISAT-I MRS datasets of HH polarization were used for the study. Thakur et al. (2017) used multi-temporal SAR and PolSAR approach for classification of zone on Gangotri Glacier and Samudra Tapu glacier with a classification accuracy of 82-90%.

2.6.   Summary

In the past few years, several studies have been undertaken using optical and radar products for classification of glacier facies and retrieving surface velocities. From the review presented in this chapter, it may be asserted that radar products have gained importance for glacial applications, considering their configurations and ability to function in poor weather conditions. The differential scattering properties of snow, firn and ice and the phase information that are recorded by SAR sensors is of crucial use to delineate glacier facies and assess surface movements.

DInSAR is a robust and reliable method for assessment of glacier velocities offering millimetre-level estimates. The method is highly applicable to stable glaciers and ice-caps from the polar regions, but may not be best suitable for alpine glaciers. Glaciers from the Himalayas are highly dynamic, crevassed, undergoing rapid melt and debris covered. For such glaciers SAR instruments with longer wavelengths and high revisit frequencies are required. Ensuring smaller spatiotemporal baseline can preserve coherence between the master and the slave images. Also longer wavelength radiations (e.g. L-Band) that are less sensitive to surface scattering, can enhance the degree of coherence. Therefore, a SAR constellation that has longer wavelengths ($\lambda > 24cm$) and higher revisit frequency (2-4 days) would be optimal for monitoring highly dynamic glacial systems as in the Himalayas. Launch of Sentinel-1 mission has opened up opportunities for interferometric processing of Himalayan glaciers. As Sentinel-1 products are either single or dual polarized, these datasets can be effectively utilized for classification of glacier facies using multi-temporal SAR approach. Further, this also permits the identification of ELA, which may be critical to understanding of glacier status. As Sentinel-1 data is available for 4 consecutive years (2014 – 2018), a time series analysis can be performed to assess the changes that have occurred over these years.

3.   STUDY AREA AND DATASETS

This chapter presents information on the study area chosen to achieve the research objectives. Also, the datasets, with a brief highlight on their characteristics, that were used to carry out the work are listed along with their key acquisition parameters.
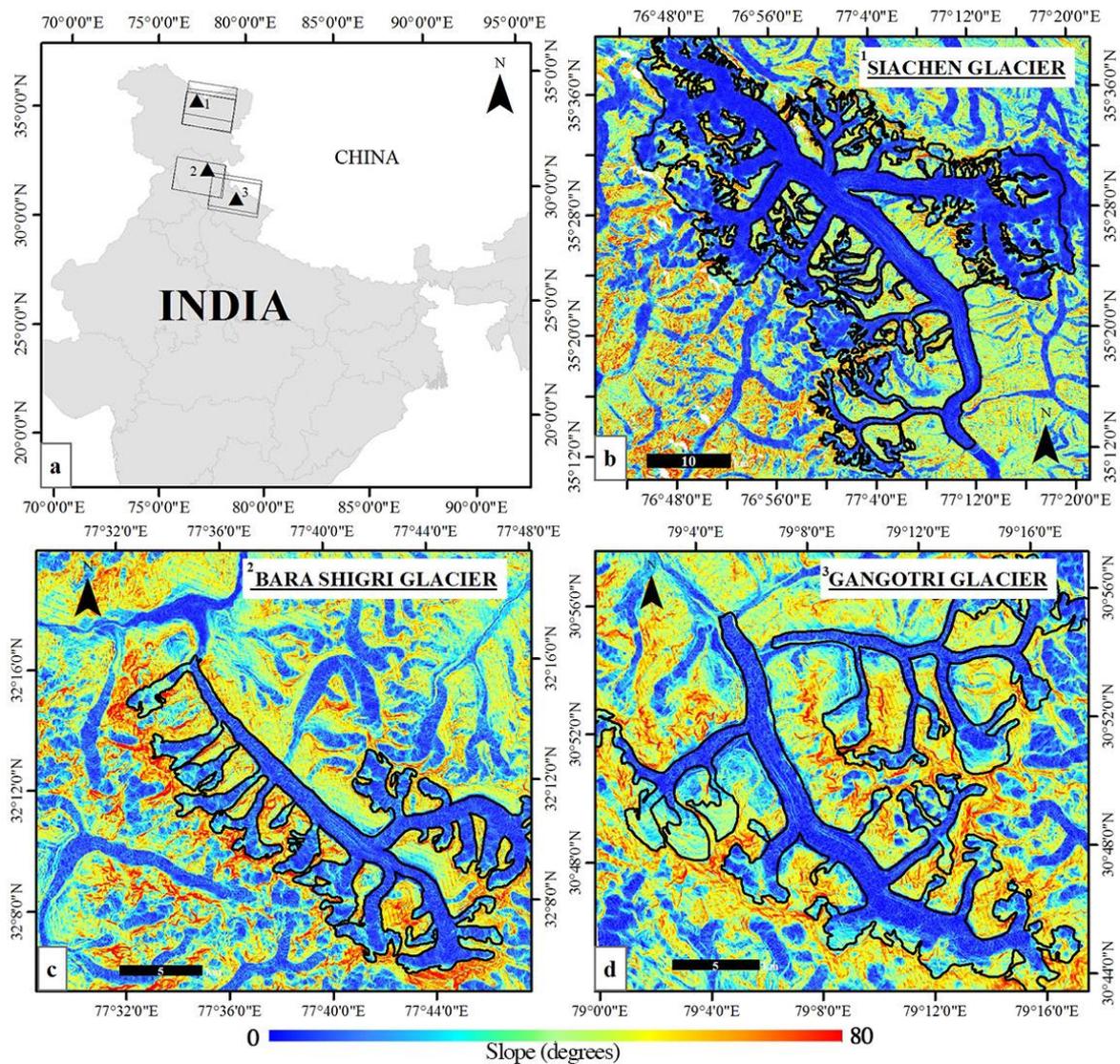
Figure 3.1: Illustration of the study area. a) Outline of India with geographic location of Siachen Glacier (1), Bara Shigri Glacier (2) and Gangotri Glacier (3). The outlines of the adopted S1a/b scenes from Descending Pass are presented using rectangular polygons on the image; b) Map of Siachen Glacier; c) Maps of Chhota (Left) and Bara Shigri Glacier (Right); d) Map of Gangotri Glacier. The glacier outlines are overlaid on the slope maps.

3.1.   Description of the Study Area – Indian Himalayan Region

This study focusses on the Indian Himalayan Region (IHR), specifically the Western Himalayas.

The Himalayas, beginning from the Karakoram in the west, passing through Pakistan, India, Nepal, Bhutan and China, is the biggest and the longest mountain range in the world. Housing the largest mass of glaciers outside the Arctic and the Antarctic, this region forms an integral part of the 'Third Pole' (Yao et al., 2012) along with other mountain ranges of Pamir, Hindu-Kush, Kunlun and Tien Shan. Storing freshwater reserves that feed downstream ecosystems, these mountains also play a crucial role in regulation of regional weather and climate. Along its swaths, they are exposed to different climate regimes and characterized by heterogeneous ecology and geographic features. For the length of Himalayas, and the varying climatic conditions that they are exposed to, the mountain range is sub-divided into 3 sub-ranges – The Western, the Central and the Eastern Himalayan Range. Glaciers in this region are affected by various regional and global factors, making them dynamic and sensitive, at the same time difficult to understand.

In this study, we have chosen 3 glaciers from the Western Himalayan Range (**Figure 3.1**) – 1) Siachen Glacier located in the North, 2) Bara Shigri Glacier from the centre and 3) Gangotri Glacier from the east of the region.

3.1.1.   Siachen Glacier

Located in the Karakoram Range of the North-Western Himalayas, Siachen Glacier (N35°31'18.08" and E76°57'3.77") is the longest glacier in Asia spanning for a length of ~72km. It is also the second longest valley glacier in the world, outside the polar regions, extending in the northwest-southeast direction. The snout of the glacier is located at 3670m.a.s.l., while the highest point in the accumulation zone is located at ~7200m.a.s.l. The melt waters from this glacier feeds the Shylok River, which is an important river system in region.

Precipitation by the western disturbances accounts for most of the accumulation of mass in the glacier. Influence of summer monsoon in this region is minimal. During winter periods continuous snowfall is observed with temperatures ranging between -10°C to -50°C. Dimri & Dash (2010), in their study on winter temperature & precipitation trends, have reported non-homogenous response of temperature to climate change and local atmospheric stress across the glacier surface, along with shrinkage in accumulation zone of the glacier between 1984 and 2006. The location and the outline of the glacier are illustrated in **Figure 3.1a and b** respectively.

3.1.2.   Bara Shigri Glacier

A few hundred kilometres, towards the south of Siachen Glacier is the Bara Shigri Glacier (N32° 9'38.48" and E77°41'31.95"). Located in the Chandra River Basin of the Lahaul-Spiti Valley, this glacier is highly debris covered with much of its ablation zone being covered by debris. This makes it difficult to access the glacier by foot, hence very few field based studies have been performed on this glacier in the past. The elevation varies from 3975m.a.s.l at the snout to 6250m.a.s.l at the highest point in the accumulation zone, with a length of 27.2km between them. Melt water from this glacier drains into Chandra River, which is one of the tributaries of River Indus.

This region is located in the monsoon-arid transition zone, characterized by influence from Indian Monsoonal Winds during summer and Westerlies during winter (Bookhagen & Burbank, 2010). Both wind systems contribute towards accumulation of glacier mass. Automatic weather station (located at 4863 m.a.s.l) data reported by Azam et al. (2014) for a nearby region shows a temperature of 4.3°C during August and -15.8°C during January, which are reported as the warmest and the coldest temperatures observed between 2009 and 2013. Garg, Shukla, Tiwari, & Jasrotia, (2017) reported formation of numerous supraglacial lakes and enormous down-wasting of mass through melting over this glacier. The location of the glacier and its outline are represented in **Figure 3.1a and c** respectively.

3.1.3. Gangotri Glacier

Feeding one of the most important rivers in the region, Gangotri Glacier (N30°50'49.34" and E79° 6'35.44") is complex glacier system with several tributaries, namely Kirti, Swachchand, Ghanolim and Maiandi, feeding the glacier along its length. Three other glaciers, Meru, Chaturangi and Raktavarn were also connected to the glacier in the past, but now remain disconnected due to continuous retreat (Bhattacharya et al., 2016). With a length of 29km, Gangotri glacier extends from 4066m.a.s.l at the snout to 5910m.a.s.l at the accumulation zone of the glacier. Debris cover in the lower ablation zone is prominent and covers almost one third of the entire glacier area. This glacier is a widely studied glacier (e.g. Bhattacharya et al., 2016; Gantayat, Kulkarni, & Srinivasan, 2014; Gupta, Haritashya, & Singh, 2005; Satyabala 2016), yet its dynamics are not completely understood, due to its complexity and dynamicity. With a northward orientation, meltwater from this glacier flows into the Bhagirathi River which further joins Alaknanda to form the holy River Ganges.

Both, Indian Monsoon and Westerlies, contribute to precipitation in the glacier region during the summer and winter periods respectively. Average annual maximum and minimum temperatures recorded by the meteorological observatory 3km away from the snout are reported to be 11°C and -2.3°C respectively (Bhambri, Bolch, Chaujar, & Kulshreshtha, 2011). The location of Gangotri glacier and its physical boundaries are represented in **Figure 3.1a and d**.

3.2. Description of the Datasets used in the Study

In this study, we intend to focus on the Sentinel-1 (S1) mission of European Space Agency (ESA) for assessing its ability to study glacier dynamics in the IHR. S1 mission was developed by ESA under the Copernicus Initiative of European Union (EU), a conventional programme for global Earth Observation with modern satellite infrastructure. Under the EU initiative, 7 separate space missions are being developed, **1) Sentinel-1** mission is a radar imaging mission for land and ocean observation, 2) **Sentinel-2** is a multispectral high resolution optical imaging mission for monitoring land services with ability to extend emergency operations, 3) **Sentinel-3** is a multi-instrument mission to specifically work with sea-surface topography and interactions and global land monitoring services, 4) **Sentinel-4** will be a payload on a third generation Meteosat (MTG-S) satellite which is devoted to atmospheric monitoring from the geostationary orbit, 5) **Sentinel-5 Precursor** is a forerunner to Sentinel-5 mission for providing information on atmospheric trace gases, greenhouse gases and aerosols affecting earth's air quality, 6) **Sentinel-5** Mission will be for atmospheric monitoring from the polar orbit, and will be a payload to second generation Meteosat satellite and 7) **Sentinel-6** will host a radar altimeter for monitoring sea-level variations, with a focus on climatology and oceanography.

Table 3.1: Key characteristics of ESA's Sentinel-1a and -1b Satellites from S1 Mission

Specifications	Sentinel-1a (S1a)	Sentinel-1b (S1b)
Launch	03-Apr-14	22-Apr-16
Orbit	Sun Synchronous Orbit (693km)	
Sensor	C Band (5.6cms) – SAR Sensor	
Temporal Repeat Cycle	12 Days individually, 3-6 days (varies with region in consideration) when S1a and S1b are used in combination	
Acquisition modes	Strip-map (SM), Interferometric Wide Swath (IW), Extra Wide Swath (EW) and Wave mode (WV).	
Polarization	Single (HH or VV) or Dual Polarization (HH + HV or VV + VH).	
Data Format(s)	Level - 0 RAW	
	Level – 1 Single Look Complex (SLC)	
	Level – 1 Ground Range Detected (GRD)	
	Level – 2 Ocean (OCN) Product	

The S1 mission comprises of a constellation of 4 satellites with spaceborne SAR sensors aboard. Out of the 4 satellites, 2 have been launched by ESA. Their characteristics are briefly described in **Table 3.1**. The launch of the other 2 satellites as a part of this constellation is yet to be decided.

The primary mode of data acquisition by S1 SAR sensors in the IHR is Interferometric Wide Swath (IW). Images captured in this mode cover a swath equivalent to 250km on ground and have a spatial resolution of 5 x 20m. Level-1 IW SLC images are used for DInSAR processing to retrieve surface velocity. A total of 9 interferometric pairs with different temporal baselines acquired over different periods in Winter have been used for obtaining surface velocities of the 3 chosen glaciers. These images were captured between November 2016 and January 2018. We have used VV polarized information in all processes, due to its highly sensitive nature. **Table 3.2** presents an overview and key acquisition parameters of the datasets used for DInSAR processing.

For generation of topographic model for the study area, geometric correction of produced outputs and for elimination of topographic phase from generated interferograms, a SRTM DEM was used. Acquired in 2001 by NASA's Shuttle Radar Topography Mission, it has a resolution of 30m. This data is freely available from USGS's Earth Explorer Portal (https://earthexplorer.usgs.gov/).

Further, for obtaining classified glacier facies information 3 datasets from one year are required, each representing the winter, early summer and late summer conditions of the glacier. S1a has regular passes over the IHR in the descending node throughout the year, while passes of S1b are irregular and focussed to the winter period only. Therefore, products from the S1a platform were used for multi-temporal SAR classification. A total of 36 images acquired between December 2014 and December 2018 were used for producing 12 RGB composites for 3 glaciers, one each for 2015, 2016, 2017 and 2018. Level-1 GRD products, having a spatial resolution of 20 x 20m, were used for glacier facies classification. **Table 3.3** lists the set of products used for this process along with their dates of acquisition.

Table 3.2: Overview and key acquisition characteristics of datasets used for DInSAR processing. $B_\perp$ represents the perpendicular baseline and ΔT represents the temporal difference in the interferometric pairs.

| Glacier | Interferometric Pair | | | | $B_\perp$ | ΔT | Sub-swath | Satellite Node |
| | Master (T_0) | | Slave (T_1) | | | | | |
	Date	Platform	Date	Platform	meters	days		
Siachen Glacier	28-Nov-17	S1a	10-Dec-17	S1a	34.82	12	IW3	Descending
	10-Dec-17	S1a	16-Dec-17	S1b	113.9	6		
	21-Dec-16	S1b	27-Dec-16	S1a	39.71	6		
	21-Jan-18	S1b	27-Jan-18	S1a	87.7	6		
Bara Shigri Glacier	21-Dec-16	S1b	27-Dec-16	S1a	33.43	6	IW1 + IW2	Descending
	02-Jan-18	S1a	14-Jan-18	S1a	75.47	12		Ascending
	03-Jan-18	S1a	15-Jan-18	S1a	29.72	12		Descending
Gangotri Glacier	22-Dec-16	S1a	28-Dec-16	S1b	88.34	6	IW2	Descending
	15-Jan-17	S1a	21-Jan-17	S1b	106.59	6		

Table 3.3: List of datasets and their dates of acquisition used for classification of glacier facies. All datasets used for classification were acquired by Sentinel-1a SAR Sensor.

| Glacier | Year | Dataset used for classification | | |
		Winter	Early Summer	Late Summer
Siachen Glacier	2015	07-Jan-15	31-May-15	04-Sep-15
	2016	02-Jan-16	25-May-16	29-Aug-16
	2017	27-Dec-16	01-Jun-17	05-Sep-17
	2018	03-Jan-18	27-May-18	31-Aug-18
Bara Shigri Glacier	2015	07-Jan-15	25-Apr-15	23-Aug-15
	2016	03-Jan-16	01-May-16	29-Aug-16
	2017	08-Jan-17	08-May-17	05-Sep-17
	2018	03-Jan-18	21-Apr-18	31-Aug-18
Gangotri Glacier	2015	14-Jan-15	08-Arp-15	30-Aug-15
	2016	28-Dec-15	26-Apr-16	17-Sep-16
	2017	03-Jan-17	09-Apr-17	12-Sep-17
	2018	10-Jan-18	16-Apr-18	07-Sep-18

3.2.1. ERA Interim Climate Reanalysis Data

To relate and assess the findings in our study, precipitation and surface temperature data from the ECMWF ReAnalysis (ERA) - Interim Archive is used. ERA-Interim is a modern global level atmospheric reanalysis product of several climatic variables produced by the European Centre for Medium-range Weather Forecasting (ECMWF). Processed at a model resolution of T255 (approximately 80km on ground) over the horizontal scale and 60 levels over vertical scale, this data uses 4D-variational analysis and is available from 1979 to present day (Balsamo et al., 2015; Dee, Dick, & National Center for Atmospheric Research Staff, 2019). Key specifications of this product are presented in **Table 3.4**.

Table 3.4: Product specifications of ECMWF's ERA Interim

Specifications	ERA Interim	
Product	Atmospheric Reanalysis	
Produced by	European Centre for Medium-range Weather Forecasting (ECMWF)	
Temporal Availability	January 1979 – Present	
Temporal frequency	3-hourly, 12-hourly, daily and monthly average	
Model Resolution	Horizontal – 80km	
	Vertical – 60 Levels	
Input Data	In-situ and satellite observations	
Data Format(s)	netCDF and GRIB	

3.3. Summary

Siachen Glacier, Bara Shigri Glacier and Gangotri Glacier are glaciers from different locations in the Western Himalayan region, exposed to relatively variable climate regimes. Furthermore, the different sizes, hypsometry and physical characteristics of glaciers make them interesting components of this research. Datasets from the S1 mission, that have seen limited utility so far in the IHR, will be the primary focus for glacier velocity estimation and facies classification. Using these datasets, the proposed analysis is performed for the study area. The detailed methodology for achieving the proposed objectives is discussed in next chapter. The subsequent results obtained will be assessed using the ERA-Interim atmospheric data.

4. METHODOLOGY

This chapter summarizes the methods adopted in this study for retrieving glacier surface flow velocities and for classification of glacier radar facies using Sentinel-1 SAR products. While Differential SAR Interferometry (DInSAR) approach was used for velocity assessment, facies classification was performed using Multi-temporal SAR technique. In both the cases, the steps & factors for choosing ideal datasets are briefly presented. This is followed by some information on pre-processing of SAR datasets and accuracy assessment of the obtained results. Overview of the methodology followed in this research is pictorially presented in **Figure 4.1** *and* **Figure 4.5** *for retrieving velocities and performing classification, respectively.*
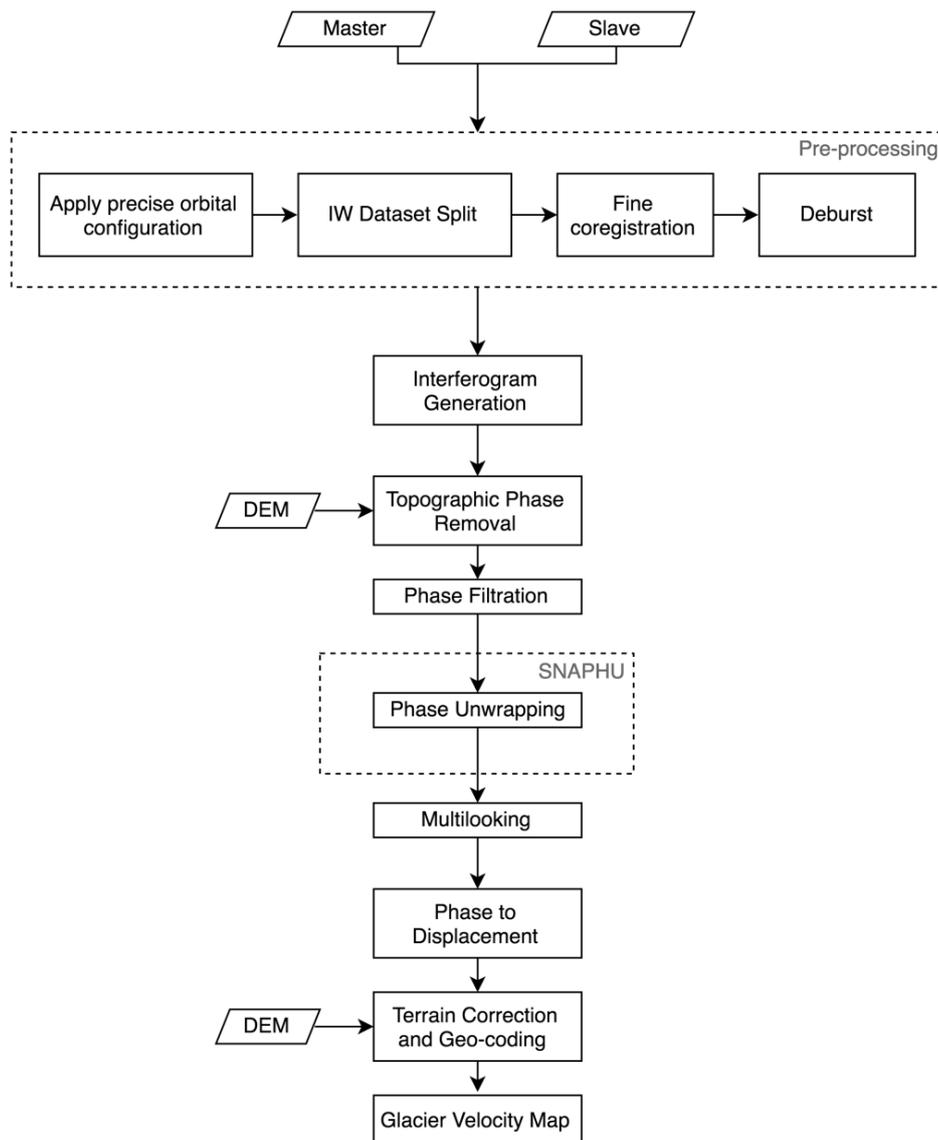
Figure 4.1: Methodological flowchart for surface velocity estimation using DInSAR

4.1. Differential SAR Interferometry for velocity estimation

DInSAR can be performed with help of either two repeat passes (1 interferometric pair) over the area of interest using an external DEM for elimination of topographic phase (Massonnet et al., 1993), or with three passes (2 interferometric pairs) where one pair is used for modelling topography, which is in turn used for eliminating topographic phase from the second interferometric pair (Zebker et al., 1994). In this study, we use a two pass DInSAR approach using an SRTM DEM (30m) for elimination of topographic phase.

All SAR processing for DInSAR is performed using ESA's Sentinel-1 toolbox (V 6.0). Final glacier velocity maps are prepared using ArcMap 10.3.

4.1.1. Selecting datasets for processing

Selection of datasets is the primary and a key step for interferometric processing, as this can have significant impact on the quality of results obtained. For estimating glacier displacement, following factors need to be considered while selecting datasets

1. **Glacier flow direction:** DInSAR estimates are most sensitive in LOS direction. If the glacier flow is perpendicular to the LOS direction of the satellite, the estimated velocity will be less sensitive. On the other hand, if the flow directions are in line with the LOS directions of the satellite, velocity estimates will be more reliable.
2. **Satellite heading – ascending / descending nodes:** Foreshortening is a manifestation of side-looking geometry of SAR. Foreshortening in study area can be avoided by selecting datasets from a suitable pass/node, also keeping in mind the glacier flow direction. Datasets from both passes may be required when estimating 2D/3D velocity.
3. **Period of the year – summer / winter:** Based on the previous knowledge of glacier flow rates and based on research interests, a suitable assessment period may be chosen. It may be important to note that during summer flow velocities and surface melting are generally higher than winter, with a potential to cause decorrelation in most of the cases.
4. **Spatial & Temporal baseline:** This is one of the vital factors while choosing datasets for interferometric processing. Spatial baselines less than the critical baselines are required, which otherwise causes complete spatial decorrelation of phase. Optimal baselines for DEM generation using tandem ERS-1/2 C-band products are between 150-300m (Ferretti et al., 2007), but for deformation/displacement as in our case, lower spatial baselines are preferred which could also be near-zero. This is also the case for temporal baselines, shortest temporally separated pairs are most preferred. Longer temporal baselines can cause temporal decorrelation. Therefore, optimal spatiotemporal baselines are vital.
5. **Weather conditions:** Poor weather conditions with a potential to cause atmospheric phase delay could propagate error while estimating glacier velocities. In case of an event of heavy storm, precipitation - rainfall or snowfall, loss of coherence will be significant. Such conditions should be cautiously identified and carefully assessed before selecting interferometric pairs.

Once the interferometric pair is chosen considering the factors mentioned, the first image (T_0) is labelled as master (reference image) and the second image (T_1) is labelled as the slave. This is used for generation of interferogram, coherence estimation and finally velocity mapping.

4.1.2. Pre-processing

Interferometric wide swath single look complex (IW-SLC) products of Sentinel-1 consists of 3 sub-swaths which in turn are a mosaic of multiple bursts. These products need to be pre-processed before being used for generation of interferogram for DInSAR processing. Pre-processing (presented in **Figure 4.1**) consists of applying precise orbital information, splitting the product to retain only the required sub-swath, fine sub-pixel level coregistration and data deburst. Although Sentinel-1 products are provided with associated orbital information in the metadata, precise orbital configuration for each of the datasets is separately available from ESA. Updating this information can help in accurate coregistration of the interferometric pair, which is vital to be achieved in DInSAR processing. Once the orbital configuration of the dataset is updated, the dataset can be split to retain only the sub-swath consisting the area of interest. The respective sub-swaths from the master and slave are precisely coregistered. Enhanced spectral diversity (ESD) can be used for improving the accuracy of coregistration. The coregistered product is subjected to deburst to eliminate the gaps between adjacent bursts in the image. This product is used for interferometric processing.

4.1.3. Differential InSAR Processing

The methodological flowchart for Differential interferometric processing is presented in **Figure 4.1**. Precisely coregistered interferometric pair is used for coherence estimation and generation of an interferogram. Coherence is a measure of similarity (correlation) of the pixel in the slave image with respect to the master reference image, based on a small window function. Its value ranges from 0 for areas with least coherence (only phase noise present) to 1 for areas with highest degree of coherence (complete absence of phase noise). A coherence map from scenes captured over Siachen Glacier is presented in **Figure 4.2**. It can be seen that over the glacier surface, substantial decorrelation is observed due to a longer temporal
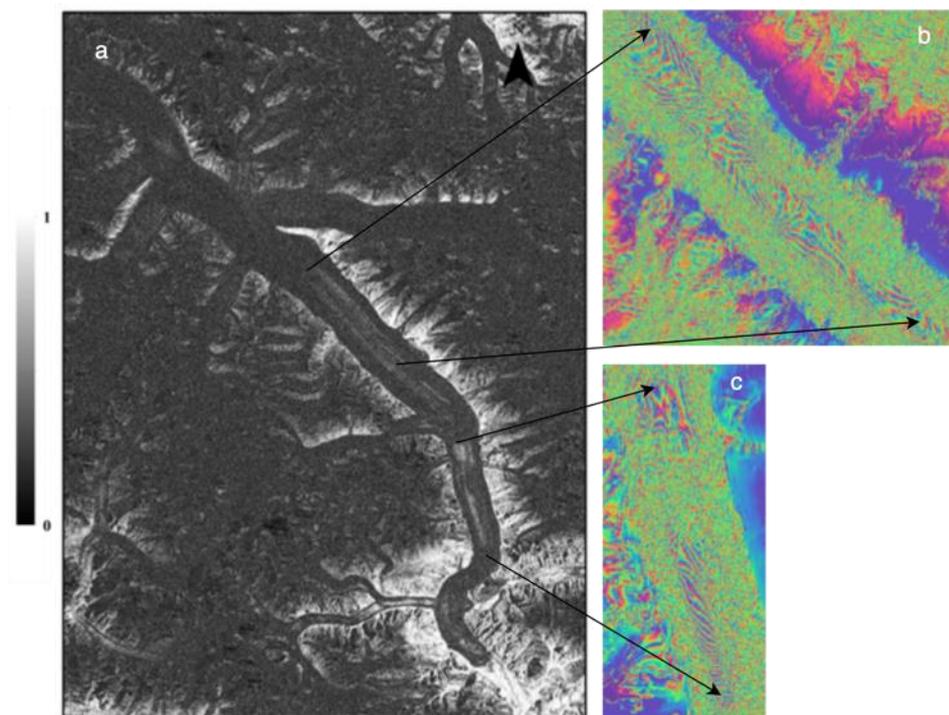
Figure 4.2: Illustration of coherence and its effect on the interferometric phase. a) Coherence map of Siachen Glacier produced using 12-day temporally separated pair (28Nov2016-10Dec2016). b) & c) display the formation of fringes in regions with some degree of coherence (>0.35), and complete noise where coherence is poor (<0.35).

baseline (Figure 8a). Where certain correlation is present, fringes in the interferogram are clearly seen, while much of the remaining region is dominated by phase noise. Therefore, assessment of coherence between the selected interferometric pair is important before generation of an interferogram.

Interferogram, which is a measure of phase difference, is calculated using phase information from the master and slave. This generally consists of topographic phase, phase due to displacement, earth's curvature, atmospheric conditions and noise (eq. 2.1). While atmospheric phase delay is assumed to be negligible, phase due to earth's curvature is eliminated. The resulting interferogram consists of phase contributions from topography and displacements, given by (eq. 4.1)

$$\Delta \varphi = - \frac{4\pi}{\lambda} \frac{B_\perp h}{R_1 \, Sin\theta} + \frac{4\pi}{\lambda} d + \Delta \varphi_{noise} \qquad (4.1)$$

Quantification of $\Delta \varphi_{noise}$ is extremely complicated. A well-justified assumption can be used, taking into consideration all the error sources that contribute to $\Delta \varphi_{noise}$. This is explained in **section 4.1.5**. An external SRTM DEM is used to synthetically generate topographic phase model and eliminate the same, resulting in a differential interferogram which retains only phase contribution from displacement of ground objects. This phase is filtered using Goldstein phase filtering approach.

Unwrapping of the wrapped phase is executed using SNAPHU (Chen & Zebker, 2002) on a high processing cluster (HPC). The unwrapped phase (φ_{uw}) is then converted to LOS displacement (V_{los}) using 'phase to displacement' function, that is given by (eq. 4.2)

$$V_{los} = - \varphi_{uw} \frac{\lambda}{4\pi} \qquad (4.2)$$

Displacement in LOS direction (V_{los}) is further decomposed to surface velocity in glacier flow direction (V_{glac}) using equation (eq. 2.2) given by Kwok & Fahnestock (1996) and Wangensteen et al. (2005). The velocity estimates, in the order of meters representing relative motion between the master and slave (separated by ΔT which is the temporal baseline), are up-scaled to present average annual velocities as meters per year (m/y), with an underlying assumption that glacier movement is linear throughout the year. This calculation is performed using the given function

$$V_{glac}(m/y) = \frac{V_{glac}}{\Delta T} \, 365 \qquad (4.3)$$

The final glacier surface velocity maps in m/y are presented and discussed in the chapters 5 and 6.

4.1.4. Validation of velocity estimates

Practically, validation of estimated velocity should be done using field measured information. However, in our case, due to lack of field measured data for the chosen study area validation of the estimated velocity has been done using proxy information. Proxy information includes estimates published in journal publications, scientific articles and reports for specific glaciers. Ideally, it is best to validate estimates of glacier surface velocity using field measured data only, generally collected over a period of time using stakes and DGPS coordinates over a network of points spread across the glacier surface.

4.1.5. Uncertainty Analysis & Error Propagation

There are several errors that propagate through the estimation process and contribute to uncertainties in surface displacements. Collectively referred to as *phase noise* ($\Delta\varphi_{noise}$), this is a measure of phase delay due to atmospheric conditions, orbital inaccuracies, decorrelation and unmodelled deformation. We have categorized all the error sources either as acquisition errors (Δacq) or as processing errors (Δproc), which totally amount to $\Delta\varphi_{noise}$, given as

$$\Delta\varphi_{noise} = \Delta acq + \Delta proc \tag{4.4}$$

Imaging characteristics of the sensor and prevailing atmospheric and surface conditions during acquisition of master and slave images may account for errors due to geometric and temporal decorrelation, atmospheric heterogeneity, orbital inaccuracies, thermal and quantization noise. As these are a manifestation of acquisition geometry, we refer to them as *acquisition errors* (Δacq). While errors that arise due to various processing steps, viz. coregistration, partial phase elimination, phase unwrapping, phase filtration and multilooking, are collectively referred to as *processing errors* (Δproc). The steps and associated errors are pictorially represented in **Figure 4.3**.
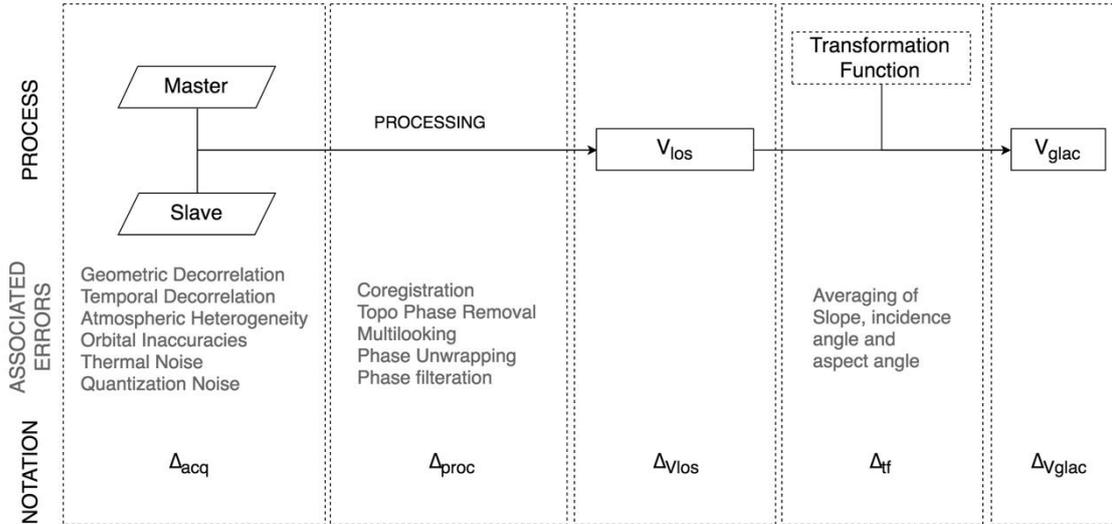
Figure 4.3: Description of various errors associated with the process of velocity estimation and their respective notations.

As independent quantization of these factors will be complicated, we assume a constant value of **5mm/epoch** as $\Delta\varphi_{noise}$ for Sentinel-1a and 1b products.

Another error contribution to the entire process is during transformation of LOS-Velocity (V_{los}) to Velocity in glacier flow direction (V_{glac}), where slope (α), incidence angle (θ) and aspect angle with respect to radar direction (ξ) are the transformation parameters. As average values are used, variance of these components (pixel by pixel) is used to represent transformation error (Δtf). Therefore, the error associated with final velocity estimates (QV_{glac}) is calculated using the law of error propagation. A general notation is given by

$$Q_{V_{glac}} = (A^T Q_{V_{los}}^{-1} A)^{-1} \tag{4.5}$$

Where QV_{glac} is the error associated with V_{glac}, QV_{los} is the error associated with V_{los} and A is the transformation function, given by ($\cos\alpha \cos\xi \sin\theta + \cos\theta \sin\alpha$) in our case.

4.1.6. Sensitivity Analysis

Sensitivity analysis is performed using a approach similar to the one presented by Chang, Dollevoet, & Hanssen (2018). This also forms an important component that contributes to error presented in the previous section.

Sensitivity of movement is determined using the *slope (α)*, *direction of movement with respect to radar beam direction (ξ)* and the *the incidence angle (θ)*. The *direction of movement with respect to radar beam direction ($\xi = \zeta - \beta$)* is given as the difference between radar beam direction and direction of glacier movement (β). Using these components, sensitivity may be derived using the following function

$$s = |V_{glac} \left(cos\alpha \; cos\xi \; sin\theta + \; cos\theta \; sin\alpha \right)| \tag{4.6}$$

Scalar sensitivity metric (notated as s), ranges between 0 and 1 ($s \in [0, 1]$), 0 indicating least sensitivity and 1 indicating highest sensitivity. This metric may be crucial to assess if deformation in a particular direction having a specific slope is observable using the given satellite, or not. As this metric is particular to a beam direction of the radar sensor, the degree of sensitivity of deformations will vary when estimated using satellites with a different viewing geometry.

LOS Velocities, that are estimated using 1 interferometric pair, are most sensitive in the beam direction (ζ) of the satellite sensor in consideration ($\xi = 0°/180°$, implying parallel movement). Whereas, those movements perpendicular to the beam direction are least sensitive ($\xi = 90°/270°$, implying perpendicular movement).

For easier understanding, in Error! Reference source not found. we present a sample sensitivity curve assuming a satellite having a beam direction $\zeta = 90°$ (satellite heading direction $= 0°$) and surface slope $= 0°$. Direction of deformation (β) is presented along the circumference of the circle. Colours along a specific direction indicate the degree of sensitivity in which the satellite could observe corresponding movement. Since sensitivity values for deformation in a particular direction are line-symmetric for a complete cycle $\beta \in [-180°, 180°]$, we plot sensitivity curve only in the range $\beta \in [0°, 180°]$.
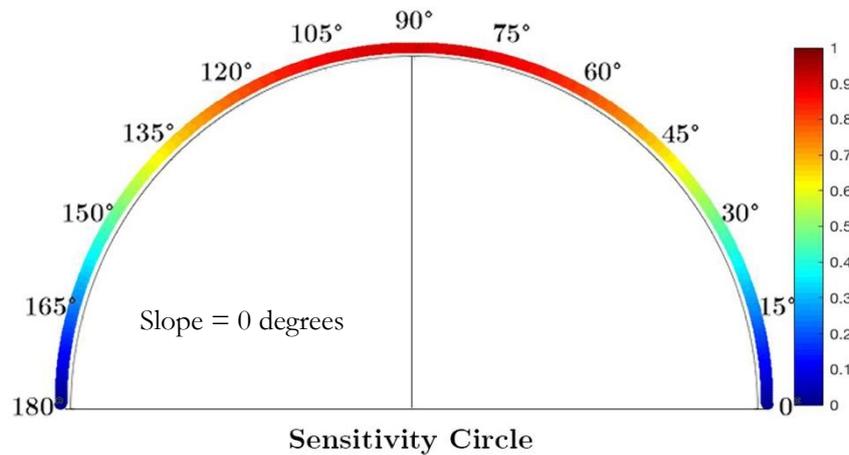
Figure 4.4: Sensitivity Circle representing the degree of sensitivity for movement in a particular direction (β) with respect to radar beam direction ($\zeta = 90°$). The basal slope considered is $\alpha = 0°$.

As lower sensitivity can potentially enhance uncertainty of the estimate, the associated error of a particular velocity vector (QV_{glac}) should be divided by the sensitivity value. This error is used to present uncertainty associated with estimated velocities.

4.2. Multi-temporal SAR for classification of glacier radar facies
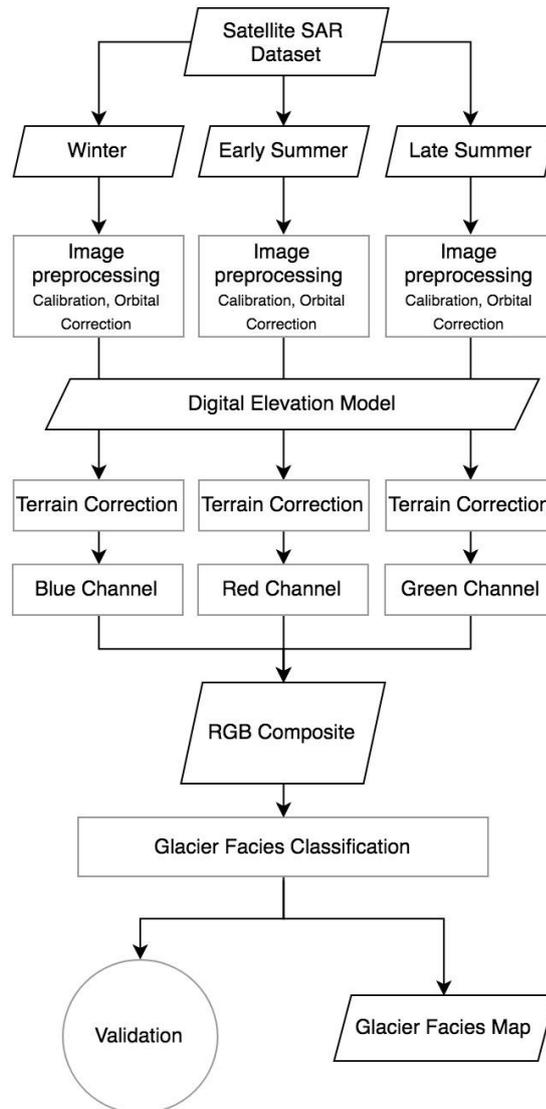
Figure 4.5: Methodological flowchart for Multi-temporal Classification of Glacier Facies

Multi-temporal SAR approach uses characteristic temporal signatures of different radar zones for classification. This mandates the requirement of multiple images from different seasons for identification and classification of glacier facies. 3 images, one each from winter, early summer and late summer are used to form a RGB composite. This is used as an input to the classifier, for classification. The overall methodology for classification based on Multi-temporal SAR approach is presented in **Figure 4.5**. The pre-processing and processing of SAR datasets is done using ESA's Sentinel-1 toolbox (V 6.0). Classification and validation of outputs is performed in ENVI (V 5.0) and using R Programming.

4.2.1. Choosing datasets

1. **Climate regimes:** Glaciers in different regions of the Himalayas are exposed to different climate regimes. Those in the far Western Himalayan range are greatly influenced by westerlies (Bookhagen & Burbank, 2010)in addition to minor influence from the summer monsoon. These regions are also

colder (Shekhar, Chand, Kumar, Srinivasan, & Ganju, 2010), due to which the onset of melting (early summer) is later than the onset in the Central Himalayan or the Eastern Himalayan range. As this study includes glaciers from both the Himalayan ranges, careful attention needs to be paid to choosing of datasets, specifically for the case of Early summer.

2. **Non-Seasonal precipitation events:** Non-seasonal events of precipitation are frequent in the higher altitudes. If an image in summer was captured just after an event of precipitation, the backscatter properties change substantially leading to errors in classification. Occurrence of such events can be checked using meteorological information or optical datasets.

Although selecting datasets for Multi-temporal SAR classification is relatively easier, careful attention should be paid during selection process. These datasets are further pre-processed before using them for classification.

4.2.2. Pre-processing

The first step towards usage of multiple SAR images is to calibrate the backscatter intensity to represent and compare the actual ground information. After calibration, orbital information associated with the datasets should be upgraded to ensure precise coregistration of the three images. Post coregistration, the stacked product is terrain corrected using an external DEM. This geometrically-corrected stacked 3-image-composite is used for classification.

4.2.3. Classification of Glacier Facies

With help of the composite image, a RGB composite is prepared to visualize the different radar facies. While winter image is passed through blue band, early summer and late summer images are passed through red and green bands respectively (Partington, 1998). Based on the temporal backscattering properties, different colours of the glacier surface on the RGB composite represent different glacier facies, as described in **Section 2.5**. Different classifiers can be used for automated classification. In this study, Support Vector Machine (Camps-Valls et al., 2004) is used for classification because of its efficiency, robustness, sensitivity and computational performance. A supervised approach is adopted by providing a sample set of training points to be used for training the classifier. The ROI polygons are created using previously classified glacier facies map (from Bisht, (2015)), temporal backscatter characteristics and VHR optical datasets as reference and sample set was generated. The number of samples used are listed in **Appendix 1**. Of all the sample in the sample set, around 70% were used for training the classifier and the rest was used for testing. Once the classifier is trained, classification of the 3 image composite is performed.

Apart from Support Vector Machines, other modern classifiers may also be used for classification of glacier facies. Brief description of SVM classifier is given in the following sub-section.

4.2.3.1. Support Vector Machines

Support Vector Machine (SVM), a machine learning algorithm, has emerged to become a superior tool commonly used for classification of multi-dimensional remote sensing products. Its applicability has been highlighted due to its efficiency and robust nature, presenting exceptionally good accuracies in most of the cases (C. Huang, Davis, & Townshend, 2002; Tso & Mather, 2009). Initially designed as a binary classifier, SVM is now widely used for classification of multi-dimensional data into several number of classes. By constructing an optimal hyperplane, with maximum margin (as shown in **Figure 4.6**), this classifier tries to
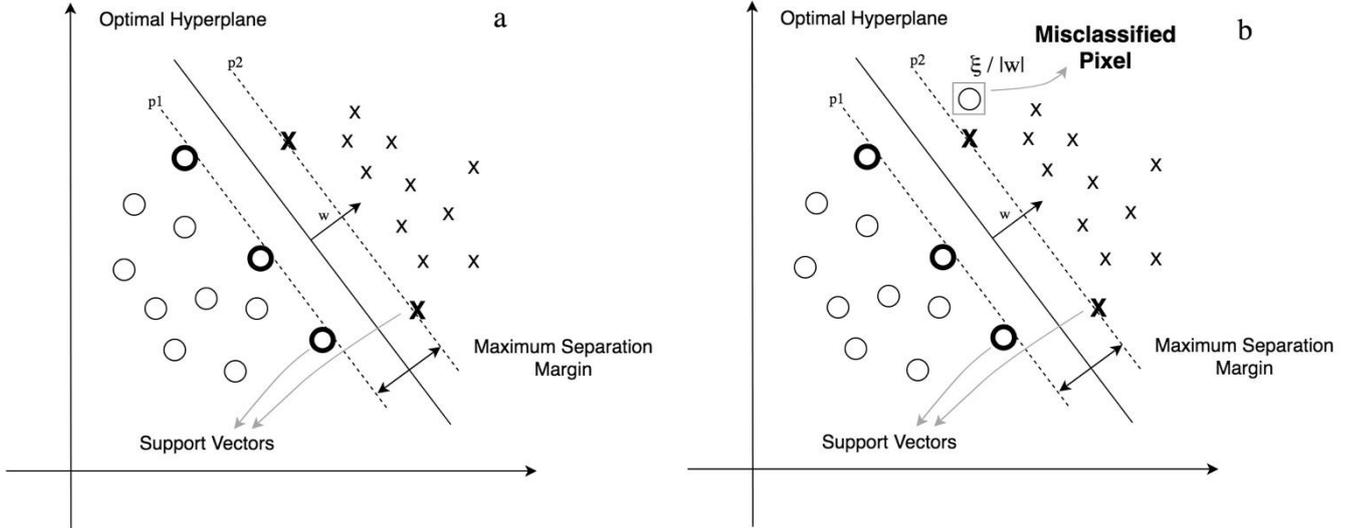
Figure 4.6: Illustration of Support Vectors and a liner hyperplane for a separable case (a) and non-separable case (b). In (b) a misclassified pixel is highlighted and shown.

separate the training pixels in consideration effectively. The location and the margin of the hyperplane is very sensitive to the provided training set, making this one of the most important components of SVM classification. The training set is represented by $\{x_i, y_i\}$; $i = 1, \ldots, n$; $x_i \in R^d$ where x_i is the spectral information and y_i the information class to which the point belongs. A hyperplane is represented by the following decision function

$$w^T x + b = 0 \tag{4.7}$$

where x is a point on the hyperplane, w is perpendicular to hyperplane, T represents matrix transposition and b represents bias. Two linear planes (p1 and p2, as shown in **Figure 4.6a**) that form margin boundaries may be constructed if the training set satisfies the following 2 equations,

$$w^T x_i + b \geq +1, for\ y_i = +1 \tag{4.8}$$

$$w^T x_i + b \leq -1, for\ y_i = -1 \tag{4.9}$$

which can be combined to give

$$y_i(w^T \times x_i + b) - 1 \geq 0 \tag{4.10}$$

These separating hyperplanes are generated only using a subset of the training set, called the Support Vectors. When the conditions given by eq. 4.10 cannot be satisfied by the training data, slack variables ξ_i, i = 1,…., n, are introduced which are proportional to the cost parameter (explained later in this section). This helps in relaxation of the constraints enforced by eq. 4.10. by permitting certain cases of disagreement. After inclusion of slack variables, eq. 4.10. becomes

$$y_i(w^T \times x_i + b) \geq 1 - \xi_i\ ;\ \xi_i \geq 0, \forall i \tag{4.11}$$

This represents the linear non-separable case (**Figure 4.6b**), where a few misclassified pixels are allowed. Based on the complexity of training data provided, a linear separable hyperplane, linear non-separable hyperplane or non-linear hyperplane may be constructed using the various construction parameters. In non-

linear case, the raw data is transformed into a higher dimensional Euclidean space that helps in wider separation of the training pixels (Boser, Guyon, & Vapnik, 1992). Use of kernel functions was proposed by Vapnik (1995) to reduce the computation burden due to processing of such complex data.

Different kernel functions such as the Linear kernel, Radial Basis function, Gaussian Radial Basis function and Sigmoid are available. These are mathematical functions that help in projecting data into multi-dimensional planes to improve separation and classification accuracy. The classifier is also very sensitive to input parameters such as C (soft margin cost function/penalty) and γ (gamma), which should be carefully defined to ensure optimal classification outputs. The range of cost function, C varies from $-\infty$ to $+\infty$, while that of γ varies from -1 to +1. C controls the selection and influence of support vectors, and the degree of misclassification that is permissible and γ influences the sensitivity (degree of softness or non-linearity) of hyperplane formation that helps in separation of training data. Repeated attempts with varying C and γ (trial and error method) helps in defining these parameters based on the accuracy of the classified output.

We, for glacier facies classification using SVM, used a radial basis kernel function. An R program, which iterates multiple times with variable C & γ values, to fine tune the parameters was used to find optimal values to be used for classification.

4.2.4. Accuracy assessment

To ensure the credibility of the classifier, accuracy assessment is performed. The quality of classification should ideally be assessed using field collected points representing different radar facies on glacier surface. Point by point comparison of the information class collected from the field with that extracted from the classified output image gives an estimate of the accuracy of the classification. However, due to non-availability of field information for this study, a test set is parallely generated using similar procedure used for generation of a training set, as described in sub-section 4.2.3. Using information from this exercise, overall accuracy (OA) was calculated from the confusion matrix along with user's (UA) and producer's accuracy (PA).

4.2.5. Equilibrium line altitude and evolution trend

Separating the accumulation zone and the ablation zone, the Equilibrium line altitude (ELA) is generally considered the boundary between the superimposed ice facies and the bare ice facies. This can be manually delineated and marked using GIS tools. The processes should be performed very cautiously using both the classified output and the RGB composite. Performing classification on multiyear datasets can help in comparing the variations in glacier responses year on year. This way the fluctuation of ELA can also be assessed and analysed to obtain an idea on the evolution trends of the glacier.

5.   RESULTS AND ANALYSIS

This chapter presents the results obtained by following the methodological framework presented in **Chapter 4**. *Additionally, an analysis of the results is also described and presented in this chapter. The chapter is organized in different sections starting with glacier surface velocity estimation for all the glaciers chosen as the study area, followed by glacier facies classification and ELA determination.*

5.1.   Glacier Surface Velocity Estimation

For the 3 chosen glaciers in the study area, namely Siachen Glacier, Bara Shigri Glacier and Gangotri Glacier, surface velocities in glacier flow direction were estimated in 2 steps, as described in section 4.1. First the LOS velocity was estimated using the DInSAR approach followed by estimation of the actual surface flow velocity in the glacier flow direction using a transformation function (Eldhuset et al., 2003; Wangensteen et al., 2005). Prior to estimation of LOS velocity, the coherence between the interferometric pairs was estimated and analysed before using the phase information to estimate displacement.

5.1.1.   Estimation of Line of Sight (LOS) Velocity

Considering the selection parameters detailed in section 4.1.1, optimal interferometric pairs were chosen and used for estimating degree of coherence. Where available more than one interferometric pair was selected, so the one with the highest degree of coherence over the entire area of the glacier could be used for DInSAR processing. **Figure 5.1** presents the coherence bands estimated using the chosen interferometric pairs – 21 & 27 December 2016 for Siachen and Bara Shigri Glaciers and 22 & 28 December 2016 for Gangotri Glacier. The key characteristics of these pairs are listed in **Table 3.2**. It can be clearly observed in the coherence images that there is relatively fair degree of coherence over the main glacier surface, although poor coherence is seen over non-glaciated regions and higher reaches of the glacier. To ensure higher coherence in these areas of the glacier, pairs with lower temporal baseline are required, which are not available from the dataset in consideration – S1a/b. However, good degree of coherence on the main glacier tongue of all three glaciers permits usage of these pairs for InSAR/DInSAR processing. In case

Figure 5.1: Coherence bands for Siachen Glacier(a), Bara Shigri Glacier (b) and Gangotri Glacier(c) estimated using the chosen interferometric pairs.

of Bara Shigri Glacier and Gangotri Glacier, much of the coherence retained is over the debris covered part, while the bare ice region and accumulation region possess low coherence. It should be understood that the estimates of deformation/displacement will be reliable only in the areas where coherence is optimal (generally >0.35), permitting formation of interferometric fringes. An example of a low coherence image from Siachen Glacier and its consequence on formation of fringes is presented in **Figure 4.2**.

The same set of interferometric pairs were used for further interferometric processing. Differential interferograms for each of these pairs were generated using the two-pass DInSAR approach and an external SRTM-DEM for elimination of topographic phase. Considering the computational intensity of phase unwrapping using SNAPHU, only a subset containing the region of interest from the entire product was processed. The LOS velocities estimated by this process are presented in **Figure 5.2**.

LOS velocities are one dimensional estimates of glacier movement in the slant-range direction. While movement towards the satellite is shown on a positive scale, the movement away from the satellite is shown on a negative scale.
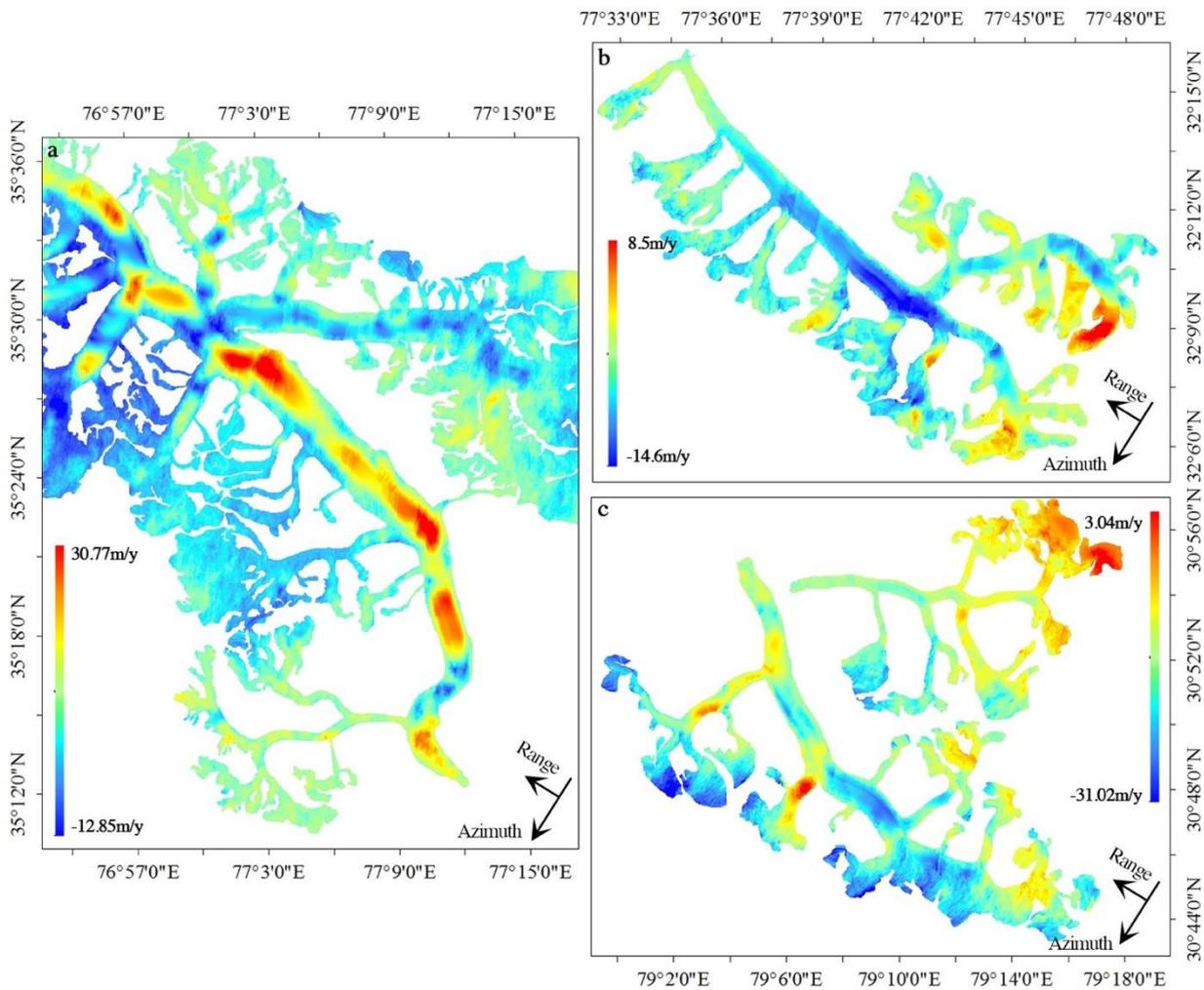
Figure 5.2: Line-of-sight velocities generated using S1a/b interferometric pairs for Siachen Glacier (a), Bara Shigri Glacier (b) and Gangotri Glacier (c). At the lower right corner of the image is azimuth (descending pass) and slant-range (right-looking) direction of the corresponding satellite, guiding the LOS direction.

In case of Siachen Glacier (**Figure 5.2**a), displacement is estimated to range between -12.85m/y to 30.77m/y. Highest positive values are seen along the main trunk of the glacier. Where there is a change in direction of the flow path, the velocity reduces while speeding up again after changing the direction. On the higher reaches of the glacier, in the accumulation zone, the velocities are lower. It may also be noted that the direction of flow of Siachen Glacier is in the south-east direction, i.e. towards the satellite sensor, while that of Bara Shigri (**Figure 5.2**b) and Gangotri (**Figure 5.2**c) glaciers is in the north-west direction, away from the satellite sensor. Therefore, the velocities on the main trunks of Bara Shigri and Gangotri glacier appear in negative range, indicating their movement away from the satellite sensor. In case of Bara Shigri glacier, 4 tributaries come together to form the main trunk of the glacier. The mass contributed by the 4 tributaries accelerates the flow at the junction, and this region is seen to have the highest rate of displacement. The range of estimated velocity over Bara Shigri glacier is between -14.6m/y to 8.5m/y and over Gangotri glacier it is between -31.02m/y and 3.04m/yr. Like Bara Shigri glacier, the orientation of Gangotri glacier is also in the north-west direction, therefore the negative values indicate movement in the glacier flow direction and away from the satellite sensor. Velocities over Gangotri glacier are variable with relatively higher rates of displacement along the main trunk.

5.1.2. Surface Velocity in Glacier Flow Direction

Although one can get an idea of the glacier flow rates using LOS velocity, the measure is of least significance to understand the actual magnitude and direction of the flow. We have projected LOS velocities in glacier flow direction using the transformation function presented by Eldhuset et al. (2003) and Wangensteen et al. (2005), given in **equation 2.2**. Using slope, aspect angle with respect to radar direction and incidence angle for each of the glaciers, actual velocity in the glacier flow direction is estimated. However, it should be noted that, this works only for areas that are more or less in the LOS direction. If the movement is perpendicular to LOS of the satellite sensor, the transformation function cannot produce reliable estimates (Cheng & Xu, 2006; Mattar et al., 1998). The results of estimated surface velocity in glacier flow direction are presented in **Figure 5.3** for Siachen (a), Bara Shigri (b) and Gangotri (c) glaciers.

Siachen Glacier is a large and a complex glacier with several tributaries contributing mass to its main trunk. While movement of the glacier is primarily in LOS direction, the direction of movement of its tributaries is far from being closer to the LOS. The velocity over this glacier rises to a maximum of 135.27±5.1 m/y at the junction of tributaries (shown as 'p' in **Figure 5.3a**). The flow rate continue to be higher, between ~60m/y to ~100m/y, along the main trunk ('p' ➔ 'q') before further increase due to influx of mass from 2 more tributaries at 'q'. But, the deviation in flow path at 'q' leads to reduction in the rate of displacement. Along 'r', where there is a major deviation in the flow path, significant attenuation is caused to the ice velocity lowering the flow to mere ~5m/y – ~20m/y. Reduced basal friction due to higher temperature and meltwater and mass influx near the snout increases the velocity at the glacier terminus. Unlike the flow patterns in the ablation zone, the velocities observed in the higher reaches of the glacier are significantly low. Reduced driving stress due to low accumulation mass and colder temperature regimes contribute to lower velocities in the higher reaches.

Bara Shigri Glacier, with a length of 27.2km, is composed of several small tributaries in addition to one large tributary meeting the main glacier trunk at 'u' from the right. At this point of confluence there is a huge influx of mass, causing the velocity to be around ~27m/y – ~32m/y (**Figure 5.3b**). Further along the flow path, the velocity gradually reduces to 20±3m/y due to reduced driving stress and basal attenuation. Where a major tributary joins the main glacier trunk, velocity increases and further decreases. At point 'v' over the right arm of the glacier and 'w' along the upper part of the main trunk, patches of higher displacement can

be seen, which are due to higher degree of slope. Furthermore, lower rates of displacements in the higher reaches are explained by decreased driving force from snow mass.

Gangotri Glacier is also a complex system composed of several tributary glaciers, namely Kirti (K), Ghanohim (G), Swachhand (S) and Mainadi (M). Chaturangi Glacier (Ch) which was once a part of the system has retreated to become a separate glacier. With a length of 29km, this glacier has variable velocity along the lengths of the glacier surface as seen in **Figure 5.3c**. Rate of displacement along the main glacier trunk at 'S' is about 30.2±4.3m/y. Minor increase in velocity is seen after 'G' due to mass influx from Ghanohim glacier, a small tributary to Gangotri. At 'K' where there is influx of mass, there is also a minor deviation in flow path causing decrease and then increase in the flow velocities to 20±2.07m/y. At 'G' which is the point of confluence of Ghanohim with Gangotri Glacier, there is a steep downward slope which causes disintegration of ice and formation of large crevasses, therefore causing decorrelation in SAR coherence band, seen in **Figure 5.1c**. Thus, at this point where higher velocities are expected, velocity estimates are certainly incorrect and cannot be correctly estimated.
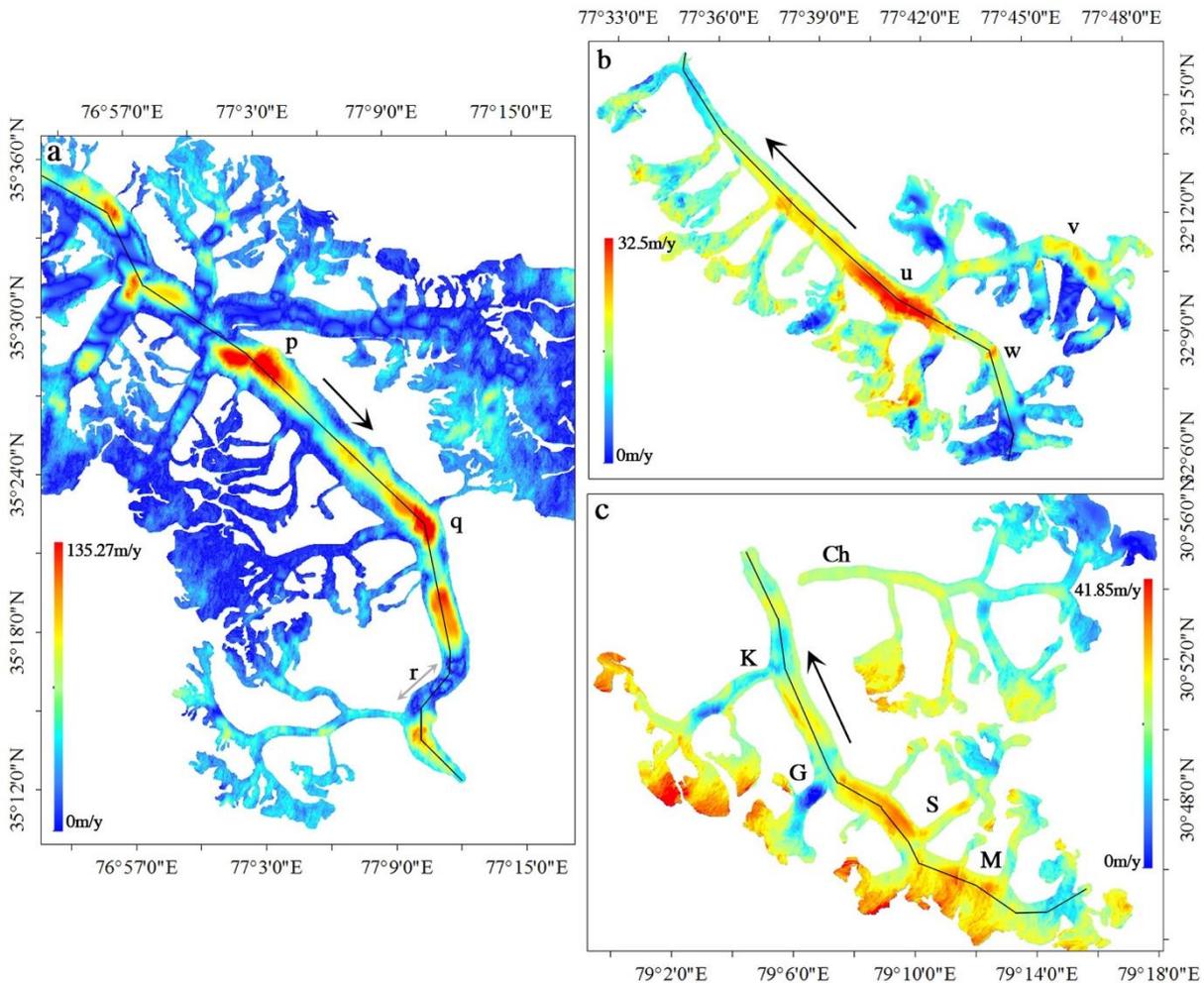
Figure 5.3: Surface velocities in direction of glacier flow estimated from DInSAR derived LOS Velocities for Siachen Glacier (a), Bara Shigri Glacier (b) and Gangotri Glacier (c). Direction of glacier flow is indicated by black arrows. In case of (a) and (b), alphabets are used for referring to explanation of analysis in the chapter. In (c), 'K', 'G', 'S', 'M' and 'Ch' are points of confluence of Kirti, Ghanohim, Swachhand, Mainadi and Chaturangi with Gangotri Glacier respectively. They are also used for referring to explanations in the chapter. Black line on the main glacier trunk is the glacier centreline.

From the results it is generally observed that glacier velocities are highest over the main trunk of the glacier. Basal slope and driving stress induced by mass influx from tributaries can potentially enhance the flow velocities. It is also noted that velocities are higher along the centrelines, due to possible attenuation from the edges. Deviations in the flow path of the glacier ice can also impact the flow velocities, where the extent of impact is proportional to the degree of deviation.

5.1.3.   Sensitivity Analysis
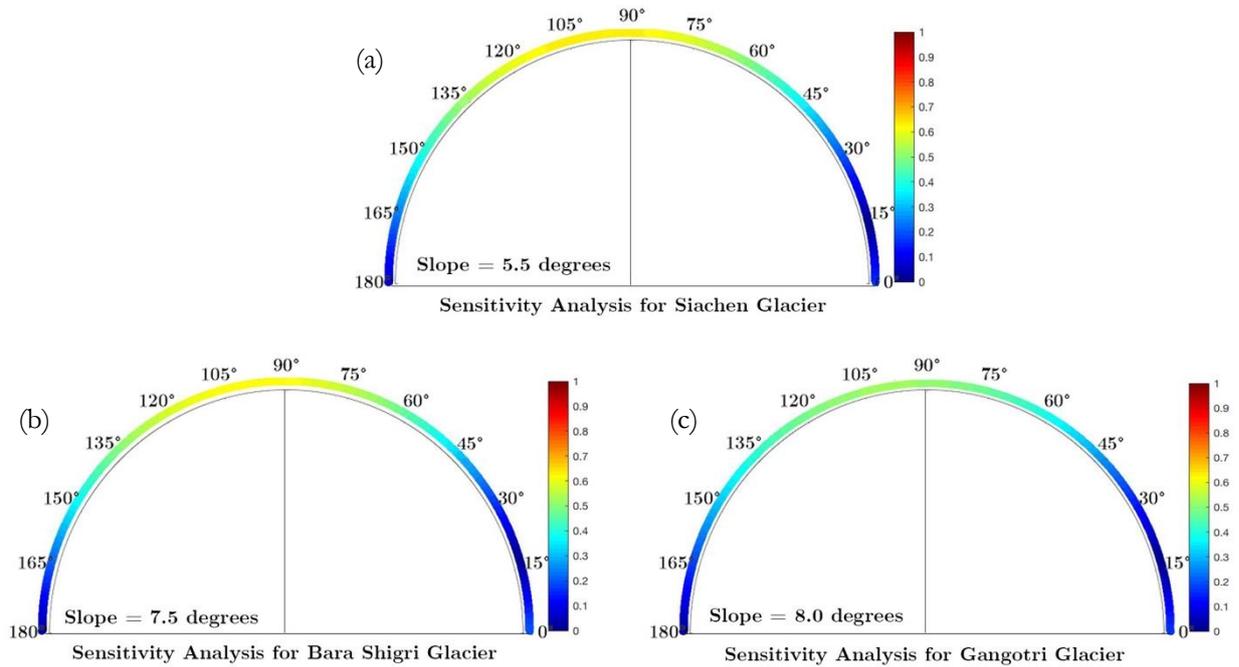
Figure 5.4: Sensitivity Map for Siachen (a), Bara Shigri (b) and Gangotri Glaciers(c). The radar beam direction is $\zeta = 280°$ for Sentinel-1a & -1b sensors. The average slope used for determining sensitivity is mentioned on the figure.

Based on the approach presented in **Section 4.1.6** of the previous chapter, we have determined sensitivity for different glaciers and presented them in form of sensitivity circles in **Figure 5.4**. The direction of glacier movement is along the circumference of the circle denoted by degrees in the image. It can be observed that Siachen Glacier had the highest sensitivity of 0.66 along the main glacier trunk, while for Bara Shigri and Gangotri Glaciers it was slightly lower at 0.61 and 0.55 respectively. Sensitivity values are used for accounting uncertainty associated with each velocity vector.

5.2.   Glacier Facies Classification

Classification of glacial facies using multi-temporal surficial characteristics was performed using S1a datasets and multi-temporal SAR approach. Visualizing calibrated scenes from early summer, late summer and winter through red, blue and green colour bands gives distinct colours to different facies, as described in

Table **5.1** and presented in **Figure 5.5**. These seasonal characteristics are central to classification of facies using this approach.
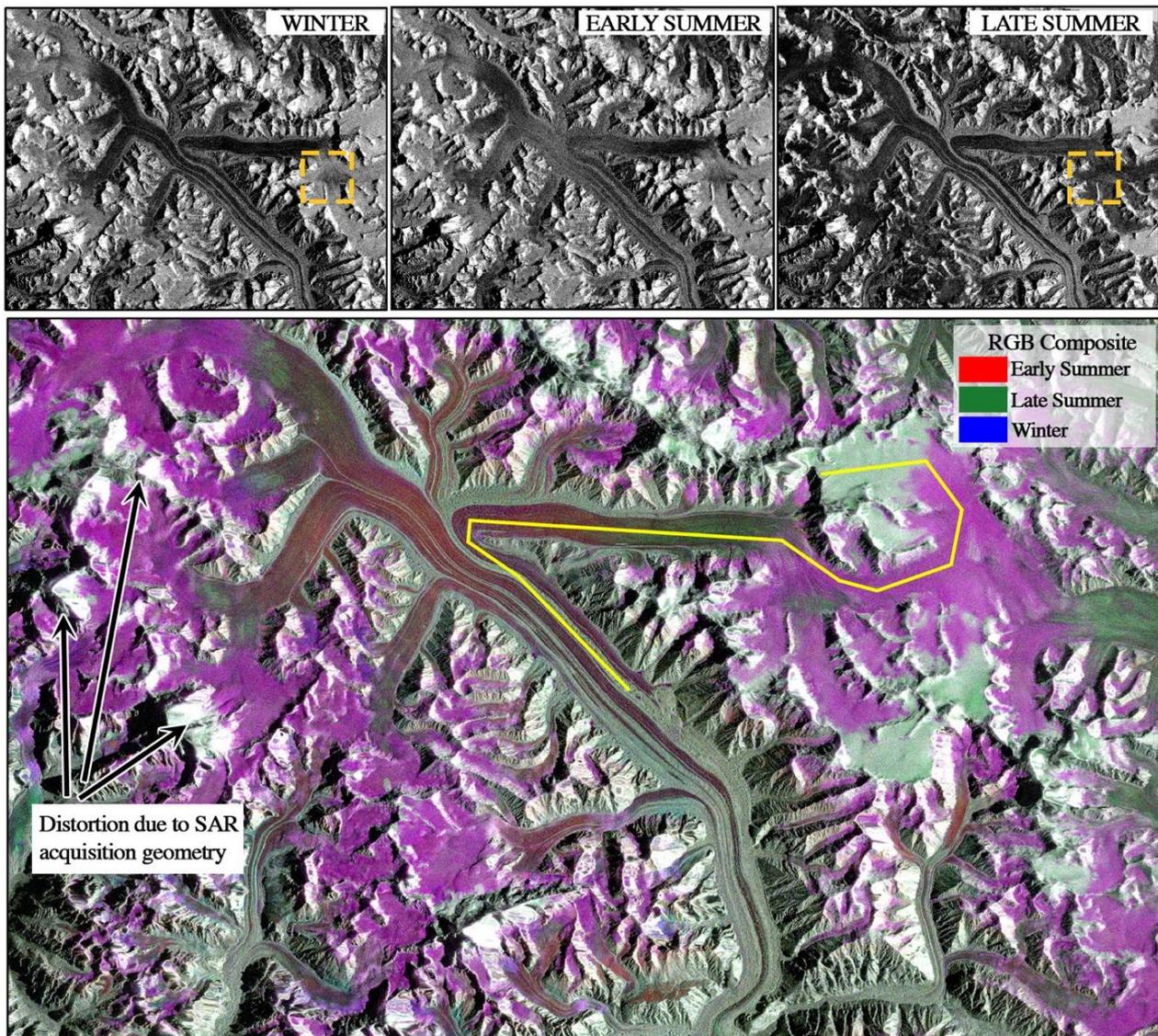
Figure 5.5: Top: SAR Backscatter intensity images of Winter, Early Summer and Late Summer. The dashed-box highlights an example of change in intensity over different seasons. Bottom: RGB Composite of SAR Backscatter Intensity. Intensity values along the yellow line are represented in **Figure 5.6**. Examples of distortion are indicated in the image.

5.2.1. Multi-temporal Signatures
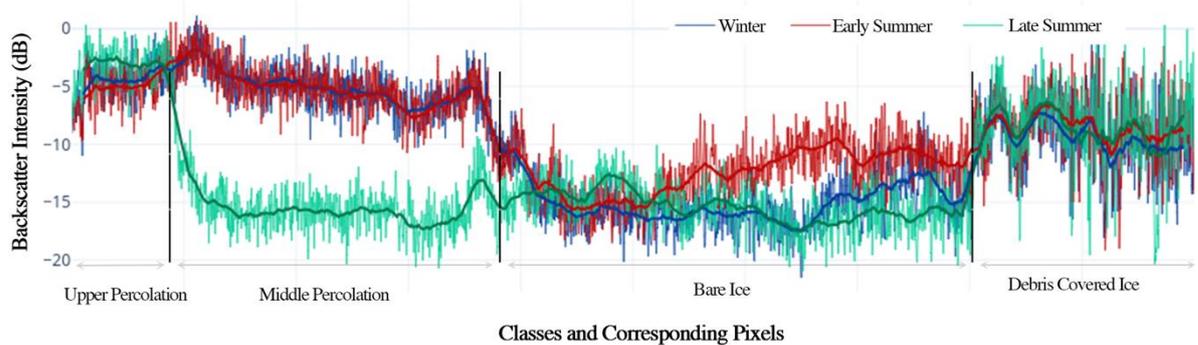
Figure 5.6: Backscatter Intensity profile drawn for pixels of different classes. The path is presented on the RGB Composite in **Figure 5.4**.

The Indian Himalayan Region (IHR) is characterized by compact dry snow in the higher reaches of the glacier due to extremely cold sub-zero temperature regimes. With a decreasing gradient of dryness along with decline in elevation, the scattering properties also change. Rise in temperature, along lower elevations, enhances melting rates of snow and firn causing a spatial variation of backscatter intensity. The C-Band backscatter intensity of compacted dry snow is high (-2.5 ± 2dB), while that of wet snow is lower (-6.2 ± 2.05dB) and very low for bare ice (-15 ± 2.25dB). Loosely packed dry snow, which is generally seen in dry snow facies having a very low backscatter intensity, is absent in the IHR. Debris cover has a highly variable scattering mechanism, as seen from **Figure 5.6**. As time proceeds from winter to early summer and late summer, temperatures gradually increase giving rise to temporal variations along different glaciated regions. Increase in meltwater content of snow/ice pack, exposure of underlying firn/ice layers and change in scattering mechanisms from volume to surface scattering are underlying explanations for varying scattering properties.

Table 5.1: Brief description of seasonal characteristics of different glacier facies and their appearance in RGB Composite. The level of backscatter intensities for each component is mentioned in the cells below.

Glacial Facies	Seasonal Characteristics			Appearance in RGB Composite
	Winter	Early Summer	Late Summer	
	(Blue)	(Red)	(Green)	
Upper Percolation	Dry snow	Dry snow	Dry snow melting	Greenish White
	High	High	Slightly Higher	
Middle Percolation	Dry snow	Dry snow melting	Melting Snow	Pink
	High	High	Low	
Lower Percolation	Dry snow melting	Firn exposed	Firn melting	Blue
	High	Low	Low	
Bare Ice	Snow melting/ Ice exposed	Ice melting	Excessive Ice Melting	Reddish/Greenish Black
	Low	Low	Low	
Debris Covered Ice	Debris	Debris	Debris	Light Grey

The seasonal characteristics of glacier facies seen in IHR are summarized below and briefly described in **Table 5.1.** While Dry Snow Facies, which is composed of loosely packed dry snow crystals, is absent in IHR, Percolation Facies, Bare Ice Facies and Debris Covered Ice Facies are seen.

Percolation Facies:

Similar to what Partington (1998) observed in the Glaciers of Mt. Wrangell in Alaska during their study, three zones are seen within the percolation/wet-snow facies due to melting conditions extending to higher altitudes. Upper Percolation Facies is characterized by high backscatter coefficients throughout the year, appearing white in the RGB composite. The green tint to upper percolation zone comes from beginning of snow melt during late summer, that enhances the backscatter due to slightly enhanced wetness. Excessive water content in the snowpack would reduce the backscatter intensity. Over early and late summer periods, melting extends into the percolation facies, identifying them as the middle and lower percolation zones. They appear as pink and blue, respectively. The temporal change in backscatter intensities over the middle percolation zone is highlighted in **Figure 5.5.** These multi-temporal variations in the percolation zone may be explained by the dry winter conditions, where snow doesn't undergo melting, but only compaction with time. During Early summer, the lower most zone starts to melt, thereby increasing the water content of the snow pack. Further, during late summer warmer conditions extend even higher, leading to slush like formation in the lower most zone. Due to percolation and refreezing of meltwater, ice glands and ice lenses form in those regions exposed to melting conditions during the day and freezing conditions over the night. Firn from previous year may be exposed in the lower percolation zone. During years with low ablation, the lower percolation zone becomes very prominent. However, in case of IHR, as ablation is significant in most of the cases lower percolation zone wasn't present.

End of percolation facies marks the boundary between ablation and accumulation zone of the glaciers in the IHR. ELA is drawn along the boundary of percolation facies and bare ice facies.

Bare Ice Facies:

Bare Ice Facies falls immediately under the ELA, which is the beginning of ablation zone downwards. Super-imposed Ice facies, that is primarily characterized by presence of extensive horizontal ice glands and vertical ice lenses due to refreezing, is absent in glaciers of IHR. Bare Ice Facies is characterized by exposed ice surface throughout the year, subjected to constant melting. Due to presence of surface meltwater, this region appears consistently dark in all the three seasonal images. Snow that falls in this region quickly melts due to warmer temperatures, again exposing the existing ice. However, depending on the period of snow precipitation, the layer may appear slightly reddish-black or greenish-black suggesting snowfall in Early and Late summer periods respectively.

Debris Covered Ice Facies:

As most of the glaciers in IHR are debris covered, a part of Bare Ice facies is debris covered throughout the year with no distinct seasonal or multi-temporal signature. This region is separately classified as debris covered ice facies and extends until the glacier terminus.

5.2.2. Classified Outputs of Study Area
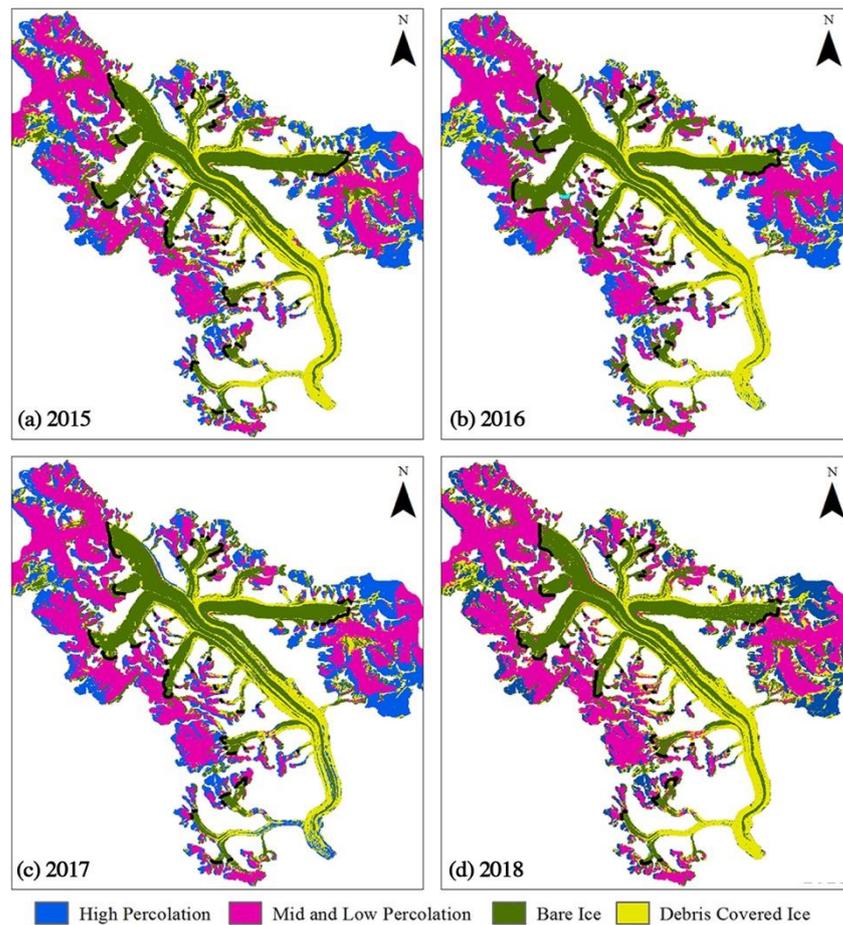
Figure 5.7: Classified maps of Siachen Glacier for years 2015(a), 2016(b), 2017(c) and 2018(d). Equilibrium Line Altitude (ELA) is drawn in black along the boundary of percolation facies and bare ice facies.
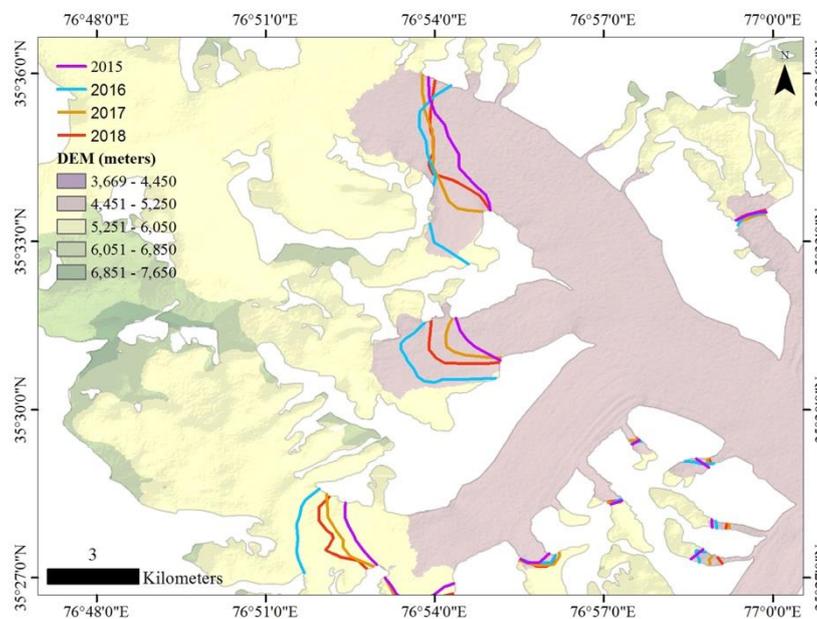
Figure 5.8: Illustration of change in ELA positions over Siachen Glacier between 2015 and 2018. Only a part of the glacier is presented for better understanding.

Classification was performed on 3 glaciers of the study area for a period of 4 years - 2015, 2016, 2017 and 2018. Support Vector Machine (SVM) was used for classification with help of a Radial Basis Kernel. Best results were obtained with $\gamma = 0.3$ and $C = 10$ as input slack parameters to the classifier. The classified outputs, representing different glacier facies, are presented in **Figure 5.7** for Siachen Glacier, **Figure 5.9** for Bara Shigri Glacier and **Figure 5.11** for Gangotri Glacier. Each of these maps present 4 classes of glacier facies – Upper Percolation Zone, Mid and Low Percolation Zone, Bare Ice Zone and Debris Covered Ice Zone. In very few instances, the lower percolation zone was seen. Therefore, it has been merged with middle percolation zone, to make the maps consistent.

It is generally observed that Upper Percolation Facies was present only over Siachen Glacier. Bara Shigri and Gangotri Glacier, that are at relatively lower elevations, are exposed to warmer weather conditions which are not optimal for presence of upper percolation facies. However blue coloured regions (used for indicating upper percolation facies in classified maps) appear over these glaciers due to misclassification of distorted pixels (explained in **Section 6.4),** which generally have very high backscatter and appear white in geometrically corrected SAR products, similar to signatures of upper percolation facies. Signatures of other classes are fairly distinct as seen in **Figure 5.6**. This helps in good classification outputs and accuracies. Using the classified images, ELA for every case was manually digitized carefully with corresponding RGB composite product for support.

Siachen Glacier

The overall accuracy of classified outputs of Siachen Glacier, over different years, was higher than 86.1%. The error matrices along with accuracy values are presented in **Appendix-1**.

The upper percolation facies over this glacier is present on the left tributary (w.r.t the flow direction) above ~6150m.a.s.l. The elevation on the other sides of the glacier is relatively lower, thereby explaining the non-existence of upper percolation facies over those areas. Due to lower elevations, temperatures get warmer over early and late summer initiating the melt of snow packs. Percolation facies, which accounts for the total accumulation zone, consists of approximately 51.2±2.5% of total area covered by the glacier during the study period.

Annual variation of ELA of Siachen Glacier is presented in **Figure 5.8** and listed in **Table 5.2**. It may be noted that ELA of 2016 was at the highest altitude of ~5185±0.7m.a.s.l., while that of 2015 was at the lowest elevation ~5157±1.5m.a.s.l. Only over the major branches of the glacier, ELA displayed a consistent behaviour. Over smaller branches the behaviour was variable, possibly due to its higher sensitivity to surrounding microclimate.

Table 5.2: ELA of different glaciers along the glacier centreline. *Lowest and [†]Highest ELA during the study period.

Assessment Year	Equilibrium Line Altitude (ELA) (m.a.s.l.)		
	Siachen Glacier	Bara Shigri Glacier	Gangotri Glacier
2015	5157±1.5*	5375±2.1*	5133±3.2*
2016	5185±0.7[†]	5397±0.6	5232±3.0
2017	5172±1.9	5407±3.3	5383±2.7[†]
2018	5176±1.1	5409±1.2[†]	5299±4.1

Bara Shigri Glacier

As temporal signatures of the different glacier facies are distinct, overall accuracy of the classified outputs is also high. In case of Bara Shigri Glacier classification, the accuracy is reported at 88.1% or higher. Misclassification is relatively higher at places where one class transforms to another. The error matrices are presented in the **Appendix-1**, at the end of this document.

In Bara Shigri Glacier, Percolation Facies mainly consists of only the Middle Percolation Zone. Upper percolation zone doesn't occur in this region due to beginning of melting of compact dry snow by the early summer periods. As time proceeds from winter to early summer and late summer, temperature rises considerably leading to extensive melting and absence of lower percolation zone. The accumulation zone, that consists of percolation facies, occupies roughly 31.84±3.1% of the total glacier area. Rest ~68% is the ablation zone of the glacier, consisting of Debris Covered Ice and Bare Ice. From the classified maps, presented in **Figure 5.9**, it can be seen debris cover is extensive in case of Bara Shigri Glacier. ELA for every year, based on the classified outputs, is demarcated and presented in **Figure 5.10**. 2015 and 2018 had ELA at the lowest and the highest altitude, respectively, in case of Bara Shigri Glacier. Altitudes of ELA along the glacier centreline from different years are listed in **Table 5.2**.

Gangotri Glacier

The classified outputs of Gangotri Glacier are presented in **Figure 5.11**, while the annual ELAs are shown in **Figure 5.12**. The overall accuracy of classified outputs in case of this glacier was above 89.8%, whose error matrices are presented in **Appendix-1**. From the classified maps, it can be observed that no upper percolation zone is present, and the Percolation Facies only consists of middle percolation zone. Gangotri glacier is exposed to even warmer temperature regimes throughout the year when compared to Bara Shigri and Siachen Glaciers (**Figure 6.5 bottom**), due to which ablation zone occupies significantly larger portion of surface area. 74.2±3.1% is the extent of area covered by ablation zone, consisting of extensive debris cover and small portion of bare ice facies.

ELA in 2015 was significantly lower, at 5133±3.2m.a.s.l. when compared to other years in assessment. Highest ELA was observed in 2017 at 5383±2.7m.a.s.l.
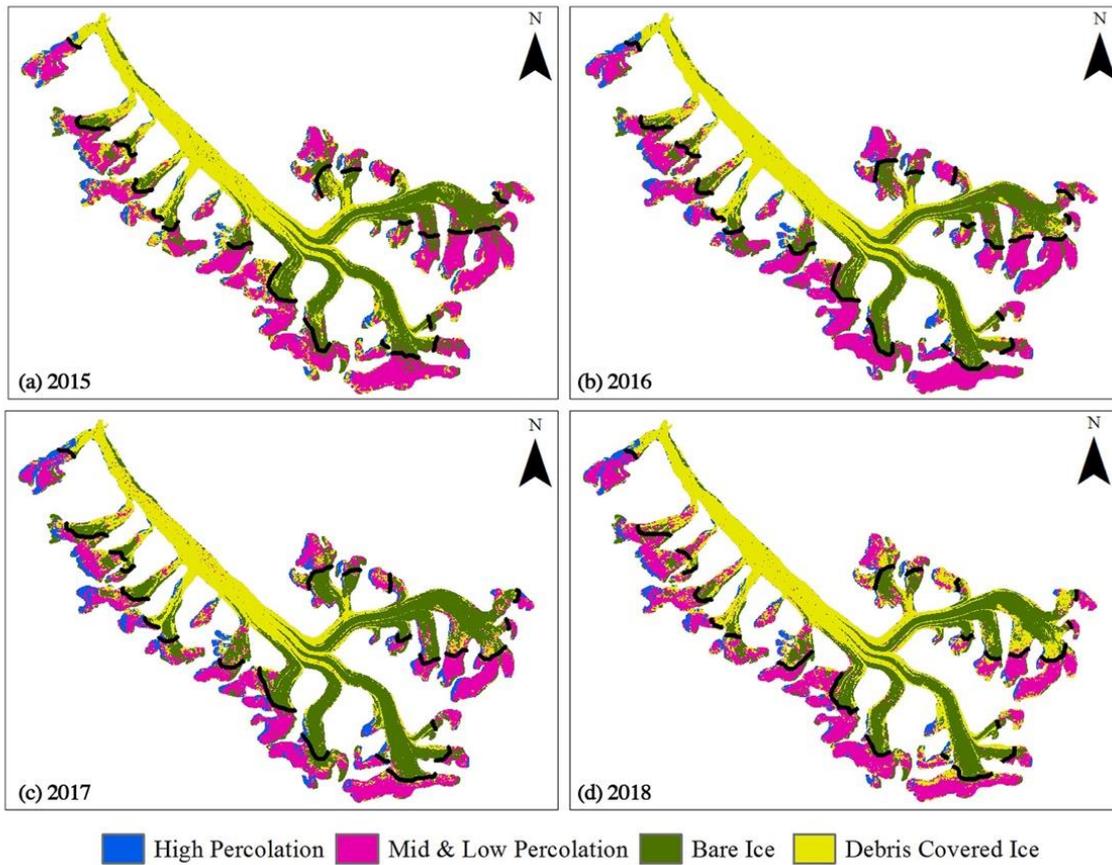
Figure 5.9: Classified maps of Bara Shigri Glacier for years 2015(a), 2016(b), 2017(c) and 2018(d). Equilibrium Line Altitude (ELA) is drawn in black along the boundary of percolation facies and bare ice facies.
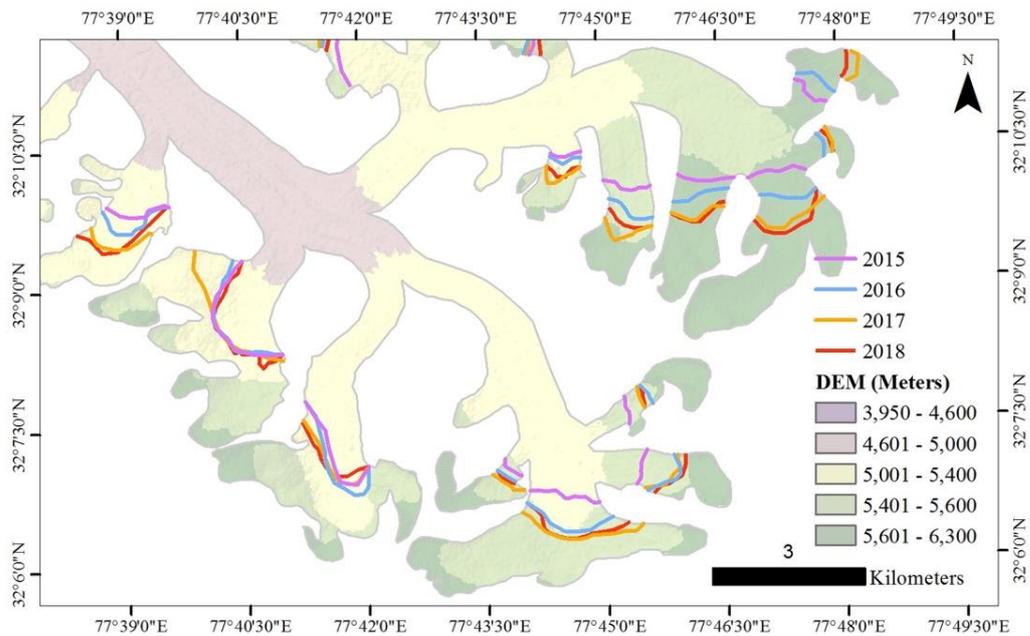
Figure 5.10: Illustration of change in ELA positions over Bara Shigri Glacier between 2015 and 2018. Only a part of the glacier is presented for better understanding.
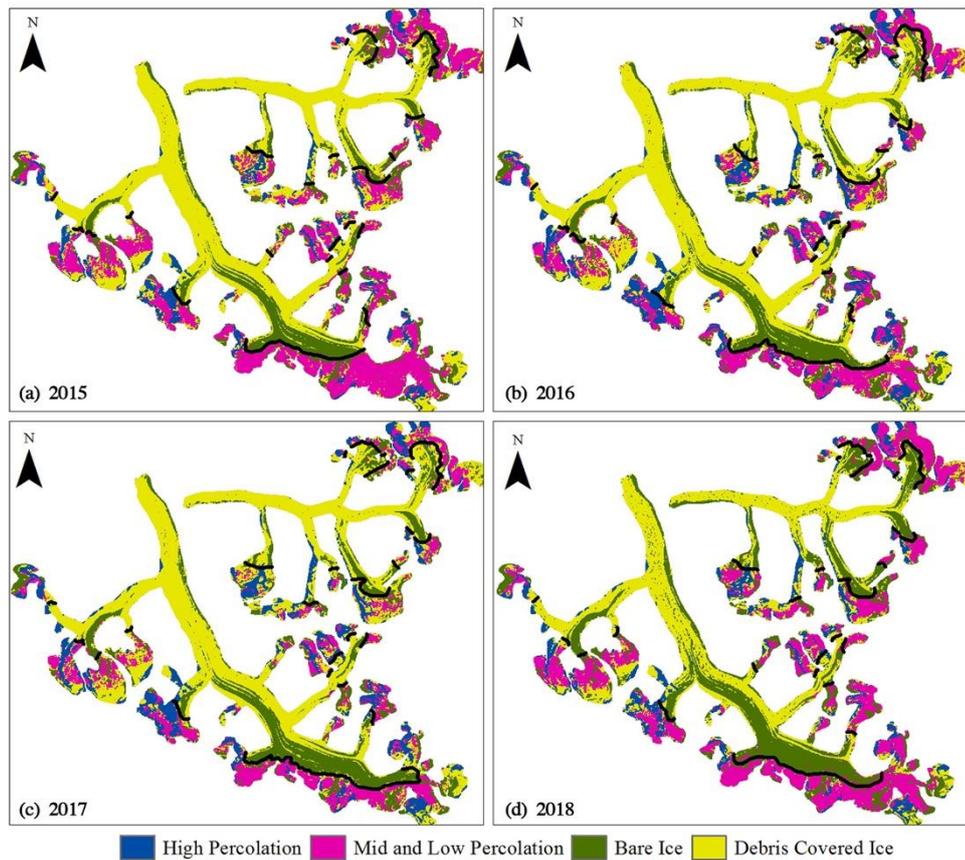
Figure 5.11: Classified maps of Gangotri Glacier for years 2015 (a), 2016(b), 2017(c) and 2018(d). Equilibrium Line Altitude (ELA) is drawn in black along the boundary of percolation facies and bare ice facies.
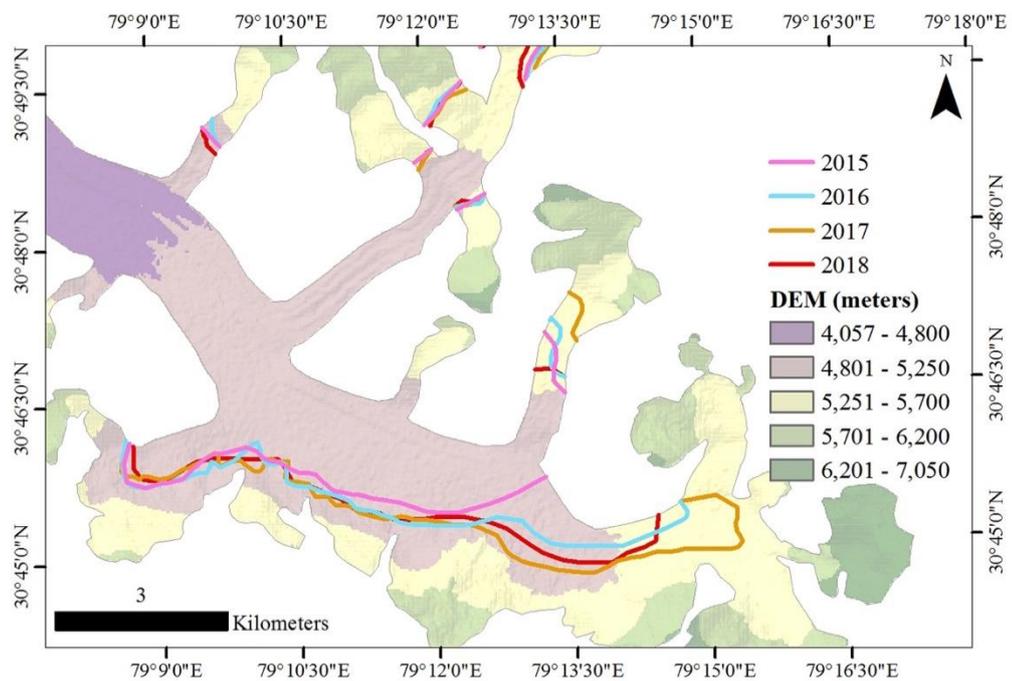
Figure 5.12: Illustration of change in ELA positions over Gangotri Glacier between 2015 and 2018. Only a part of the glacier is presented for better understanding.

6.   DISCUSSION

This chapter presents discussions on the results obtained in this research. Glacier velocities from the past, factors contributing to ELA fluctuation over the study period and the impact of distortions from viewing geometry of SAR systems are described in brief in addition to a note on uncertainty analysis and applicability of Sentinel-1 datasets in IHR.

6.1.   Surface Velocity Analyses and Comparison

For Siachen, Bara Shigri and Gangotri glaciers in IHR, we were able to successfully estimate LOS velocities (**Figure 5.2**) using interferometric pairs from descending nodes of Sentinel-1a/b. These LOS vectors were transformed into actual surface velocity in flow direction (**Figure 5.3**). The images were captured during winter (December 2016), and the estimates were up-scaled to present annual average velocities. Generally, velocities vary during summer and winter seasons, where they are higher during summer periods due to lower friction from the base and easier sliding and lower during winter periods due to higher basal friction and rigidity of snow/ice packs (Satyabala, 2016). Since optimal datasets only from winter periods were available, it was assumed that the velocities are more or less similar throughout the year and therefore up-scaled. To ensure precise velocity estimates, one should essentially consider estimating velocities for summer and winter separately, and use them in combination to present an annual average estimate.

From the velocity maps, it can be seen that among the three glaciers of the study area Siachen Glacier has the fastest velocity, which is significantly higher than the other two glaciers in consideration. With an area of 930sqkm, Siachen glacier stores massive amounts of ice and snow which enhances the stress on the underlying mass leading to higher rates of displacement. Covering an area of 179.9sqkm, Gangotri glacier moves slightly faster than Bara Shigri Glacier whose areal extent is 116.0sqkm. This asserts that areal extent and the glacier mass strongly impact the glacier flow velocity. The variation in areal extent and elevation covered by glaciers in the study area is presented in **Figure 6.1**.
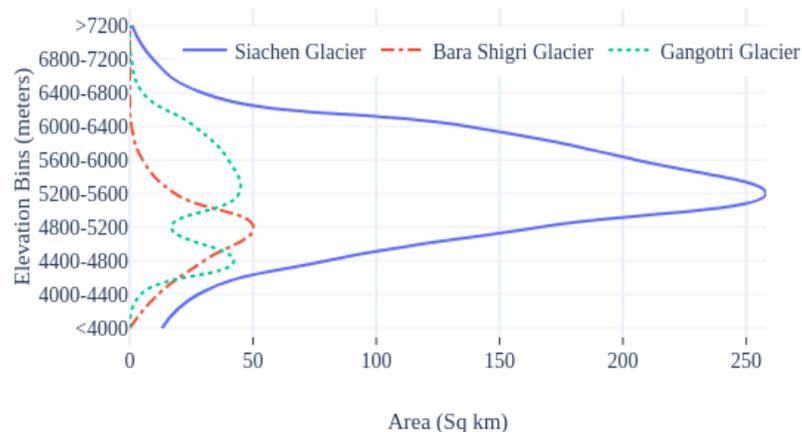
Figure 6.1: Curve plot representing area occupied by glaciers over a specific elevation bin
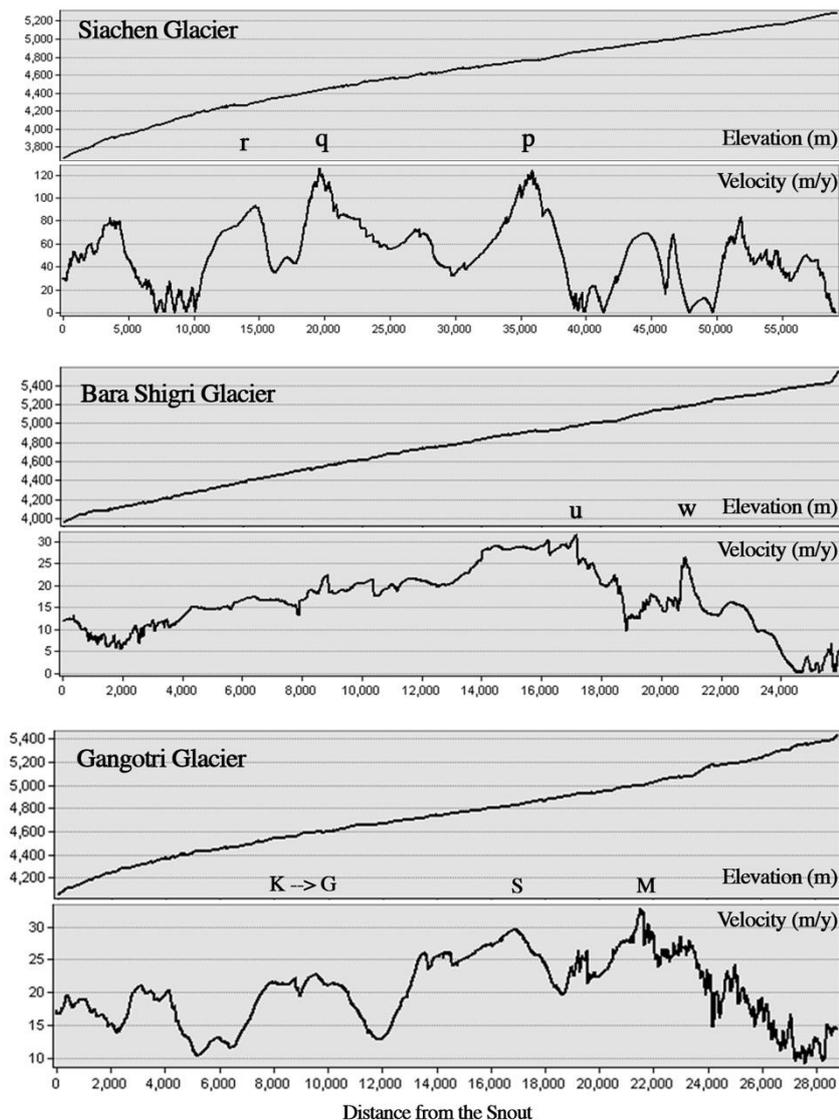
Figure 6.2: Profile plots of elevation and corresponding velocity drawn over Siachen Glacier, Bara Shigri Glacier and Gangotri Glacier. The profile transects are drawn along the glacier centreline, beginning from the snout and upwards, presented in **Figure 5.3**

From **Figure 6.1** and **Figure 6.2**, it can be inferred that a considerable percentage of glacier area lies in higher altitudes, where the ice movement is relatively slower than what is seen in the ablation area. While moving upwards from the snout, a gradual increase in velocity is observed which decreases after a certain distance. Initial stretch near the snout has slow rates of displacement, which may be due to thick debris cover, that can potentially reduce the flow velocity (Bolch et al., 2012), and lower ice thickness. When there is an influx of mass due to joining of tributaries, a sudden increase in glacier velocity is observed. This again asserts that velocity of the glacier is greatly influenced by driving stress exerted by mass influx. This also explains why velocities in accumulation areas are lower than in ablation areas.

Due to lack of field velocity data, the estimates produced from this study couldn't be verified. However, they were compared with published data from the past to gain an idea on the consistency of the estimates. Results for glacier surface velocity of Siachen, Bara Shigri and Gangotri glaciers from this study and from previous studies have been summarized in **Table 6.1**.

Table 6.1: Comparison of velocity estimations. ([†]Average annual velocity; *Maximum Velocity).

Reference	Glacier Name	Method of assessment	Period of Assessment	Glacier Velocity (m/y)		This study (m/y)
				Summer	Winter	
Kumar, Venkataraman, & Høgda (2011)	Siachen Glacier	DInSAR	1996	[†]125-140 (*43cm/day)		*135.27±5.1
Garg et al. (2017)	Bara Shigri	Optical Ft. Tracking	2002-2003	*59.2		*32.5±2.15
			2013-2014	*42.4		
Satyabala (2016)	Gangotri Glacier	SAR Offset Tracking	1992-1993	[†]63.1±5.4	[†]29.4±2.6	*41.85±7.32
			1999	[†]66.6 ± 6.0	[†]33.5 ± 2.9	
			2004	[†]58.2±4.5	[†]25.7 ± 2.3	
			2007	[†]42.8±4.2	[†]26.9 ± 1.9	
Bhattacharya et al. (2016)	Gangotri Glacier	Optical Feature Tracking	1993-1994	[†]46 ± 7.5		
			1998-1999	[†]50 ± 7.2		
			2008-2009	[†]48 ± 4.8		
			2006-2014	[†]44.7 ± 4.9		
			2013-2014	[†]43.0 ± 5.1		

The velocity estimates presented for Siachen Glacier (**Figure 5.3a**) show a maximum displacement of 135.27±5.1m/y at point 'p', located ~38kms above the snout of the glacier. Between 'p' and 'q' the average velocity was found to be 83.2±10m/y. These results are very much comparable with the results presented by Kumar, Venkataraman, & Høgda (2011), where they report highest velocity of 156.95m/y (43cm/day) at a location similar to point 'p'. Additionally, between 'p' and 'q', they observed an average velocity of 102.2m/y (28cm/day). The difference in estimates in the 2 studies may be due to the difference in time periods. While this study used datasets from 2016, the previous study reported results from 1996. Loss of glacier mass over the 20 years would have reduced the driving stress. Additionally, the estimates of this study are from winter, while that of the previous study are from summer, also explaining the substantial decrease in reported rates of displacement over Siachen Glacier.

Strong agreement in velocities of Bara Shigri Glacier can also be seen between results of this study (**Figure 5.3b**) and results presented by Garg et al. (2017). They presented velocity estimates using Optical Feature Tracking for 2002-2003 and 2013-2014. At point 'u', ~16km from the snout, they reported a velocity of approximately 35m/y for 2013-2014, which is similar to the estimate from this study, 32.5±2.15m/y. The difference can be explained by annual average estimate of theirs, compared to winter estimate in this case. Considering the size of the glacier and minor temporal difference in study periods of the two studies, very minimal temporal variation in velocities is expected.

Surface velocity estimation of Gangotri Glacier between 1992 and 2007 was carried out by Satyabala (2016) using SAR based Offset Tracking approach. For similar time periods Bhattacharya et al. (2016) also reported velocity estimates using Optical Feature Tracking. Their results are strongly consistent and are used to assess the outputs presented in this study using Differential SAR Interferometry. At point 'S', shown in **Figure 5.3c**, which is ~18km above the snout of the glacier, a velocity of 32.7±3.18m/y is estimated from our analysis. Whereas, Satyabala (2016) reported 47.5m/y for the same region, calculated using remotely sensed images from Feb-March 2008. Gangotri glacier is one of the most rapidly melting glaciers in the IHR, which could have lost mass between 2008 and 2016. Trend of negative mass balance, since 1993, is also presented

by Bhattacharya et al. (2016) which asserts the argument that decline in velocity over Gangotri Glacier may be due to lower stress from the standing mass of the glacier.

6.2.   ELA Fluctuation between 2014 & 2018

Equilibrium Line Altitude (ELA) which separates the ablation zone of the glacier from the accumulation zone is a reliable indicator of glacier health (Kulkarni, 1992). Over warming conditions, the ELA moves higher up in elevation thereby reducing the area covered by the accumulation zone and increasing the area of ablation, indicating a negative mass balance or declining glacier health. On the other hand, during freezing conditions ELA moves lower in elevation indicating positive mass balance and advancing health of the glacier. This sensitive behaviour of ELA fluctuation can be used to analyse immediate glacier response to exposed climatic conditions, and corresponding glacier state.

ELA, which is also measured as the Snow Line Altitude during glacier melt season, is strongly influenced by surrounding climatic conditions. After classification of glacier facies, we were able to successfully delineate the annual ELA for glaciers in consideration for the years 2015, 2016, 2017 and 2018. Their results are represented in **Figure 5.7** to **Figure 5.12** of Chapter 5. To analyse the fluctuations observed in ELA for a
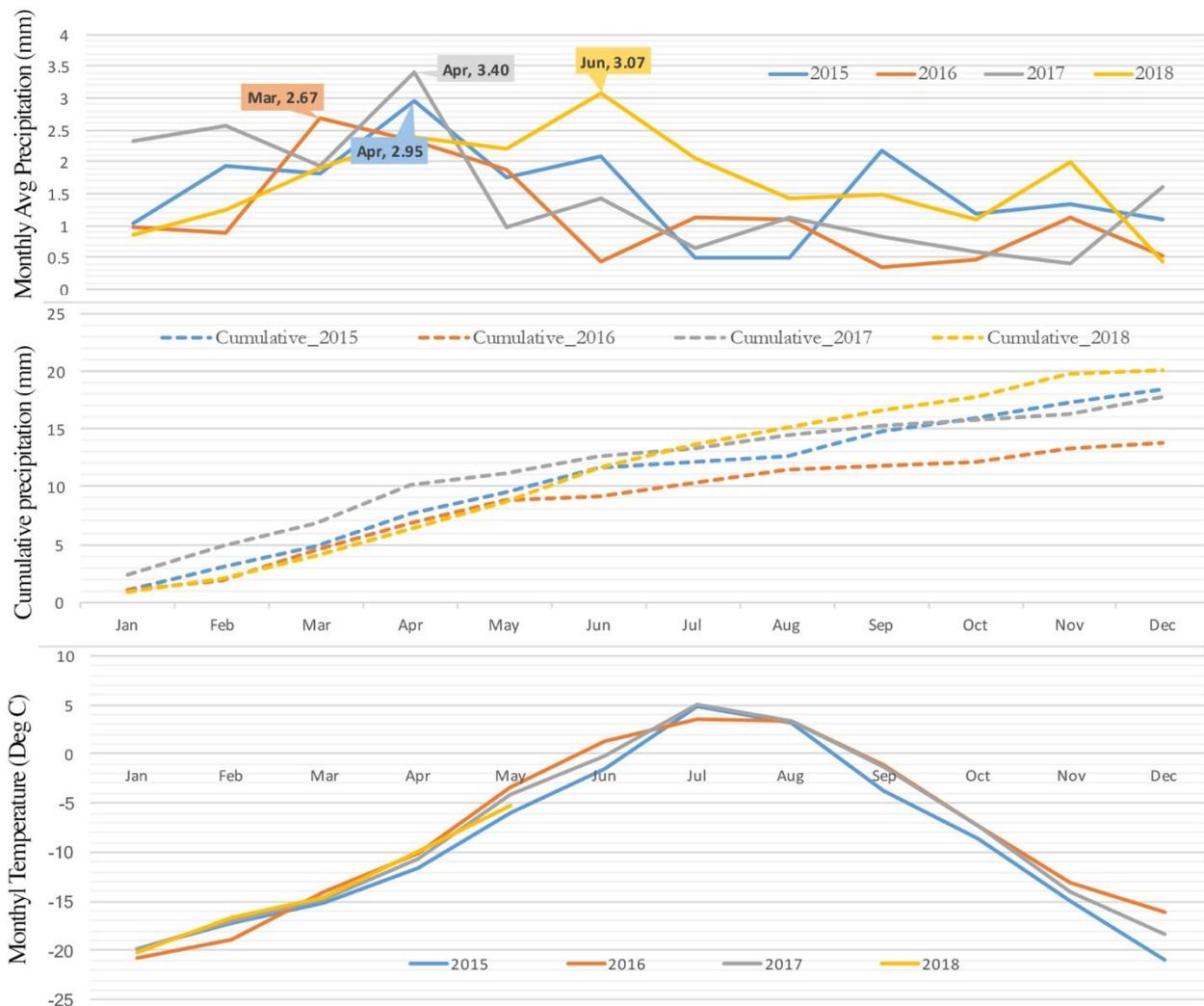
Figure 6.3: Climatic conditions illustrated by precipitation and temperature surrounding Siachen Glacier. Top: Average Monthly Precipitation vs Time; Middle: Cumulative Precipitation vs Time; Bottom: Average Temperature vs Time
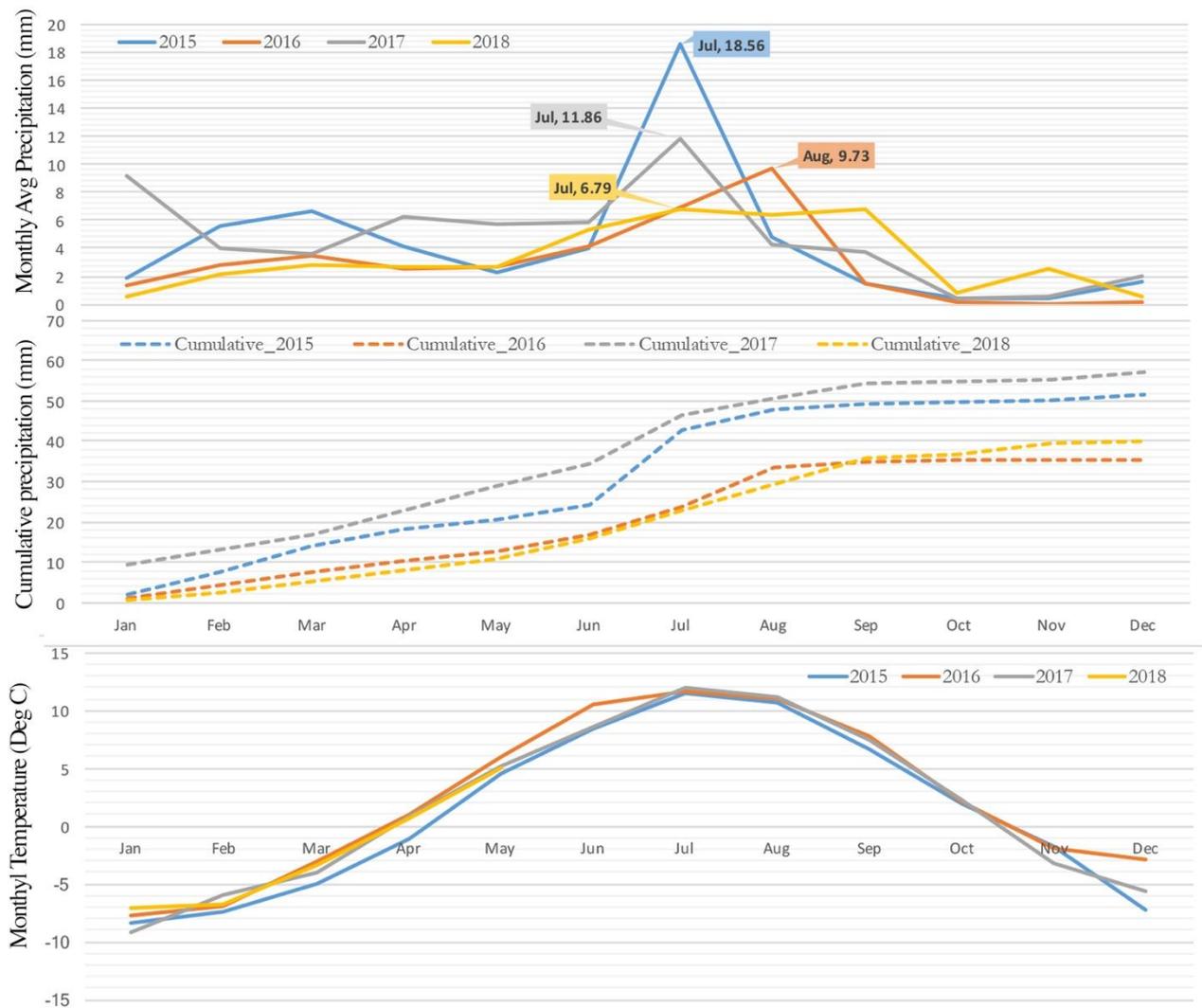
Figure 6.4: Climatic conditions illustrated by precipitation and temperature surrounding Bara Shigri Glacier. Top: Average Monthly Precipitation vs Time; Middle: Cumulative Precipitation vs Time; Bottom: Average Temperature vs Time

specific glacier, it is important to understand the climatic conditions that the glacier is exposed to over the year in consideration. Using ERA Interim Atmospheric Reanalysis product, we have extracted average monthly precipitation and average monthly temperature surrounding Siachen, Bara Shigri and Gangotri Glaciers and plotted them as graphs in **Figure 6.3**, **Figure 6.4** and **Figure 6.5** respectively. Upon analysis of these graphs, it is understood that winter precipitation is significant over the west (Siachen Glacier) and it's impact gradually decreases as we move eastwards towards Bara Shigri and Gangotri Glaciers. As Bara Shigri and Gangotri Glaciers are not very far apart, the difference in magnitude of winter precipitation is low. A warming trend of temperature regimes is also seen in the order: Siachen Glacier < Bara Shigri Glacier < Gangotri Glacier, making Gangotri glacier most sensitive glacier among the three.

Observing changes to ELA of Siachen Glacier from **Figure 5.8** it is stated that in 2015 ELA was at the lowest altitude (5157±1.5m.a.s.l.), while highest elevation was reached in 2016 (5185±0.7m.a.s.l.). Heavy precipitation accompanied by low temperature conditions, maintained stability over the glacier surface in 2015 thereby reducing melt. On the other hand, 2016 was a low precipitation year, also with relatively warm temperatures in March, April, May and June 2016 which could have led to enhanced surface melting of
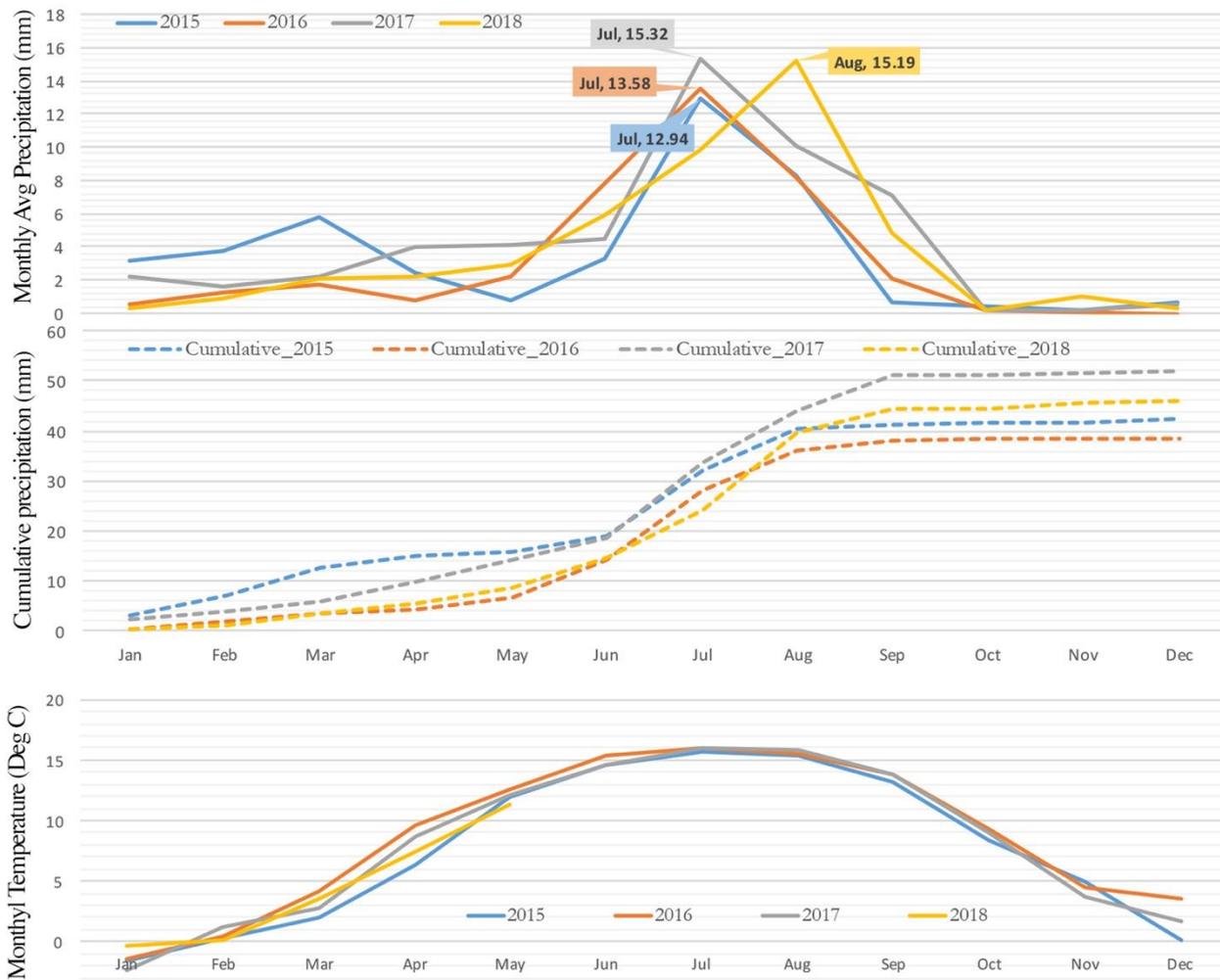
Figure 6.5: Climatic conditions illustrated by precipitation and temperature surrounding Gangotri Glacier. Top: Average Monthly Precipitation vs Time; Middle: Cumulative Precipitation vs Time; Bottom: Average Temperature vs Time

stored snow/ice stock causing ELA to shift higher in altitude. ELAs of 2017 and 2018 maintained stability at 5174±2.7m.a.s.l.

Similar weather conditions extended over Bara Shigri and Gangotri Glacier regions as well in 2015, with heavy precipitation and low average temperatures. ELAs in case of these two glaciers were also lowest in 2015 at 5357±2.1m.a.s.l. and 5133±3.2 m.a.s.l. respectively. Whereas, the maximum equilibrium altitude of Bara Shigri Glacier was attained in 2018, which received very low precipitation from westerlies, that accounts to accumulation of glacier mass. From **Figure 6.4** (bottom), it can also be seen that temperatures in initial months of 2018 remained on the higher side which further asserts the reason for higher altitude of equilibrium in 2018. Although precipitation in 2017 was high (around Bara Shigri glacier), it was accompanied by higher temperature averages, suggesting that precipitation would have been in a wetter form with higher liquid water content. Such snowfall is sensitive and melts faster. This suggests that temperature may have higher influence than precipitation over the altitude of equilibrium. Similar behaviour is observed in case of Gangotri Glacier also, which reasserts the finding.

6.3.   Reporting Errors

Glacier velocities estimated using interferometric approaches are affected by various sources of error, that give rise to uncertainty in the estimated values. While phase decorrelation, atmospheric phase delay, orbital inaccuracies and sensor characteristics (thermal and quantization noise) are some components of acquisition errors (Δacq), processing steps such as coregistration, multilooking, phase unwrapping and filtration are components of processing errors (Δproc), described in detail in **Section 4.1.5.** We, in this study, collectively refer these errors as phase noise ($\Delta\varphi_{noise}$) which defines uncertainties associated with LOS velocities. As quantification of $\Delta\varphi_{noise}$ is highly complicated, we assume a constant value of 5.0mm/epoch for Sentinel-1 products.

LOS velocity vectors are further transformed to surface flow velocities using a function that further adds to the error (Δtf) due to averaging of slope, aspect and incidence angle. As only one interferometric pair is used for estimation, the sensitivity of glacier deformation is selective in a particular direction. Defined by sensitivity (s), this is an additional component considered towards analysis of uncertainty in this study. Therefore, the error propagation for velocity estimates in our study is given by

$$Error = \frac{[(\Delta acq + \Delta proc) * (\Delta tf)]}{s} \qquad (6.1)$$

Errors in the altitude of equilibrium are given by classification inaccuracies and resolution of DEM used. As precise estimation of error propagation is difficult in this case, we delineated ELAs five times and used the standard deviation as associated error.

6.4.   Effect of Distortions due to SAR acquisition geometry

In this study datasets captured by the Interferometric Wide Swath mode of SAR sensors aboard Sentinel-1a/b are used. The incidence angle at which these sensors acquire images range between 29.16° to 46.00°. Due to the slanting line of sight of SAR sensors, elevated areas will display significant geometric distortions, in form of layover, shadow and foreshortening when geometrically terrain corrected. Since the techniques used in this study for estimating velocity and performing classification involve geometrically corrected intermediates or results, the outputs along such regions may be poor, incorrect and unreliable in most of the cases. **Figure 6.6** presents a layover, shadow and foreshortening mask for S1a/b SAR products. Upon careful observation of the figure it can be seen that substantial regions from the higher reaches and edges of the glaciers are affected by these distortions. Dotted boxes drawn over the image highlight some of the areas of glacier overlapping with areas where distortions may occur. In these regions, results produced are incorrect and should be carefully analysed taking these factors into consideration.

For classification, geometrically corrected composites are used. The radar backscatter in these regions is significantly high and doesn't reflect the actual scattering characteristics of the corresponding objects on ground. As a result, most of these regions are misclassified and account for error. During velocity estimations, terrain correction is done in the last to avoid propagation of error. Displacement in those regions will be far from actual velocity observations on ground.
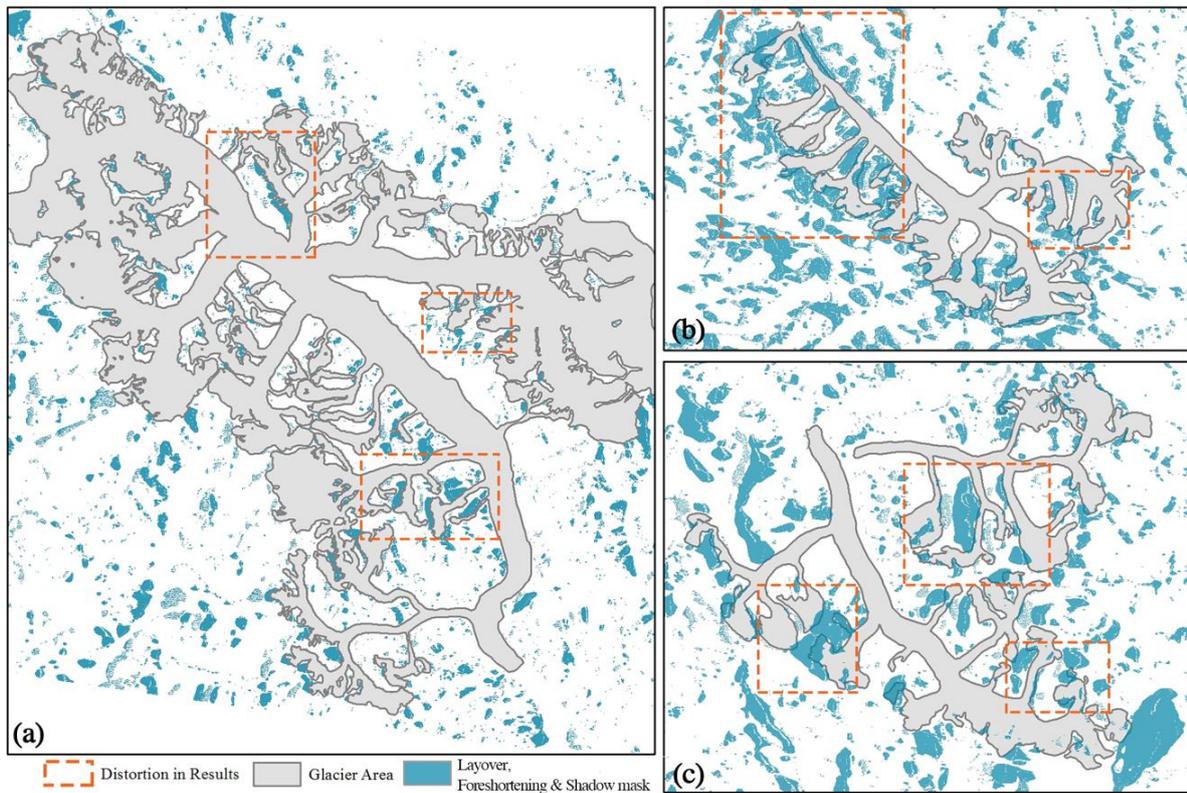
Figure 6.6: Layover and Shadow mask (blue colour) generated considering the viewing geometry of Sentinel-1a/b sensors during acquisition. Example of areas that may have an impact on the results estimated in this study are highlighted using dotted boxes.

Considering these distortions, we do not present glacier-wide averaged estimates of surface velocity. Whereas most of the other studies report averaged velocities for complete glacier area. Further, based on classified outputs, calculating total areas representing a particular facies will also be a wrong estimation. Therefore, only approximate estimates as percentage of total area are reported rather than precise values.

6.5. Applicability of Sentinel-1 Products in IHR

In this study we have used Sentinel-1 products for estimating glacier velocities and facies classification over 3 glaciers from the IHR. While a set of any 3 images can be used for classification, for velocity estimation there are several constraints involved in the choice of datasets. Based on the availability of required (optimal) datasets, we share a note on applicability of Sentinel-1 products for assessing glacier velocities specifically in IHR. Previously, datasets only from ERS-1/2 with a 1-day temporal baseline over IHR permitted DInSAR based velocity estimations in the glaciers of this region. Products from none of the other SAR missions could be used due to higher temporal baselines.

Recently launched Sentinel-1 mission offers an opportunity for DInSAR processing in the Himalayas. However, the availability of datasets over this region is not how one would generally expect. The passes of Sentinel-1a over the IHR are regular and available throughout the year in both ascending and descending passes. A pool of 12-day pairs are thus available from S1a for InSAR processing. On the other hand, passes of Sentinel-1b are irregular and minimal, with operation over the IHR only in winter periods. Moreover, S1b covers IHR only during the descending pass, while no products are available from the ascending pass. In addition to this, spatial coverage of S1b in IHR was reduced in winter of 2017 (NDJ), and none in 2018. Due to this orbital setting of S1a and S1b, 6-day interferometric pairs are few and are available only from the descending pass. Assessment of these 12-day and 6-day pairs must be done carefully to ensure reliable outputs of estimations.

In **Figure 6.7** coherence bands generated using 3 different interferometric combinations are presented. **Figure 6.7a** presents coherence band from 12-day temporal separation using datasets from 28-Nov-16 and 10-Dec-16. **Figure 6.7b** presents results of coherence estimation using a pair temporally separated by 6-days (10-Dec-17 and 16-Dec-17) and **Figure 6.7c** presents coherence obtained from 6-days separated interferometric pair with an event of precipitation (21-Dec-17 and 27-Dec-17). Careful assessment of these coherence estimates suggests, 6-day pairs are optimal for DInSAR processing in IHR. However, the degree of correlation in these pairs may be affected by events of snowfall, rainfall, windstorms and avalanches if occurred between the dates of acquisition of the master and the slave.
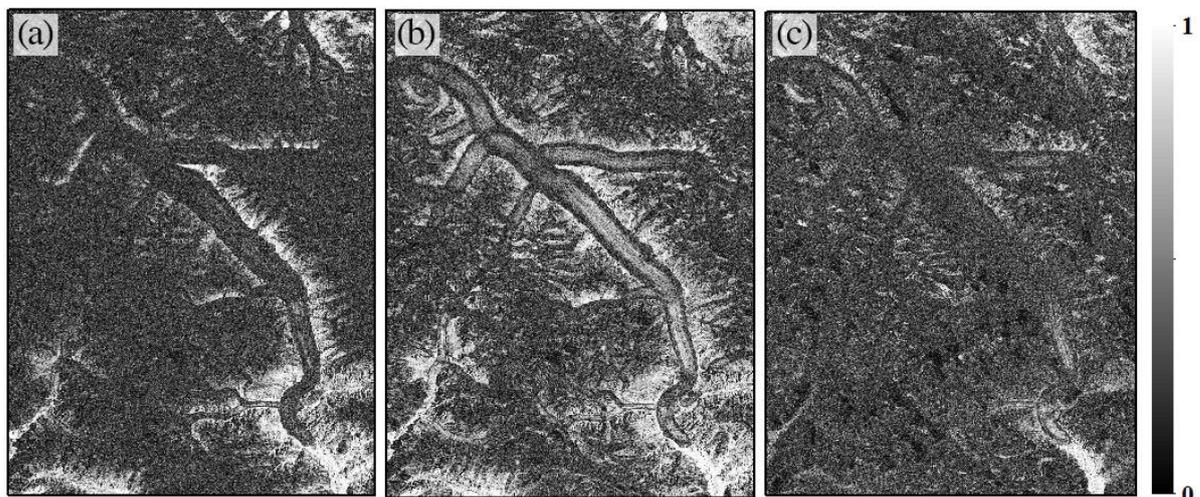
Figure 6.7: Coherence estimated using (a) 12-day temporal baseline (b) 6 day temporal baseline and (c) 6 day temporal baseline with an event of precipitation

On summary, Sentinel-1 datasets are applicable for DInSAR analysis in IHR and require careful assessment for identifying an ideal pair for processing. This is presented as a SWOT outline below for easier and better understanding of applicability in IHR.

Strengths

The primary advantage of S1 products is the ability to offer low temporal baselines, which none of the other repeat-pass SAR missions currently in operation provide. Further, the long term data availability from the mission will be an added advantage along with identical imaging geometries of its constellation. This offers an exciting opportunity for glacier assessment and monitoring over the Indian Himalayan Region. Moreover, these datasets are completely free-of-cost and can be downloaded as-and-when-required from ESA's data portal.

Weakness

Unlike passes of S1a, the passes of S1b are orbitally aligned/planned such that there are minimal and highly irregular visits over the IHR. Additionally, spatial coverage (regions covered) is also not consistent over the years of operation. This brings down the number of 6-day separated pairs to a very low number.

Opportunities

Nevertheless, these few pairs can potentially help in performing glacier assessments in the region using SAR interferometric tools. Choosing glaciers based on the availability of 6-day pairs can put us in an ideal scenario where at least a few sets are available for analyses. This can be used to generate valuable knowledge about glacial processes and dynamics in IHR.

Threats

Not all 6-day pairs may be applicable for interferometric processing due to other factors such as acquisition errors, geometric baselines, unfavourable atmospheric conditions during acquisition and events of precipitation/avalanches/windstorms between acquisitions. These can potentially affect coherence between the master and the slave, rendering the pair non-usable for interferometric analysis. Careful pre-assessment of the dataset needs to be performed beforehand.

7.   CONCLUSIONS

The primary objective of this research was to use Sentinel-1 products for assessing glacier velocities and classifying glaciers into different radar facies in the Indian Himalayan Region. Sentinel-1 datasets were used for the first to assess velocities in IHR in this study. Notably, these products have exhibited their ability to produce highly reliable results of velocity, however applicability of these datasets is limited to availability of ideal 6-day interferometric pairs over the study area. 6-day separated pairs are only available when products from S1a and S1b are used in combination. Due to minimal and irregular passes of S1b, very few pairs may be available from the winter periods of selected years. Events such as snowfall, rainfall, windstorms, avalanches and rapid melting may hamper the applicability of the few available pairs. This requires careful pre-assessment to find optimal pairs for interferometric investigations.

Siachen, Bara Shigri and Gangotri Glaciers were chosen for this study, taking into account their variable size, location and climatic exposure. With help of few optimal pairs acquired from the descending pass, we were able to successfully retrieve surface velocities of these glaciers. Our findings for all 3 glaciers are strongly in agreement with estimates from the past, available through published literature. The maximum velocities estimated for 2016 over the main trunks are reported to be 135.27±5.1m/y, 32.5±2.15m/y and 32.7±3.18m/y for Siachen, Bara Shigri and Gangotri Glaciers respectively. Upon comparison it is understood that velocities have gradually reduced over the past 20 years. This decline is explained by the reduced driving stress from standing glacier mass due to negative balance in the region. Due to insignificant change in glacier mass between 2014 and 2016, the velocities were observed to be consistent. It may be noted that velocities were generated using single interferometric pair, estimates of which are reliable only in LOS direction. The sensitivity metrics that are presented in this study help in understanding the most sensitive direction of flow, given the basal slope of glacier and geometry of Sentinel-1 sensors. Movements along the major trunks of three glaciers had an average sensitivity of 0.66, 0.61 and 0.55 respectively. Sensitivity of movement over the glacier tributaries were lower. Sensitivity, phase noise (acquisition errors and processing errors) and transformation errors were used to determine the range of uncertainties associated with estimates. As the acquisition errors and processing errors cannot be calculated, we assumed a constant value of 5mm/epoch for every pixel as $\Delta\varphi_{noise}$. To generate 2D/3D surface displacement and make estimates more sensitive, additional pair from another viewing geometry (ascending pass) may be required. However, 6-day pairs are not available from ascending pass, making this a major limitation for usage of Sentinel-1 datasets in IHR for 3D surface velocity assessments.

Multi-temporal SAR approach for classification of glacier facies uses datasets from winter, early summer and late summer. Sentinel-1a products, which were available for the whole year, were used for classification of radar zones between 2015 and 2018. Upon analysis of classified outputs, high degree of coherence (>85% in all cases) was found between the results and validation points picked using VHR optical datasets and previously classified images as reference. Percolation Facies, Bare Ice Facies and Debris Covered Ice Facies were seen over the chosen glaciers. Upper percolation zone was present only over Siachen Glacier due to the extreme cold conditions that the glacier is exposed to throughout the year. Further, ELAs delineated using classified outputs were carefully analysed to understand the trends of evolution. While the line of

equilibrium gradually moved higher between 2015 and 2018 for Siachen and Bara Shigri glaciers, in case of Gangotri glacier it varied differently. Highest variation of ELA was seen over Gangotri glacier due to extreme warming conditions that the glacier is exposed to, suggesting that Gangotri glacier is highly sensitive among the three. It was also found that temperature surrounding the glacier had a higher influence on ELA variation than precipitation. These findings, altogether, substantiate the negative mass balance trends prevailing over the IHR. With these findings the research questions are answered as follows:

Question 1: What is the estimated surface velocity of the chosen glaciers?

Surface velocity estimated using DInSAR approach ranges between 0m/y to 135.27±5.1m/y over Siachen Glacier, 0m/y to 32.5±2.15m/y over Bara Shigri Glacier and 0m/y to 41.85±7.32m/y over Gangotri Glacier. The velocity was observed to be highest over the main trunks of these glaciers, and is driven by influx of mass and the stress that is exerted over the underlying ice.

Question 2: What are the different glacier facies identified using Multi-temporal SAR Approach in IHR?

Over the Indian Himalayan Region, specifically Siachen, Bara Shigri and Gangotri Glaciers, following facies were identified – Percolation Facies, Bare Ice Facies and Debris Covered Ice Facies. Further, three zones were identified within the Percolation Facies, namely the Upper Percolation Zone, Middle Percolation Zone and Lower Percolation Zone. Upper Percolation Zone is present only on glaciers in extremely cold regions, e.x. Siachen Glacier in the Karakoram Range, while Middle and Lower Percolation Zones were present consistently throughout the study area. Dry Ice Facies and Super-Imposed Ice Facies are not seen in this region, generally.

Question 3: How accurate are the results of classification?

Due to distinct characteristics of seasonal radar backscatter from corresponding glacier facies, it was possible to obtain highly coherent training samples. High levels of accuracy (85% - 93%) were obtained from comparison of the classified maps with validation points. Accuracies are very poor over the higher reaches of the glaciers which are impacted by geometric distortions due to acquisition geometry of SAR. This, however, doesn't impact the ELA analysis which is performed using the classified outputs.

Question 4: What is the quality of the velocity estimated using Sentinel-1?

The quality of the velocity estimated using Sentinel1 depends on the vector of displacement. As only 1 interferometric pair is used for estimation, the estimate will be most sensitive in the LOS direction. For Sentinel-1a and -1b sensors, the radar beam direction is $\zeta = 280°$. The primary direction of movement (along the main trunk) of Siachen, Bara Shigri and Gangotri glaciers is approximately $\beta = 130°$, 315° and 320.5° respectively. The average sensitivity along the main trunks of these glaciers is 0.66, 0.61 and 0.55 respectively. However, sensitivity over tributaries and other parts of the glacier may significantly vary.

Question 5: How has ELA evolved/changed over the study period and what impacts the change?

Over Siachen and Bara Shigri Glaciers, line of equilibrium gradually moved higher in altitude by 5-6m.a.s.l./y. The fluctuation over Gangotri Glacier's ELA was variable. Here, due to extensive snow fall and low temperature atmosphere in 2015, the ELA was 70m (on average) lower in altitude compared to other years. It was also observed that temperature had a higher influence, than precipitation, over the Equilibrium Line Altitude. Changes in ELA indicate instability and negative mass balance over all the thee glaciers.

Future Scope

- 2D/3D surface velocity estimations should be performed by combining azimuth displacements from Offset tracking/ Multiple Aperture Interferometry (MAI) and range displacements from DInSAR.
- Assessments over other regions of Himalayas (Central and Eastern) should also be performed.
- Findings from satellite assessments should be substantiated with field observed information.
- Further in-depth analysis on sensitivity of the results is required.
- Multi-component analysis should be performed to get a comprehensive idea of glacier dynamics and future evolution.

LIST OF REFERENCES

Akbari, V., Doulgeris, A. P., & Eltoft, T. (2014). Monitoring Glacier Changes Using Multitemporal Multipolarization SAR Images. *IEEE Transactions on Geoscience and Remote Sensing*, *52*(6), 3729–3741. http://doi.org/10.1109/TGRS.2013.2275203

Armstrong, R. L., & Brun, E. (2008). *Snow and Climate: Physical Processes, Surface Energy Exchange and Modeling*. Cambridge University Press.

Azam, M. F., Wagnon, P., Vincent, C., Ramanathan, A. L., Favier, V., Mandal, A., & Pottakkal, J. G. (2014). Processes governing the mass balance of Chhota Shigri Glacier (western Himalaya, India) assessed by point-scale surface energy balance measurements. *Cryosphere*, *8*(6), 2195–2217. http://doi.org/10.5194/tc-8-2195-2014

Bajracharya, S. R., & Mool, P. (2009). Glaciers, glacial lakes and glacial lake outburst floods in the Mount Everest region, Nepal. *Annals of Glaciology*, *50*(53), 81–86. http://doi.org/10.3189/172756410790595895

Balsamo, G., Albergel, C., Beljaars, A., Boussetta, S., Brun, E., Cloke, H., … Vitart, F. (2015). ERA-Interim/Land: a global land surface reanalysis data set. *Hydrology and Earth System Sciences*, *19*, 389–407. http://doi.org/10.5194/hess-19-389-2015

Benn, D., & Evans, D. J. A. (2010). *Glaciers and Glaciation* (2nd ed.). London, UK: Routledge. Retrieved from http://ebookcentral.proquest.com/lib/itc/detail.action?docID=615876

Bhambri, R., Bolch, T., Chaujar, R. K., & Kulshreshtha, S. C. (2011). Glacier changes in the Garhwal Himalaya, India, from 1968 to 2006 based on remote sensing. *Journal of Glaciology*, *57*(203), 543–556. http://doi.org/10.3189/002214311796905604

Bhattacharya, A., Bolch, T., Mukherjee, K., Pieczonka, T., Kropáček, J., & Buchroithner, M. F. (2016). Overall recession and mass budget of Gangotri Glacier, Garhwal Himalayas, from 1965 to 2015 using remote sensing data. *Journal of Glaciology*, *62*(236), 1115–1133. http://doi.org/10.1017/jog.2016.96

Bisht, S. M. (2015). *Study of Gangotri Glacier Dynamics using Remote Sensing and Geospatial Tools (Master's Thesis)*. IIRS, Andhra Univeristy.

Bliss, A., Hock, R., & Radić, V. (2014). Global response of glacier runoff to twenty-first century climate change. *Journal of Geophysical Research: Earth Surface*, *119*(4), 717–730. http://doi.org/10.1002/2013JF002931

Bolch, T., Kulkarni, A. V., Kääb, A., Huggel, C., Paul, F., Cogley, J. G., … Stoffel, M. (2012). The state and fate of himalayan glaciers. *Science*, *336*(6079), 310–314. http://doi.org/10.1126/science.1215828

Bookhagen, B., & Burbank, D. W. (2010). Toward a complete Himalayan hydrological budget: Spatiotemporal distribution of snowmelt and rainfall and their impact on river discharge. *Journal of Geophysical Research*, *115*(F3), F03019. http://doi.org/10.1029/2009JF001426

Boser, B. E., Guyon, I. M., & Vapnik, V. N. (1992). A Training Algorithm for Optimal Margin Classifiers. In *Proceedings of the 5th Annual ACM Workshop on Computational Learning Theory* (pp. 144–152). ACM Press. http://doi.org/10.1.1.21.3818

Bürgmann, R., Rosen, P. A., & Fielding, E. J. (2000). Synthetic Aperture Radar Interferometry to Measure Earth's Surface Topography and Its Deformation. *Annual Review of Earth and Planetary Sciences*, *28*(1),

169–209. http://doi.org/10.1146/annurev.earth.28.1.169

Callegari, M., Carturan, L., Marin, C., Notarnicola, C., Rastner, P., Seppi, R., & Zucca, F. (2016). A Pol-SAR Analysis for Alpine Glacier Classification and Snowline Altitude Retrieval. *IEEE Journal of Selected Topics in Applied Earth Observations and Remote Sensing*, *9*(7), 3106–3121. http://doi.org/10.1109/JSTARS.2016.2587819

Callegari, M., Marin, C., & Notarnicola, C. (2017). Multi-temporal and multi-source alpine glacier cover classification. In *2017 9th International Workshop on the Analysis of Multitemporal Remote Sensing Images (MultiTemp)* (pp. 1–3). IEEE. http://doi.org/10.1109/Multi-Temp.2017.8035233

Camps-Valls, G., Gómez-Chova, L., Calpe-Maravilla, J., Martín-Guerrero, J. D., Soria-Olivas, E., Alonso-Chordá, L., & Moreno, J. (2004). Robust support vector method for hyperspectral data classification and knowledge discovery. *IEEE Transactions on Geoscience and Remote Sensing*, *42*(7), 1530–1542. http://doi.org/10.1109/TGRS.2004.827262

Chang, L., Dollevoet, R. P. B. J., & Hanssen, R. F. (2018). Monitoring Line-Infrastructure With Multisensor SAR Interferometry: Products and Performance Assessment Metrics. *IEEE Journal of Selected Topics in Applied Earth Observations and Remote Sensing*, *11*(5), 1593–1605. http://doi.org/10.1109/JSTARS.2018.2803074

Chen, C. W., & Zebker, H. A. (2002). Phase unwrapping for large SAR interferograms: Statistical segmentation and generalized network models. *IEEE Transactions on Geoscience and Remote Sensing*, *40*(8), 1709–1719. http://doi.org/10.1109/TGRS.2002.802453

Cheng, X., & Xu, G. (2006). The integration of JERS-1 and ERS SAR in differential interferometry for measurement of complex glacier motion. *Journal of Glaciology*, *52*(176), 80–88. http://doi.org/10.3189/172756506781828881

Cloude, S. R. (2009). *Polarisation: Applications in Remote Sensing.* New York: Oxford University Press.

Cuffey, K. M., & Paterson, W. S. B. (2010). *The Physics of Glaciers* (Fourth). Elsevier.

Dee, Dick, & National Center for Atmospheric Research Staff. (2019). The Climate Data Guide: ERA-Interim. Retrieved February 16, 2019, from https://climatedataguide.ucar.edu/climate-data/era-interim

Dimri, A. P., & Dash, S. K. (2010). Winter temperature and precipitation trends in the Siachen Glacier. *Current Science*, *98*(12), 1620–1625.

Eldhuset, K., Andersen, P. H., Hauge, S., Isaksson, E., & Weydahl, D. J. (2003). ERS tandem InSAR processing for DEM generation, glacier motion estimation and coherence analysis on Svalbard. *International Journal of Remote Sensing*, *24*(7), 1415–1437. http://doi.org/10.1080/01431160210153039

Euillades, L. D., Euillades, P. A., Riveros, N. C., Masiokas, M. H., Ruiz, L., Pitte, P., … Balbarani, S. (2016). Detection of glaciers displacement time-series using SAR. *Remote Sensing of Environment*, *184*, 188–198. http://doi.org/10.1016/J.RSE.2016.07.003

European Space Agency. (2014). ASAR User Guide. Retrieved December 3, 2018, from https://earth.esa.int/handbooks/asar/CNTR1-1-2.html#eph.asar.ug.choos.sci

Ferretti, A., Monti-Guarnieri, A., Prati, C., & Rocca, F. (2007). *InSAR Principles: Guidelines for SAR Interferometry Processing and Interpretation.* (K. Fletcher, Ed.)*InSAR Principles.* Noordwijk, The Netherlands: ESA Publications. http://doi.org/10.1145/2541016.2541057

Ferretti, A., Prati, C., & Rocca, F. (2000). Nonlinear Subsidence Rate Estimation UsingPermanent Scatterers in Differential SAR Interferometry. *IEEE Transactions on Geoscience and Remote Sensing*, *38*(5), 2202–2212.

Ferretti, A., Prati, C., & Rocca, F. (2001). Permanent scatterers in SAR interferometry. *IEEE Transactions on Geoscience and Remote Sensing*, *39*(1), 8–20. http://doi.org/10.1109/36.898661

Forster, R. R., Isacks, B. L., & Das, S. B. (1996). Shuttle imaging radar (SIR-C/X-SAR) reveals near-surface properties of the South Patagonian Icefield. *Journal of Geophysical Research E: Planets*, *101*(E10),

23169–23180. http://doi.org/10.1029/96JE01950

Gabriel, A., Goldstein, R. M., & Zebker, H. A. (1989). Mapping small elevation changes over large areas: Differential radar interferometry. *Journal of Geophysical Research*, *94*(B7), 9183. http://doi.org/10.1029/JB094iB07p09183

Gantayat, P., Kulkarni, A. V., & Srinivasan, J. (2014). Estimation of ice thickness using surface velocities and slope: Case study at Gangotri Glacier, India. *Journal of Glaciology*, *60*(220), 277–282. http://doi.org/10.3189/2014JoG13J078

Gardner, A. S., Moholdt, G., Cogley, J. G., Wouters, B., Arendt, A. A., Wahr, J., … Paul, F. (2013). A Reconciled Estimate of Glacier Contributions to Sea Level Rise: 2003 to 2009. *Science*, *340*(6134), 852–857. http://doi.org/10.1126/science.1234532

Garg, P. K., Shukla, A., Tiwari, R. K., & Jasrotia, A. S. (2017). Assessing the status of glaciers in part of the Chandra basin, Himachal HimalayaA multiparametric approach. *Geomorphology*, *284*, 99–114. http://doi.org/10.1016/j.geomorph.2016.10.022

Giles, A. B., Massom, R. A., & Warner, R. C. (2009). A method for sub-pixel scale feature-tracking using Radarsat images applied to the Mertz Glacier Tongue, East Antarctica. *Remote Sensing of Environment*, *113*(8), 1691–1699. http://doi.org/10.1016/j.rse.2009.03.015

Goldstein, R. M., Engelhardt, H., Kamb, B., & Frolich, R. M. (1993). Satellite Radar Interferometry for Monitoring Ice Sheet Motion: Application to an Antarctic Ice Stream. *Science*, *262*(5139), 1525–1530. http://doi.org/10.1126/science.262.5139.1525

Gray, A. L., Short, N., Mattar, K. E., & Jezek, K. C. (2001). Velocities and flux of the filchner ice shelf and its tributaries determined from speckle tracking interferometry. *Canadian Journal of Remote Sensing*, *27*(3), 193–206. http://doi.org/10.1080/07038992.2001.10854936

Green, H. E. (2008). The phase centre of a Pure Mode, Smooth Wall, Conical Horn. *Progress In Electromagnetics Research B*, *4*, 285–298. http://doi.org/10.2528/PIERB08010705

Gupta, R. P., Haritashya, U. K., & Singh, P. (2005). Mapping dry/wet snow cover in the Indian Himalayas using IRS multispectral imagery. *Remote Sensing of Environment*, *97*(4), 458–469. http://doi.org/10.1016/j.rse.2005.05.010

Haeberli, W., Hoelzle, M., Paul, F., & Zemp, M. (2007). Integrated monitoring of mountain glaciers as key indicators of global climate change: The European Alps. *Annals of Glaciology*, *46*, 150–160. http://doi.org/10.3189/172756407782871512

Hanssen, R. F. (2001). *Radar Interferometry: Data Interpretation and Error Analysis (PhD Thesis)*. TU Delft.

Houghton, J. T., Ding, Y., Griggs, D. J., Noguer, M., Van Der Linden, P. J., Dai, X., … Johnson, C. A. (2001). *Climate change 2001: the scientific basis. Contribution of Working Group I to the Third Assessment Report of the Intergovernmental Panel on Climate Change*. Cambridge.

Hu, J., Li, Z. W., Zhu, J. J., Ren, X. C., & Ding, X. L. (2010). Inferring three-dimensional surface displacement field by combining SAR interferometric phase and amplitude information of ascending and descending orbits. *Science China Earth Sciences*, *53*(4), 550–560. http://doi.org/10.1007/s11430-010-0023-1

Huang, C., Davis, L. S., & Townshend, J. R. G. (2002). An assessment of support vector machines for land cover classification. *International Journal of Remote Sensing*, *23*(4), 725–749. http://doi.org/10.1080/01431160110040323

Huang, L., & Li, Z. (2011). Comparison of SAR and optical data in deriving glacier velocity with feature tracking. *International Journal of Remote Sensing*, *32*(10), 2681–2698. http://doi.org/10.1080/01431161003720395

Huang, L., Li, Z., Tian, B.-S., Chen, Q., Liu, J.-L., & Zhang, R. (2011). Classification and snow line detection for glacial areas using the polarimetric SAR image. *Remote Sensing of Environment*, *115*(7), 1721–1732. http://doi.org/10.1016/J.RSE.2011.03.004

Hubbard, B., & Glasser, N. (2005). *Field Techniques in Glaciology and Glacial Geomorphology*. England: John Wiley and Sons Ltd.

Immerzeel, W. W., van Beek, L. P. H., & Bierkens, M. F. P. (2010). Climate Change Will Affect the Asian Water Towers. *Science*, *328*(5984), 1382–1385. http://doi.org/10.1126/science.1183188

Jauvin, M., Yan, Y., Trouve, E., & Fruneau, B. (2018). Potential and Limits of Sentinel-1 Data for Small Alpine Glaciers Monitoring. *IGARSS 2018 - 2018 IEEE International Geoscience and Remote Sensing Symposium*, 5165–5168. http://doi.org/10.1109/IGARSS.2018.8519231

Jiancheng Shi, Dozier, J., & Rott, H. (1994). Snow mapping in alpine regions with synthetic aperture radar. *IEEE Transactions on Geoscience and Remote Sensing*, *32*(1), 152–158. http://doi.org/10.1109/36.285197

Joughin, I. R., Kwok, R., & Fahnestock, M. A. (1998). Interferometric estimation of three-dimensional ice-flow using ascending and descending passes. *IEEE Transactions on Geoscience and Remote Sensing*, *36*(1), 25–37. http://doi.org/10.1109/36.655315

Joughin, I. R., Smith, B. E., & Abdalati, W. (2010). Glaciological advances made with interferometric synthetic aperture radar. *Journal of Glaciology*, *56*(200), 1026–1041. Retrieved from https://www.igsoc.org/journal/56/200/j10j204.pdf

Joughin, I. R., Winebrenner, D. P., & Fahnestock, M. A. (1995). Observations of ice-sheet motion in Greenland using satellite radar interferometry. *Geophysical Research Letters*, *22*(5), 571–574. http://doi.org/10.1029/95GL00264

Kääb, A., Chiarle, M., Raup, B., & Schneider, C. (2007). Climate change impacts on mountain glaciers and permafrost. *Global and Planetary Change*, *56*(1–2), vii–ix. http://doi.org/10.1016/j.gloplacha.2006.07.008

Kääb, A., Wessels, R., Haeberli, W., Huggel, C., Kargel, J. S., & Khalsa, S. J. S. (2003). Rapid ASTER imaging facilitates timely assessment of glacier hazards and disasters. *Eos, Transactions American Geophysical Union*, *84*(13), 117. http://doi.org/10.1029/2003EO130001

Kaser, G., Grosshauser, M., & Marzeion, B. (2010). Contribution potential of glaciers to water availability in different climate regimes. *Proceedings of the National Academy of Sciences*, *107*(47), 20223–20227. http://doi.org/10.1073/pnas.1008162107

Kodama, H., & Mae, S. (1976). The flow of glaciers in the Khumbu region. Glaciological Expedition to Nepal, Contribution No 10. *Journal of the Japanese Society of Snow and Ice*, *38*(Special), 31–36.

König, M., Winther, J.-G., & Isaksson, E. (2001). Measuring snow and glacier ice properties from satellite. *Reviews of Geophysics*, *39*(1), 1–27. http://doi.org/10.1029/1999RG000076

Kulkarni, A. V. (1992). Mass Balance of Himalayan Glaciers Using Aar and Ela Methods. *Journal of Glaciology*, *38*(128), 101–104.

Kulkarni, A. V., Rathore, B. P., Singh, S. K., & Bahuguna, I. M. (2011). Understanding changes in the Himalayan cryosphere using remote sensing techniques. *International Journal of Remote Sensing*, *32*(3), 601–615. http://doi.org/10.1080/01431161.2010.517802

Kumar, V., Venkataraman, G., & Høgda, K. A. (2011). Glacier surface velocity estimation using SAR interferometry technique applying ascending and descending passes in Himalayas. *International Journal of Applied Earth Observation and Geoinformation*, *13*(4), 545–551. http://doi.org/10.1016/j.jag.2011.02.004

Kumar, V., Venkataraman, G., Høgda, K. A., & Larsen, Y. (2013). Estimation and validation of glacier surface motion in the northwestern Himalayas using high-resolution SAR intensity tracking. *International Journal of Remote Sensing*, *34*(15), 5518–5529. http://doi.org/10.1080/01431161.2013.792965

Kumar, V., Venkataraman, G., Larsen, Y., & Hogda, K. A. (2011). SAR interferometry and offset tracking approaches for glacier movement estimation in the Himalaya. In *2011 IEEE International Geoscience and Remote Sensing Symposium* (pp. 3175–3178). IEEE.

http://doi.org/10.1109/IGARSS.2011.6049893

Kwok, R., & Fahnestock, M. A. (1996). Ice sheet motion and topography from radar interferometry. *IEEE Transactions on Geoscience and Remote Sensing*, *34*(1), 189–200. http://doi.org/10.1109/36.481903

Li, J., Li, Z., Wu, L., Xu, B., Hu, J., Zhou, Y., & Miao, Z. (2018). Deriving a time series of 3D glacier motion to investigate interactions of a large mountain glacial system with its glacial lake: Use of Synthetic Aperture Radar Pixel Offset-Small Baseline Subset technique. *Journal of Hydrology*, *559*, 596–608. http://doi.org/10.1016/J.JHYDROL.2018.02.067

Lucchitta, B. K., Rosanova, C. E., & Mullins, K. F. (1995). Velocities of Pine Island Glacier, West Antarctica, from ERS-1 SAR images. *Annals of Glaciology*, *21*, 277–283. http://doi.org/10.1017/S0260305500015949

Mahagaonkar, A., Wangchuk, S., Ramanathan, A., Tshering, D., & Mahanta, C. (2017). Glacier Environment and Climate Change in Bhutan—An Overview. *Journal of Climate Change*, *3*(2), 1–10. http://doi.org/10.3233/JCC-170010

Massonnet, D., & Feigl, K. L. (1998). Radar interferometry and its application to changes in the Earth's surface. *Reviews of Geophysics*, *36*(4), 441–500. http://doi.org/10.1029/97RG03139

Massonnet, D., Rossi, M., Carmona, C., Adragna, F., Peltzer, G., Feigl, K. L., & Rabaute, T. (1993). The displacement field of the Landers earthquake mapped by radar interferometry. *Nature*, *364*, 138–142.

Mattar, K. E., Vachon, P. W., Geudtner, D., Gray, A. L., Cumming, I. G., & Brugman, M. (1998). Validation of alpine glacier velocity measurements using ERS Tandem-Mission SAR data. *IEEE Transactions on Geoscience and Remote Sensing*, *36*(3), 974–984. http://doi.org/10.1109/36.673688

Meier, M. F., Dyurgerov, M. B., Rick, U. K., O'Neel, S., Pfeffer, W. T., Anderson, R. S., … Glazovsky, A. F. (2007). Glaciers Dominate Eustatic Sea-Level Rise in the 21st Century. *Science*, *317*(5841), 1064–1067. http://doi.org/10.1126/science.1143906

Mohr, J. J., Reeh, N., & Madsen, S. N. (1998). Three-dimensional glacial flow and surface elevation measured with radar interferometry. *Nature*, *391*(6664), 273–276. http://doi.org/10.1038/34635

Moll, A., & Braun, M. (2006). Determination of glacier velocities on King George Island (Antarctica) by DInSAR. *International Geoscience and Remote Sensing Symposium (IGARSS)*, 1236–1239. http://doi.org/10.1109/IGARSS.2006.319

Moreira, A., Prats-Iraola, P., Younis, M., Krieger, G., Hajnsek, I., & Papathanassiou, K. P. (2013). A tutorial on synthetic aperture radar. *IEEE Geoscience and Remote Sensing Magazine*, *1*(1), 6–43. http://doi.org/10.1109/MGRS.2013.2248301

Mouginot, J., Rignot, E., Scheuchl, B., & Millan, R. (2017). Comprehensive Annual Ice Sheet Velocity Mapping Using Landsat-8, Sentinel-1, and RADARSAT-2 Data. *Remote Sensing*, *9*(4), 364. http://doi.org/10.3390/rs9040364

Mouginot, J., Scheuch, B., & Rignot, E. (2012). Mapping of ice motion in antarctica using synthetic-aperture radar data. *Remote Sensing*, *4*(9), 2753–2767. http://doi.org/10.3390/rs4092753

Müller, K. (2011). *Microwave penetration in polar snow and ice: Implications for GPR and SAR (PhD Thesis)*. Oslo, Norway: University of Oslo.

Nagler, T., Rott, H., Hetzenecker, M., Wuite, J., & Potin, P. (2015). The Sentinel-1 mission: New opportunities for ice sheet observations. *Remote Sensing*, *7*(7), 9371–9389. http://doi.org/10.3390/rs70709371

Parrella, G., Fischer, G., Hajnsek, I., & Papathanassiou, K. P. (2018). Mapping the Ice Zones of West Greenland Using Multi-Frequency Polarimetric SAR Data. In *European Conference on Synthetic Aperture Radar (EUSAR)*. Aachen, Germany. Retrieved from https://elib.dlr.de/119210/1/Mapping_Greenland_ice_zones_Parrella_et_al_abstract.pdf

Partington, K. C. (1998). Discrimination of glacier facies using multi-temporal SAR data. *Journal of Glaciology*, *44*(146), 42–53.

Paul, F. (1998, June). Theory of Synthetic Aperture Radar. Retrieved August 20, 2018, from http://www.geo.uzh.ch/~fpaul/sar_theory.html

Paul, F., & Haeberli, W. (2008). Spatial variability of glacier elevation changes in the Swiss Alps obtained from two digital elevation models. *Geophysical Research Letters*, *35*(21), L21502. http://doi.org/10.1029/2008GL034718

Prats, P., Scheiber, R., Reigher, A., Andres, C., & Horn, R. (2009). Estimation of the surface velocity field of the Aletsch glacier using multibaseline airborne SAR interferometry. *IEEE Transactions on Geoscience and Remote Sensing*, *47*(2), 419–430. http://doi.org/10.1109/TGRS.2008.2004277

Pritchard, H., Arthern, R. J., Vaughan, D. G., & Edwards, L. A. (2009). Extensive dynamic thinning on the margins of the Greenland and Antarctic ice sheets. *Nature*, *461*(7266), 971–975. http://doi.org/10.1038/nature08471

Rignot, E. (1998). Fast Recession of a West Antarctic Glacier. *Science*, *281*(5376), 549–551. http://doi.org/10.1126/science.281.5376.549

Rignot, E., Echelmeyer, K., & Krabill, W. (2001). Penetration depth of interferometric synthetic-aperture radar signals in snow and ice. *Geophysical Research Letters*, *28*(18), 3501–3504. http://doi.org/10.1029/2000GL012484

Rignot, E., Jacobs, S., Mouginot, J., & Scheuchl, B. (2013). Ice-shelf melting around antarctica. *Science*, *341*(6143), 266–270. http://doi.org/10.1126/science.1235798

Rignot, E., Jezek, K. C., & Sohn, H. G. (1995). Ice flow dynamics of the Greenland Ice Sheet from SAR interferometry. *Geophysical Research Letters*, *22*(5), 575–578. http://doi.org/10.1029/94GL03381

Rosenzweig, C., Karoly, D., Vicarelli, M., Neofotis, P., Wu, Q., Casassa, G., … Imeson, A. (2008). Attributing physical and biological impacts to anthropogenic climate change. *Nature*, *453*(7193), 353–357. http://doi.org/10.1038/nature06937

Rott, H., Domik, G., & Matzler, C. (1985). *Study on use and characteristics of SAR for land snow and ice applications. Final Report to ESA*. Innsbruck, Austria.

Rott, H., Sturm, K., & Miller, H. (1993). Active and passive microwave signatures of Antarctic firn by means of field measurements and satellite data. *Annals of Glaciology*, *17*, 337–343. http://doi.org/10.3189/S0260305500013070

Sánchez-Gámez, P., & Navarro, F. J. (2017). Glacier surface velocity retrieval using D-InSAR and offset tracking techniques applied to ascending and descending passes of sentinel-1 data for southern ellesmere ice caps, Canadian Arctic. *Remote Sensing*, *9*(5), 1–17. http://doi.org/10.3390/rs9050442

Satyabala, S. P. (2016). Spatiotemporal variations in surface velocity of the Gangotri glacier, Garhwal Himalaya, India: Study using synthetic aperture radar data. *Remote Sensing of Environment*, *181*, 151–161. http://doi.org/10.1016/J.RSE.2016.03.042

Schneevoigt, N. J., Sund, M., Bogren, W., Kääb, A., & Weydahl, D. J. (2012). Glacier displacement on Comfortlessbreen, Svalbard, using 2-pass differential SAR interferometry (DInSAR) with a digital elevation model. *Polar Record*, *48*(1), 17–25. http://doi.org/10.1017/S0032247411000453

Shekhar, M. S., Chand, H., Kumar, S., Srinivasan, K., & Ganju, A. (2010). Climate-change studies in the western Himalaya. *Annals of Glaciology*, *51*(54), 105–112. http://doi.org/10.3189/172756410791386508

Shi, J., & Dozier, J. (1995). Inferring snow wetness using C-band data from SIR-C's polarimetric synthetic aperture radar. *IEEE Transactions on Geoscience and Remote Sensing*, *33*(4), 905–914. http://doi.org/10.1109/36.406676

Sood, S. (2014). *Glacier Classification and Movement Estimation using SAR Polarimetric and Interferometric Techniques (MSc Thesis)*. Enschede: University of Twente Faculty of Geo-information Science and Earth Observation.

Strozzi, T., Luckman, A., Murray, T., Wegmuller, U., & Werner, C. L. (2002). Glacier motion estimation

using SAR offset-tracking procedures. *IEEE Transactions on Geoscience and Remote Sensing*, *40*(11), 2384–2391. http://doi.org/10.1109/TGRS.2002.805079

Thakur, P. K., Aggarwal, S. P., Arun, G., Sood, S., Senthil Kumar, A., Mani, S., & Dobhal, D. P. (2017). Estimation of Snow Cover Area, Snow Physical Properties and Glacier Classification in Parts of Western Himalayas Using C-Band SAR Data. *Journal of the Indian Society of Remote Sensing*, *45*(3), 525–539. http://doi.org/10.1007/s12524-016-0609-y

Thakur, P. K., Dixit, A., Chouksey, A., Aggarwal, S. P., & Kumar, A. S. (2016). Ice sheet features identification, glacier velocity estimation, and glacier zones classification using high-resolution optical and SAR data. In R. Khanbilvardi, A. Ganju, A. S. Rajawat, & J. M. Chen (Eds.), *Proceedings of SPIE 9877, Land Surface and Cryosphere Remote Sensing III* (p. 987719). New Delhi: International Society for Optics and Photonics. http://doi.org/10.1117/12.2224027

Thompson, L., Mosley-Thompson, E., Davis, M., & Brecher, H. (2011). Tropical Glacier, Records and Indicator of Climate Change, Are Disappearing Globally. *Annals of Glaciology*, *52*(59), 23–34. http://doi.org/10.3189/172756411799096231

Tso, B., & Mather, P. (2009). *Classification Methods for Remotely Sensed Data* (Second Edi). CRC Press. http://doi.org/10.1201/9781420090741

Ulaby, F. T., Moore, R. K., & Fung, A. K. (1981). *Microwave Remote Sensing : Active and Passive. Volume 1 - Microwave Remote Sensing Fundamentals and Theory*. Addison-Wesley Publishing.

Vapnik, V. N. (1995). *The nature of statistical learning theory*. New York: Springer-Verlag.

Varugu, B. K., Singh, M., & Rao, Y. S. (2015). Glacier velocity estimation using high resolution SAR images – Application to Gangotri glacier in Himalayas. In *Proceedings (CD) of National Symposium on Geomatics for Digital India–Annual Conventions of Indian Society of Remote Sensing and Indian Society of Geomatics (ISRS-ISG)*. Jaipur, India.

Vaughan, D. G., Comiso, J. C., Allison, I., Carrasco, J., Kaser, G., Kwok, R., … Rignot, E. (2013). Observations: Cryosphere. *Climate Change*, *2103*, 317–382.

Venkataraman, G., Rao, Y. S., & Rao, K. S. (2006). Application of SAR Interferometry for Himalayan Glaciers. In *Proceeding of Fringe 2005 Workshop*. Frascati, Italy: European Space Agency.

Wangensteen, B., Weydahl, D. J., & Hagen, J. O. (2005). Mapping glacier velocities on Svalbard using ERS tandem DInSAR data. *Norsk Geografisk Tidsskrift - Norwegian Journal of Geography*, *59*(4), 276–285. http://doi.org/10.1080/00291950500375500

Weber Hoen, E., & Zebker, H. A. (2000). Penetration depths inferred from interferometric volume decorrelation observed over the Greenland Ice Sheet. *IEEE Transactions on Geoscience and Remote Sensing*, *38*(6), 2571–2583. http://doi.org/10.1109/36.885204

Yao, T., Thompson, L. G., Mosbrugger, V., Zhang, F., Ma, Y., Luo, T., … Fayziev, R. (2012). Third Pole Environment (TPE). *Environmental Development*, *3*, 52–64. http://doi.org/10.1016/j.envdev.2012.04.002

Zebker, H. A., Rosen, P. A., Goldstein, R. M., Gabriel, A., & Werner, C. L. (1994). On the derivation of coseismic displacement fields using differential radar interferometry: The Landers earthquake. *Journal of Geophysical Research: Solid Earth*, *99*(B10), 19617–19634. http://doi.org/10.1029/94JB01179

Zemp, M., Frey, H., Gärtner-Roer, I., Nussbaumer, S. U., Hoelzle, M., Paul, F., … Vincent, C. (2015). Historically unprecedented global glacier decline in the early 21st century. *Journal of Glaciology*, *61*(228), 745–762. http://doi.org/10.3189/2015JoG15J017

Zemp, M., Hoelzle, M., & Haeberli, W. (2009). Six decades of glacier mass-balance observations: a review of the worldwide monitoring network. *Annals of Glaciology*, *50*(50), 101–111. http://doi.org/10.3189/172756409787769591

APPENDIX – 1

Details of the Sample Set used for classification of Glacier Facies.

Glacier	Year	Sample Size
Siachen Glacier	2018	4500
	2017	5800
	2016	5750
	2015	5800
Bara Shigri Glacier	2018	4450
	2017	5000
	2016	4500
	2015	5500
Gangotri Glacier	2018	4000
	2017	5000
	2016	4500
	2015	4000

Error matrices produced for accuracy assessment using the test data for Siachen Glacier. (UPF: Upper Percolation Facies; MPF: Middle Percolation Facies; LPF: Lower Percolation Facies; BIF: Bare Ice Facies; DCIF: Debris Covered Ice Facies; UA: User Accuracy; PA: Producer Accuracy; OA: Overall Accuracy).

Siachen Glacier 2018		REFERENCE DATA						UA (%)
		UPF	MPF	LPF	BIF	DCIF	Total	
CLASSIFIED DATA	UPF	**314**	0	0	57	0	**371**	84.6%
	MPF	1	**455**	11	8	1	**476**	95.6%
	LPF	0	7	**334**	3	24	**368**	90.8%
	BIF	33	2	0	**237**	24	**296**	80.1%
	DCIF	2	0	21	23	**164**	**210**	78.1%
	Total	350	464	366	328	213	1721	
PA (%)		89.7%	98.1%	91.3%	72.3%	77.0%	OA – 87.4%	

Siachen Glacier 2017		REFERENCE DATA						UA (%)
		UPF	MPF	LPF	BIF	DCIF	Total	
CLASSIFIED DATA	UPF	**209**	0	0	0	31	**240**	87.1%
	MPF	0	**368**	6	4	19	**397**	92.7%
	LPF	0	1	**318**	14	3	**336**	94.6%
	BIF	0	5	20	**369**	2	**396**	93.2%
	DCIF	60	12	3	2	**280**	**357**	78.4%
	Total	269	386	347	389	335	1726	
PA (%)		77.7%	95.3%	91.6%	94.9%	83.6%	OA – 89.5%	

Siachen Glacier 2016		REFERENCE DATA						UA (%)
		UPF	MPF	LPF	BIF	DCIF	Total	
CLASSIFIED DATA	UPF	**280**	6	0	5	30	**321**	87.2%
	MPF	0	**357**	15	14	0	**386**	92.5%
	LPF	0	2	**251**	1	0	**254**	98.8%
	BIF	0	27	4	**362**	11	**404**	89.6%
	DCIF	44	1	7	2	**339**	393	86.3%
	Total	**324**	**393**	**277**	**384**	**380**	**1758**	
PA (%)		86.4%	90.8%	90.6%	94.3%	89.2%	OA – 90.4%	

Siachen Glacier 2015		REFERENCE DATA					UA (%)
		UPF	MPF	BIF	DCIF	Total	
CLASSIFIED DATA	UPF	**211**	0	0	22	**233**	90.6%
	MPF	0	**278**	25	8	**311**	89.4%
	LPF	0	31	**351**	22	**404**	86.9%
	BIF	33	4	37	**290**	**364**	79.7%
	Total	**244**	**313**	**413**	**342**	**1312**	
PA (%)		86.5%	88.8%	85.0%	84.8%	OA – 86.1%	

Error matrices produced for accuracy assessment using the test data for Bara Shigri Glacier.

Bara Shigri Glacier - 2018		REFERENCE DATA					UA (%)
		UPF	MPF	BIF	DCIF	Total	
CLASSIFIED DATA	UPF	**210**	5	0	21	**236**	89.0%
	MPF	0	**251**	5	6	**262**	95.8%
	LPF	0	32	**156**	5	**193**	80.8%
	BIF	19	17	10	**309**	**355**	87.0%
	Total	**229**	**305**	**171**	**341**	**1046**	
PA (%)		91.7%	82.3%	91.2%	90.6%	OA – 88.5%	

Bara Shigri Glacier - 2017		REFERENCE DATA					UA (%)
		UPF	MPF	BIF	DCIF	Total	
CLASSIFIED DATA	UPF	**384**	0	0	34	**420**	91.4%
	MPF	0	**497**	4	31	**532**	93.4%
	LPF	0	1	**295**	11	**307**	96.1%
	BIF	21	7	16	**255**	**299**	85.3%
	Total	**405**	**505**	**317**	**331**	**1558**	
PA (%)		94.8%	98.4%	93.1%	77.0%	OA – 91.8%	

Bara Shigri Glacier - 2016		REFERENCE DATA					UA (%)
		UPF	MPF	BIF	DCIF	Total	
CLASSIFIED DATA	UPF	**207**	1	3	29	**240**	86.3%
	MPF	0	**289**	13	8	**310**	93.2%
	LPF	0	53	**327**	10	**390**	83.8%
	BIF	31	2	11	**391**	**435**	89.9%
	Total	**238**	**345**	**354**	**438**	**1375**	
PA (%)		87.0%	83.8%	92.4%	89.3%	OA – 88.3%	

Bara Shigri Glacier - 2015		REFERENCE DATA						UA (%)
		UPF	MPF	LPF	BIF	DCIF	Total	
CLASSIFIED DATA	UPF	**228**	3	1	7	40	**279**	81.7%
	MPF	1	**250**	0	5	6	**262**	95.4%
	LPF	0	0	**142**	6	1	**149**	95.3%
	BIF	0	49	3	**484**	32	**568**	85.2%
	DCIF	14	12	0	16	**348**	**390**	89.2%
	Total	**243**	**314**	**146**	**518**	**427**	**1648**	
PA (%)		93.8%	79.6%	97.3%	93.4%	81.5%	OA – 88.1%	

Error matrices produced for accuracy assessment using the test data for Gangotri Glacier.

Gangotri Glacier - 2018		REFERENCE DATA					UA (%)
		UPF	MPF	BIF	DCIF	Total	
CLASSIFIED DATA	UPF	**274**	7	1	29	**311**	88.1%
	MPF	10	**245**	8	1	**264**	92.8%
	BIF	1	18	**380**	8	**407**	93.4%
	DCIF	26	2	9	**156**	**193**	80.8%
	Total	**311**	**272**	**398**	**194**	**1175**	
PA (%)		88.1%	90.1%	95.5%	80.4%	OA – 89.8%	

Gangotri Glacier - 2017		REFERENCE DATA					UA (%)
		UPF	MPF	BIF	DCIF	Total	
CLASSIFIED DATA	UPF	**310**	4	5	32	**351**	88.3%
	MPF	1	**340**	1	10	**352**	96.6%
	BIF	1	4	**391**	10	**405**	96.3%
	DCIF	18	10	6	**329**	**363**	90.6%
	Total	**330**	**358**	**403**	**381**	**1472**	
PA (%)		93.9%	95.0%	97.0%	86.4%	OA – 93.1%	

Gangotri Glacier - 2016		REFERENCE DATA					UA (%)
		UPF	MPF	BIF	DCIF	Total	
CLASSIFIED DATA	UPF	**227**	0	11	30	**268**	84.7%
	MPF	2	**308**	2	19	**331**	93.1%
	BIF	1	2	**291**	6	**300**	97.0%
	DCIF	28	18	0	**379**	**425**	89.2%
	Total	258	328	304	434	1324	
PA (%)		88.0%	93.9%	95.7%	87.3%	OA – 91.0%	

Gangotri Glacier 2015		REFERENCE DATA					UA (%)
		UPF	MPF	BIF	DCIF	Total	
CLASSIFIED DATA	UPF	**149**	2	1	17	**169**	88.2%
	MPF	3	**251**	5	4	**263**	95.4%
	BIF	2	13	**207**	4	**226**	91.6%
	DCIF	17	7	12	**229**	**265**	86.4%
	Total	171	273	225	254	923	
PA (%)		87.1%	91.9%	92.0%	92.0%	OA – 90.6%	